Studying the effects of alternative magnetic field configurations on the sensitivity of the SuperNEMO Demonstrator to 0vbb decay of ^{82}Se

Hamzah Hussain

University College London
Department of Physics and Astronomy

Submitted to University College London in fulfilment
of the requirements for the award of the degree of Doctor of Philosophy

Submitted 2020

$0\nu\beta\beta$ experiment

Declaration

I, Hamzah Hussain confirm that the work presented in this thesis is my own. Where information has been derived from other sources, I confirm that this has been indicated in the thesis.

Abstract

SuperNEMO is a neutrinoless double beta decay ($0\nu\beta\beta$) experiment with an expected half-life sensitivity in excess of 10^{26} years for the isotope ^{82}Se. This corresponds to an effective Majorana neutrino mass of 40 - 100 meV. The unique tracker-calorimeter technique used with the SuperNEMO experiment provides the ability to reconstruct the full event topology of almost any double beta decaying isotope, producing 'smoking gun' evidence for potentially allowing the underlying physical mechanism behind neutrinoless double beta decay to be entangled. Currently the SuperNEMO demonstrator module has been commissioned and is expected to achieve a half-life sensitivity of 6.5 $\times$ 10^{24} years for the neutrinoless double beta decay of ^{82}Se.

A key feature of the SuperNEMO design is the magnetic field that can be used to reject backgrounds originating from sources outside of the detector tracking volume. However, the application of a magnetic field reduces the efficiency of detecting the $\beta\beta$ signal. This thesis presents the development and implementation of a comparative analysis of the detector sensitivity to neutrinoless double beta decay, in the presence of different magnetic field configurations. The magnetic coil for the SuperNEMO demonstrator module has been recently installed and is expected to be activated in due course. The performance of the detector, using three alternative magnetic field configurations, has been considered in this work, including; a uniform field with a constant field strength of 25 G, no field with zero magnetic flux and a realistic field which is a representation of the expected magnetic field taking into account the design of the detector.

The neutrinoless double beta decay half-life sensitivity for ^{82}Se has been estimated for three alternative magnetic field configurations using a window optimised, event counting based analysis.The signal ($0\nu\beta\beta$) detection efficiency and total background contributions from internal, radon and external sources were considered. A maximum half-life sensitivity limit of 1.4 $\times$ 10^{24} years was achieved for the no field scenario with a region of interest between 2.75 and 2.95 MeV. The performance of the no field scenario was only marginally greater than the uniform and realistic fields (1.2 and 1.0 $\times$ 10^{24} years) under the same conditions. As a consequence, the 2022 SuperNEMO demonstrator physics run, will initially run without a magnetic field for an unspecified period of time in order to determine if there is a measurable benefit from not having an active magnetic field.

Acknowledgements

Contents

List of Figures

List of Tables

Introduction

Although neutrinos are the most abundant matter particles in the known Universe, their low interaction cross sections have made the neutrino one of the most mysterious particles in the Standard Model (SM) of particle physics. Historically, the Standard Model has been extremely successful at accurately describing how matter interacts using the four fundamental forces, however, the discovery of neutrino oscillations was beyond any Standard Model prediction for the neutrino. Neutrinos were known to exist in three different flavour eigenstates, ν_e, ν_μ and ν_τ however the phenomenon of neutrino oscillations allows the neutrinos to mix between the different flavour eigenstates. Most importantly, the observation of neutrino oscillation proved that neutrinos were in fact massive particles, contradictory to the standard model prediction of massless neutrinos. Additionally, this raised the question of whether the non-zero neutrino mass is a Dirac or Majorana mass. If the neutrino has a Dirac mass, like the other Standard Model fermions, then the neutrino and anti-neutrino would be distinctly unique particles, whereas if the neutrino has a Majorana mass, the neutrino would be its' own antiparticle.

The only practical method for investigating the nature of neutrino mass is to examine the Beyond Standard Model (BSM) interaction, neutrinoless double beta decay ($0\nu\beta\beta$). Neutrinoless double beta decay is a hypothesised nuclear decay and the neutrinoless analogue of two neutrino double beta decay ($2\nu\beta\beta$), which is an exotic rare nuclear decay resulting in the emission of two beta electrons and two associated neutrinos from the same nucleus. Observing neutrinoless double beta decay would affirm the Majorana nature of the neutrino whilst providing additional insight into the absolute neutrino mass scale and hierarchy.

Many experiments have been developed to probe and measure the hypothetical $0\nu\beta\beta$ decay including the SuperNEMO detector, which is the successor to the previous NEMO-3 experiment that ran and collected data for number of different double beta decaying isotopes between 2003 and 2011. The complete SuperNEMO detector design is comprised of 20 modules, each holding between 5 and 7 kg of a double beta decaying isotope, beginning with ^{82}Se. A full SuperNEMO detector anticipates a half-life sensitivity of $>10^{26}$ years corresponding to an effective neutrino mass of 0.05 to 0.1 eV [1]. Construction of the full SuperNEMO detector is expected to proceed if a positive $0\nu\beta\beta$ signal is observed down to the 50 meV level as SuperNEMO provides the best opportunity to disentangle the underlying physics mechanism for $0\nu\beta\beta$.Moreover, studying the double beta decay of ^{82}Se with the SuperNEMO detector will further improve constraints on the $2\nu\beta\beta$ half-life, which is important for studying the Nuclear Matrix Elements (NMEs) and axial coupling vector g_A.

Currently a single SuperNEMO demonstrator module is undergoing commissioning in the Laboratoire Souterrain de Modane (LSM). The demonstrator module combines unique tracking and calorimetry techniques in order to study the 6.25 kg of ^{82}Se source foil located at the centre of the

demonstrator. The tracking capabilities of the SuperNEMO demonstrator allows the trajectory of reconstructed charged particles to be determined with high accuracy in three dimensions and the segmented calorimeters allows for the energies of individual particles to be measured.

Also, there is the option to apply a magnetic field to the tracker volume, in order to identify particles via their curvature in response to the applied field. Reconstructed particle kinematics combined with particle identification can be used to efficiently reject multiple backgrounds, however the currently proposed magnetic field may in fact not provide the best performance for the demonstrator module and there is also the possibility of taking data without turning on the magnetic field from the beginning.

A short description of each chapter is provided below:

i The first chapter includes an introduction to neutrino phenomenology.

ii Chapter two introduces double beta decay and underlines the physics behind the rare, second order process. An overview of previous, current and future double beta decay experiments is also presented, including a discussion of the SuperNEMO predecessor NEMO-3.

iii Chapter three overviews the SuperNEMO experiment and demonstrator module, including the relevant backgrounds for ^{82}Se double beta decay. Moreover, the different magnetic field configurations, investigated in this work are introduced.

iv The different analysis techniques used in the thesis are presented in chapter 4, including the internal software package Falaise. Additionally, the reconstructed topologies of different particles are described and the subsequent decay channels are explained. Finally, the tools needed to estimate the total signal and background contributions as well as the overall sensitivity of the study are given.

v Chapter five provides an in depth description of the double beta decay event selection used to determine if a reconstructed event has a double beta topology. Furthermore, the detection efficiency for ^{82}Se $0\nu\beta\beta$ is presented alongside the contribution from the irreversible $2\nu\beta\beta$ background. Finally, the sensitivity is estimated for the 'ideal scenario detector', providing the first performance comparison between the three magnetic field configurations.

vi In chapter six, descriptions for the different classifications of backgrounds are provided and the contribution of those backgrounds to the SuperNEMO half-life sensitivity are showcased.

vii Chapter 7 discusses the optimization process for reducing the prominent backgrounds from the chapter six and provides estimations for the overall sensitivity using the statistical approximations discussed in the analysis techniques chapter.

viii The final chapter concludes the magnetic field study, provides a summary of the conducted studies and their main implications regarding how best to utilise the magnetic field for the SuperNEMO demonstrator. Moreover, suggestions for the future strategy, if constructed, of the full SuperNEMO detector will be presented.

Author's Contributions

Chapter 1

Neutrino Phenomenology and Double Beta Decay

The neutrino was first proposed by Wolfgang Pauli in 1930, following observations of continuous energy spectra from β decay electrons. Pauli suggested the existence of a small uncharged particle, emitted alongside the β electron, allowing the decay to conserve energy, momentum and spin. Enrico Fermi coined the name neutrino in reference to the similarly uncharged neutron, following its discovery by James Chadwick in 1932.

Having no electric or colour charge made the neutrino very difficult to identify from low intensity beta decaying isotopes and it wasn't until the 1950s that experimental evidence of the neutrino was first discovered at the Savannah River Nuclear Reactor [2]. Cowan and Reines erected a nearby detector and successfully used the giant flux of antineutrinos coming from the reactor to illustrate the process of inverse beta decay, winning them the 1995 Nobel Prize. Over the following half century, further breakthroughs were made in the field of neutrino physics, including the discovery of multiple neutrino flavours, ν_e, ν_μ and ν_τ, corresponding to the three charged leptons. In the late 1960s, the Homestake experiment first measured the incoming solar neutrino flux as roughly 1/3 to 1/2 of the hypothesised flux [3], ultimately resulting in the discovery of neutrino oscillation and non-zero neutrino mass.

1.1 The Standard Model Neutrino

The Standard Model (SM) of particle physics describes fundamental particles and their interactions through the three underlying forces, the electromagnetic, the strong nuclear and the weak nuclear force. It is a renormalizable quantum field theory with an SU(3) x SU(2) x U(1) symmetry, representing the strong, weak and electromagnetic interactions respectively.

$$\underbrace{SU(3)}_{Strong} \text{ x } \underbrace{SU(2) \text{ x } U(1)}_{\text{Electroweak}} \tag{1.1}$$

Predictions made by the Standard Model have been experimentally probed and proven to a high degree of accuracy, although the model falls short in certain aspects, in particular, the non-zero mass of neutrinos. Within the Standard Model neutrinos are massless, but we know, from observing neutrino oscillations, this is false. Fermions cannot have an explicit gauge invariant mass term in

the Standard Model Lagrangian and only gain their mass via spontaneous symmetry breaking. The absence of the right handed neutrino (or left handed anti-neutrino) does not allow the neutrino to couple to the Higgs and so the neutrino does not gain a Yukawa mass term from the Standard Model spontaneous symmetry breaking. The origin of neutrino mass is still unclear, however we know the Standard Model is wrong and neutrinos do have a non-zero mass.

1.2 Origins of Neutrino Mass

Neutrino oscillation was first proposed by Bruno Pontecorvo, akin to the oscillation observed with Kaons,

$$K^0 \longleftrightarrow \bar{K}^0 \tag{1.2}$$

but it wasn't until the Homestake [3] experiment that evidence of neutrino oscillations was first observed. The Homestake experiment encountered a deficit in the number of expected solar neutrinos, with only 1/3 of the expected number being measured during experimentation, inferring that the solar neutrinos were being subject to an interaction causing a reduction in flux. The solar neutrino flux was by using the electron neutrinos produced by proton-proton fusion in the centre of the sun to induce the radiochemical transmutation of ^{37}Cl into ^{37}Ar via the inverse beta process,

$$^{37}\mathrm{Cl}^{+} + \nu_{\mathrm{e}}\ (\mathrm{Solar}) \longrightarrow {}^{37}\mathrm{Ar} + \mathrm{e}^{-} \tag{1.3}$$

Homestake used many tons of a ^{37}Cl containing compound and the resulting ^{37}Ar gas was collected and measured to estimate the neutrino interaction rate. The Homestake detector was only sensitive to the charged current (CC) interaction (Figure 1.1a) and recorded a deficit of two thirds in the solar electron neutrino flux. The deficit of electron neutrinos found in the Homestake experiment was later dubbed the "solar neutrino problem" and it wasn't validated until the end of the 20th century, when experiments such as Kamiokande-II and SNO (Sudbury Neutrino Observatory) reproduced the results from Homestake as well as observing a deficit in the neutral current (NC) (Figure 1.1b) channel [4] . Kamiokande-II and SNO confirmed that the number of solar electron neutrinos was being suppressed as a result of neutrino oscillation and therefore the neutrino mass is non-zero.

Pontecorvo's initial proposals made in [5] and [6] were verified. The neutrino was shown to have a non-zero mass contradictory to the Standard Model expectation. In response to the observed neutrino oscillations, theorists postulated the mechanism by which neutrino oscillation occurred and how the flavour eigenstates interacted with the basal mass eigenstates.

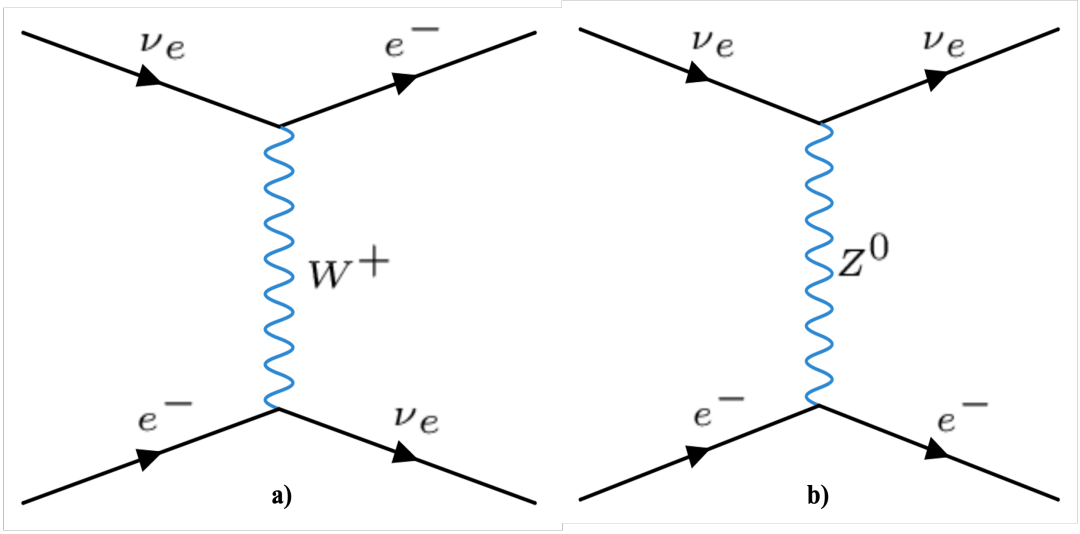

Figure 1.1: Feynman diagrams of neutrino interactions used to detect electron neutrinos. Interaction a) is a Charged Current (CC) electron neutrino-electron scattering and interaction b) is a Neutral Current (NC) electron neutrino-electron scattering [7].

1.2.1 Neutrino Mixing and Oscillation Phenomenology

Neutrinos are produced in weak decays and are emitted in their weak flavour eigenstates ν_e, ν_μ and ν_τ. The flavour eigenstates propagate as plane waves corresponding to linear superpositions of the mass eigenstates ν_1, ν_2 and ν_3. The mixing between the flavour states and the mass states is described by the unitary PMNS (Pontecorvo-Maki-Nakagawa-Sakata) matrix [8],

$$U_{PMNS} = \begin{pmatrix} U_{e1} & U_{e2} & U_{e3} \\ U_{\mu 1} & U_{\mu 2} & U_{\mu 3} \\ U_{\tau 1} & U_{\tau 2} & U_{\tau 3} \end{pmatrix} = \underbrace{\begin{pmatrix} 1 & 0 & 0 \\ 0 & c_{23} & s_{23} \\ 0 & -s_{23} & c_{23} \end{pmatrix}}_{\text{Atmospheric}} \underbrace{\begin{pmatrix} c_{13} & 0 & s_{13}e^{-i\delta} \\ 0 & 1 & 0 \\ -s_{13}e^{i\delta} & 0 & c_{13} \end{pmatrix}}_{\text{Cross-mixing}} \underbrace{\begin{pmatrix} c_{12} & s_{12} & 0 \\ -s_{12} & c_{12} & 0 \\ 0 & 0 & 1 \end{pmatrix}}_{\text{Solar}} \tag{1.4}$$

with $c_{ij} = \cos\theta_{ij}$, $s_{ij} = \sin\theta_{ij}$. θ_{ij} are mixing angles that have been experimentally calculated and represent the mixing between the mass stated i and j. Finally δ represents the neutrino CP violating phase (Section 1.3.1). If the neutrino is a Majorana particle (to be discussed in section 1.4.2), additional CP violating phases α_1 and α_2 can be added to the PMNS matrix in equation 1.4, by post-multiplication with the following,

$$\begin{pmatrix} e^{\frac{i\alpha_1}{2}} & 0 & 0 \\ 0 & e^{\frac{i\alpha_2}{2}} & 0 \\ 0 & 0 & 1 \end{pmatrix} \tag{1.5}$$

U_{PMNS} relates the flavour and mass eigenstates as,

$$\begin{pmatrix} v_e \\ v_\mu \\ v_\tau \end{pmatrix} = \begin{pmatrix} U_{e1} & U_{e2} & U_{e3} \\ U_{\mu 1} & U_{\mu 2} & U_{\mu 3} \\ U_{\tau 1} & U_{\tau 2} & U_{\tau 3} \end{pmatrix} \begin{pmatrix} v_1 \\ v_2 \\ v_3 \end{pmatrix} \tag{1.6}$$

The mixing of flavour and mass eigenstates can be used to illustrate how neutrino oscillation implicitly infers the non-zero mass of neutrinos, starting with oscillations in a vacuum.

1.2.2 Oscillation in a Vacuum

From equation 1.4, the relationship between a single flavour and mass eigenstate can be written as,

$$|\nu_\alpha\rangle = \sum_i U_{\alpha i} |\nu_i\rangle \tag{1.7}$$

where α represents the flavour states $\nu_{e,\mu,\tau}$ and i the mass states $\nu_{1,2,3}$. The mass states ν_i evolve according to the Schrödinger equation and so the time evolution of the mass eigenstate can be written as (in natural units),

$$|\nu_i(t)\rangle = e^{-i(E_i t - p_i L)} |\nu_i(0)\rangle \tag{1.8}$$

where L is the distance travelled and m_i the mass of the eigenstate. The relativistic energy, as a result of the low neutrino mass, can be approximated as,

$$E_i = \sqrt{p_i^2 + m_i^2} = p_i \left(1 + \frac{m_i^2}{p_i^2}\right)^{1/2} \approx p_i + \frac{m_i^2}{2p_i} \tag{1.9}$$

and so the time evolution becomes,

$$|\nu_i(t)\rangle = e^{-i\left(m_i^2/2p_i\right)L} |\nu_i(0)\rangle \tag{1.10}$$

When taking E ≈ p for the relativistic neutrino, equation 1.7 can be written as,

$$|\nu_\alpha(L)\rangle \approx \sum_i U_{\alpha i} e^{-i\left(m_i^2/2E\right)L} |\nu_i\rangle = \sum_{i,\beta} U_{\alpha i} U^*_{\beta i} e^{-i\left(m_i^2/2E\right)L} |\nu_\beta\rangle \tag{1.11}$$

The probability for ν_α oscillating to ν_β is,

$$P(\alpha \to \beta)(L) = |A(\alpha \to \beta)(L)|^2 = |\langle \nu_\beta \mid \nu_\alpha(L)\rangle|^2 \tag{1.12}$$

where A is the transition amplitude for $\nu_\alpha \to \nu_\beta$. Using equation 1.11, the transition probability is,

$$P_{\nu_\alpha \to \nu_\beta}(L) = \sum_{i,j} U^*_{\alpha i} U_{\beta i} U_{\alpha j} U^*_{\beta j} e^{-i\left(\Delta m_{ij}^2/2E\right)L} \tag{1.13}$$

with $\Delta m_{ij}^2 = m_i^2 - m_j^2$ the mass difference between the two mass eigenstates.

According to equation 1.13, in order for oscillations to occur, the Δm_{ij}^2 term must be non-zero. Δm_{ij}^2 is a mass squared difference and so the absolute mass of the neutrino eigenstates cannot be determined directly from oscillations in a vacuum. By measuring the oscillation of one neutrino flavour to another, the mass squared difference can be determined by controlling for the distance travelled L and the energy of the neutrino E.

1.2.3 Oscillations in Matter

Neutrino oscillations also occur in matter, however the presence of significantly dense matter alters the behaviour of the neutrino as it propagates. Neutrinos of all flavours are able to interact with matter via neutral current interactions (Figure 1.1b), exchanging an intermediary Z_0 boson. However, the prevalence of electrons in matter, allows for the charged current interaction (Figure 1.1a) with the exchange of a charged W boson, to occur. As a result, the flavour states undergo different interactions when traversing matter, altering the oscillatory behaviour of the neutrinos. The changing oscillatory behaviour of the neutrinos in matter is known as the Mikheyev-Smirnov-Wolfenstein or MSW effect.

One of the most important examples of the MSW effect is the propagation of solar neutrinos through the sun. The MSW effect is sensitive to both the electron density and neutrino energy. When neutrinos are produced in the centre of the sun, during proton-proton fusion, the significant density at the centre of the sun results in the neutrinos being skewed towards the heavier mass eigenstate. However, as the density decreases away from the sun and eventually becomes negligible

at the surface of the sun, the neutrino is in the mass eigenstate ν_2, and so does not mix as it propagates through space until it reaches earth. Measuring these solar neutrinos provides data for the Δm^2_{21} from Equation 1.13 using the parameters from the PMNS matrix (Equation)1.4).

1.2.4 Oscillations Parameters

The PMNS matrix shown in equation 1.4 has a number of measurable parameters (including Δm^2_{21} from Section 1.2.3), shown in table 1.1. Various neutrino based experiments have been run in the previous few decades in order to improve the constraints set on the PMNS parameters, particularly, the mixing angles and mass squared differences. Reactor and accelerator experiments are the primary detectors used for probing neutrinos and the associated PMNS parameters. Reactor experiments use neutrino fluxes from nearby nuclear reactors as a means to measure the neutrino deficit whereas accelerator experiments generate a neutrino beam that is measured firstly at a near detector and finally at a far detector.

Parameter	Value
$\sin^2(\theta_{12})$	0.307 ± 0.013
Δm^2_{21}	$(7.53 \pm 0.18) \times 10^{-5}$ eV^2
$\sin^2(\theta_{23})$ IH	0.539 ± 0.022
$\sin^2(\theta_{23})$ NH	0.546 ± 0.021
Δm^2_{32} IH	$(-2.524 \pm 0.034) \times 10^{-3}$ eV^2
Δm^2_{32} NH	$(2.453 \pm 0.033) \times 10^{-3}$ eV^2
$\sin^2(\theta_{12})$	$(2.20 \pm 0.07) \times 10^{-2}$
δ CP violating phase	$1.36^{+0.20}_{-0.16}\,\pi$ rad
$\langle \Delta m^2_{21} - \Delta \bar{m}^2_{21} \rangle$	$<1.1 \times 10^{-4}$ eV^2, CL = 99.7%
$\langle \Delta m^2_{32} - \Delta \bar{m}^2_{32} \rangle$	$(-0.12 \pm 0.25) \times 10^{-3}$ eV^2

Table 1.1: Current best estimates for neutrino oscillation parameters [9].

Neutrino oscillation experiments have continued to improve on the previously set constraints for the mixing angles and mass squared differences, however some questions continue to be left unanswered. Currently, only the sign of the Δm^2_{12} is measurable and so the ordering of the mass constraints (mass hierarchy) is still unknown.

1.3 Mass Hierarchy

Neutrino oscillation established the non-zero finite mass of the neutrino, antithetical to the current Standard Model picture of the massless neutrino. Currently, the sign of the Δm_{32} term is indistinguishable resulting in the two hypothesised mass eigenstate orderings, the normal hierarchy (NH) and the inverted hierarchy (IH). Observations of the pure ν_2 solar neutrinos described in section 1.2.3 inferred the sign of the Δm_{21} term, confirming $m_{\nu_1} < m_{\nu_2}$. If the Δm_{32} sign is positive ($\Delta m_{32} > \Delta m_{21} > 0$) the neutrino mass ordering follows the normal hierarchy, whereas if the Δm_{32} sign is negative ($\Delta m_{32} < 0 < \Delta m_{21}$), the inverted hierarchy reigns. Both the normal and inverted hierarchies are illustrated in figure 1.2, with the correlation of the mass eigenstates ($n_{1,2,3}$) and flavour eigenstates ($n_{e\mu\tau}$) highlighted,

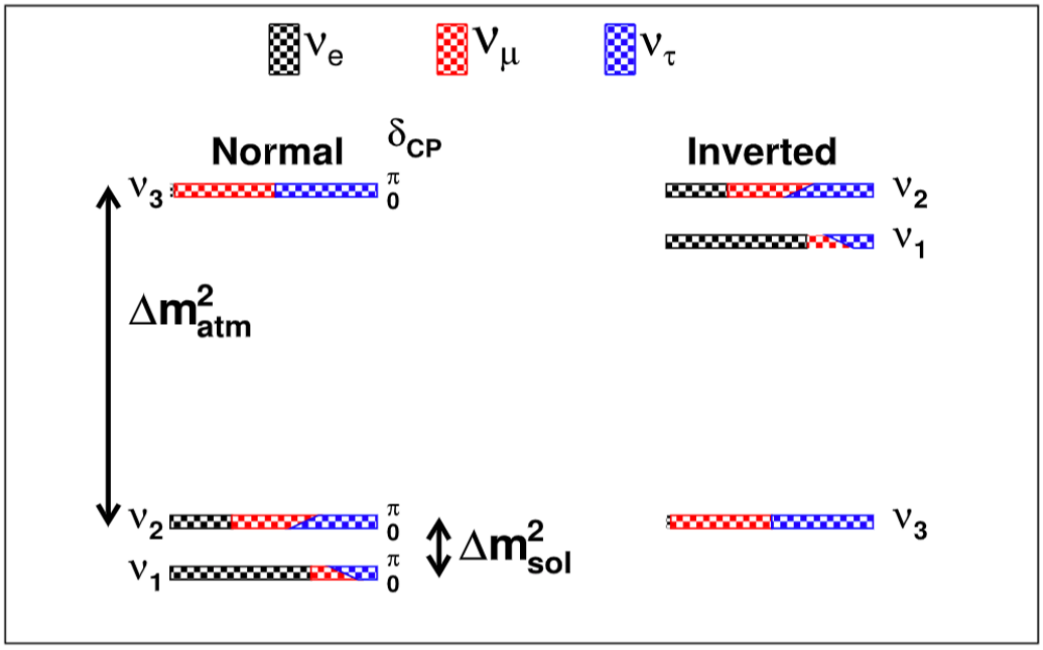

Figure 1.2: Representation of the 'normal' and 'inverted' neutrino mass eigenstate hierarchies. For the 'normal' hierarchy, $m_{\nu_3} > m_{\nu_2} > m_{\nu_1}$ and for the 'inverted' hierarchy, $m_{\nu_3} < m_{\nu_2} < m_{\nu_1}$ [10].

If the normal hierarchy is correct, the lightest mass eigenstate ν_1 would correspond strongly with the electron neutrino, analogous to the charged leptons, whereas, if the inverted hierarchy is proven, the lightest mass eigenstate would correspond strongly with ν_μ and ν_τ. Ongoing experimental data puts a preference on the normal mass ordering, with a $> 2.5\sigma$ statistical significance, taking into account double beta decay, cosmological measurements and oscillation data [11].

1.3.1 CP Violation In The Lepton Sector

As mentioned in Section 1.2.1, the PMNS matrix includes a CP violating phases δ (Equation 1.4) and if the neutrino is a Majorana particle, an additional two phases, α_1 and α_2, are incorporated into the PMNS matrix using Equation 1.5. CP violation was first observed in neutron Kaon decays and was proposed as the answer to the current matter dominated universe we observe. However the known CP decay in the quark sector does not account for the large matter-antimatter asymmetry of the the universe and so, CP violation in the lepton sector is anticipated.

In an effort to reproduce the current matter-antimatter asymmetry of the universe, a small baryon-antibaryon asymmetry must be generated in the early universe using the three Sakharov conditions,

- Baryon number violation, $n_B - n_{\bar{B}}$ is not constant.
- C and CP violation.
- Movement away from thermal equilibrium.

If the CP violating angle δ is unequal to 0° or 180°, CP violation exists in the neutrino sector and is maximal at $\delta = \pm$ 90°. Future experiments are expected to probe the PMNS δ phases by measuring oscillation between neutrino flavours.

DUNE (Deep Underground Neutrino Experiment) is a proposed neutrino beam experiment that will probe the neutrino mass hierarchy and CP violation in the neutrino sector. DUNE will use a 1300 km baseline neutrino beam, with the near detector located at the Fermi National Accelerator Lab (Fermilab) and the far detector, a 70 kt liquid scintillator, at the Sanford Underground Research Lab, 1300 km downstream of the source. DUNE will probe both CP violation and neutrino oscillations by measuring the neutrino beam at the near and far detectors, noting the change in neutrino flux between the two sites. Two prototypes of the DUNE detector, ProtoDUNE-SP and ProtoDUNE-DP have been taking data since 2018 and 2019 respectively. Full DUNE ***

Hyper-Kamiokande (Hyper-K) is a water Cherenkov detector and will supersede Super-Kamiokande (Super-K), which began data dating in 1996 (although it is continuing to take data). Hyper-K is expected to commence operation in 2027 and is currently undergoing R&D and construction. Hyper-K will utilise a 71 m deep water tank, holding 188 kt of water and will use the Cherenkov light from neutrinos interacting with charged particles, in order to reconstruct the energy and direction of the interactions.

Hyper-K will measure CP violation by comparing the rate of $P(\nu_\mu \rightarrow \nu_e)$ and $P(\bar{\nu}_\mu \rightarrow \bar{\nu}_e)$, using neutrinos from supernova, the sun, the atmosphere and the J-PARC neutrino beam. Hyper-K will operate as the far detector for the J-PARC neutrino beam that will be set up to run 2.5° off axis, at 0.6 GeV. Hyper-K, like the DUNE experiment, will also investigate proton decay and neutrino astrophysics alongside the mass hierarchy and CP violation.

Ref

1.4 Beyond Standard Model Neutrino Mass

As previously highlighted, the standard model prediction of the massless neutrino has been demonstrably disproven by neutrino oscillation. However, there are several Standard Model extensions that incorporate a non-zero Beyond Standard Model (BSM) neutrino mass term, the most common of which are the Dirac and Majorana mass terms. The Dirac neutrino is similar to the other standard model leptons, having a distinct particle and anti-particle, whereas the Majorana neutrino is its own antiparticle. Finally a third mechanism, the See-Saw mechanism, proposes a combination of both Dirac and Majorana terms, where each light neutrino has an associated heavy but inert counterpart. In this section, each of the three BSM neutrino mass terms will be introduced and their implementation into the Standard Model will be presented.

1.4.1 Dirac Mass

In the Standard Model neutrinos are incorporated as left handed chiral particles, with no right handed equivalent and vice versa for the antineutrino. Charged leptons and quarks gain their mass through the Yukawa coupling of the left and right handed fields to the Higgs,. In order to couple neutrinos to the Higgs field, a right handed neutrino field is added for each neutrino flavour, producing a Dirac mass term m_D.

The Dirac term in the Lagrangian manifests as,

$$\mathcal{L}^{\mathcal{D}} = -\frac{1}{2} m_\nu^D \bar{\nu}\nu = -\frac{1}{2} m_\nu^D \left(\bar{\nu}_R \nu_L + \bar{\nu}_L \nu_R\right) \tag{1.14}$$

with the chirality operators $P_L = \frac{1}{2}\left(1 - \gamma_5\right)$ and $P_R = \frac{1}{2}\left(1 + \gamma_5\right)$ decomposing the neutrino into its left and right handed components. The Dirac neutrino mass term can then be defined as,

$$m_i = g_Y \frac{v}{\sqrt{2}} \tag{1.15}$$

The Dirac approach provides a simple lepton number conserving extension to the Standard Model for the purpose of adding the non-zero neutrino mass, although there are a several ramifications of this method. The Lagrangian includes the three right handed neutrino fields which only interact gravitationally (having no electric or weak charge), making them completely sterile to the other Standard Model particles. Additionally, the value of g_Y is inexplicably small, many orders of magnitude lower than the corresponding charged lepton couplings as shown in Figure 1.3.

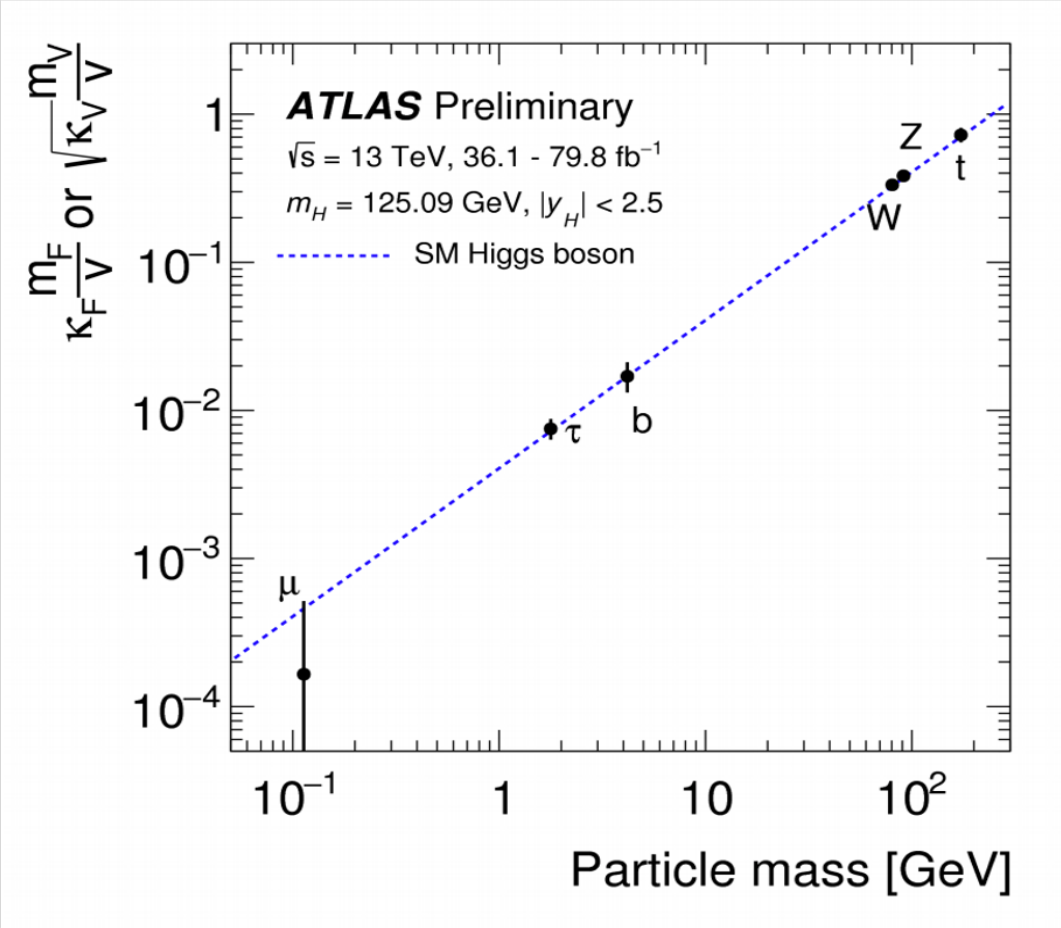

Figure 1.3: Higgs coupling as a function of the Standard Model fermion mass measured by the ATLAS collaboration. The Standard Model prediction for the fermion masses is given by the blue line. At the neutrino mass scale, the predicted Higgs coupling is significantly weaker than any previously measured coupling [12].

1.4.2 Majorana Mass

The Dirac mass terms attempts to couple the left and right handed neutrino fields in a lepton conserving manner, with the addition of sterile right handed neutrinos. However, in 1937, Ettore Majorana proposed that the left and right handed neutrinos were not independent particles [13] and were in fact related by a charge conjugation shown in equation 1.16,

$$\nu_R = \xi \mathcal{C} \bar{\nu}_L^T \tag{1.16}$$

with ξ an arbitrary phase factor, C the charge conjugation matrix and ν_R and ν_L the right and left neutrino fields. As shown in equation 1.14, the neutrino can be decomposed into its left and right

handed components,

$$\nu = \nu_L + \nu_R \tag{1.17}$$

and using using 1.16 can be rewritten as,

$$\nu = \nu_L + \mathcal{C}\bar{\nu}_L^T = \nu_L + \nu_L^c \tag{1.18}$$

Taking the charge conjugation of the Majorana neutrino and using $\hat{C}|\psi >= C|\bar{\psi} >$,

$$\nu^c = (\nu_L + \nu_L^c)^c = \nu_L^c + \nu_L = \nu \tag{1.19}$$

inferring the neutrino and its charge conjugate are the same particle. Particles which are their own antiparticles are known as Majorana particles. Of all the Standard Model fermions, only the neutrino is capable of being a Majorana particle owing to its neutral charge. The Majorana term can be included in the Lagrangian as,

$$\mathcal{L}^M = -\frac{1}{2} m_\nu^M \bar{\nu}_L^c \nu_L \tag{1.20}$$

with m_ν^M the Majorana mass term. Using the Majorana Lagrangian term, neutrinos are able to acquire mass without a Yukawa coupling, however lepton conservation is violated in the process. Like the Dirac mechanism, the Majorana mass term requires a sterile right handed neutrino, although the Majorana mass provides a better explanation of the difference between the neutrino and charged lepton masses.

1.4.3 See-Saw Mechanism

The See-Saw mechanism combines both the Dirac and Majorana mass terms into a single Lagrangian term,

$$\begin{aligned} \mathcal{L}^{D+M} &= \mathcal{L}^D + \mathcal{L}^M \\ &= -\frac{1}{2} m_\nu^D \left(\bar{\nu}_R \nu_L + \bar{\nu}_L \nu_R\right) - \frac{1}{2} m_\nu^M \bar{\nu}_L^c \nu_L + h.c. \\ &= -\frac{1}{2} \begin{pmatrix} \bar{\nu}_L & \bar{\nu}_L^C \end{pmatrix} \begin{pmatrix} m_L & m_D \\ m_D & m_R \end{pmatrix} \begin{pmatrix} \nu_R^C \\ \nu_R \end{pmatrix} + h.c \end{aligned} \tag{1.21}$$

The neutrinos in equation 1.21 are not the mass eigenstates because the mass matrix is not diagonal. To find the mass eigenvalues m_1 and m_2, the mass matrix is first diagonalised, giving,

$$m_{\pm} = \frac{1}{2}\left(m_L + m_R \pm \sqrt{(m_L - m_R)^2 + 4m_D^2}\right) \tag{1.22}$$

For the See-Saw mechanism $m_L = 0$ and $m_D << m_R$, so that the two mass eigenstates become,

$$m_+ \approx m_R \text{ and } m_- \approx \frac{m_D^2}{m_R} \tag{1.23}$$

and the mixing angle

$$\tan(2\theta) = \frac{2m_D}{m_R - m_L} \tag{1.24}$$

The See-Saw mechanism predicts the existence of a heavy GUT scale sterile neutrino, which has a mass of m_R and a light neutrino of mass $\frac{m_D^2}{m_R}$. The heavy sterile neutrino is almost entirely composed of the ν_R field explaining why it is unobserved whereas the light neutrino is almost entirely composed of the ν_L field, corresponding to the observed left handed neutrino. The See-Saw mechanism introduces one heavy sterile neutrino for each of the neutrino flavours, independent of an extremely low Yukawa coupling and could potentially explain the minute mass of the neutrino and its partiality for left handedness at current observable energies. The right handed GUT scale neutrino may also provide further insight into matter-anti matter asymmetries, CP violation and beyond standard model Grand Unification Theories if neutrinos are found to be Majorana particles.

1.5 Neutrino Mass Constraints

Neutrino oscillation observations confirmed the non-zero mass of neutrinos. Improving constraints on the neutrino mass is a major driving force for current and future neutrino experiments, including tritium decay, oscillation, cosmological observations and neutrinoless double beta decay. Tritium decay, cosmological observations and double beta decay experiments provide upper bounds on the neutrino mass whereas oscillation experiments constrain the lower limit on the heaviest neutrino mass state, whether normal (ν_3) or inverted hierarchy (ν_1).

1.5.1 Tritium Decay

Tritium undergoes beta decay into Helium,

$$^3\mathrm{H} \rightarrow {}^3\mathrm{He} + \mathrm{e}^- + \bar{\nu_e} \tag{1.25}$$

with a decay energy of 18.6 KeV. The energy of the electron follows a beta decay spectrum as shown in Figure 1.4a. The ν_e emitted during the decay reduces the energy of the beta electron, lowering the endpoint of the electron energy spectrum Figure 1.4b.

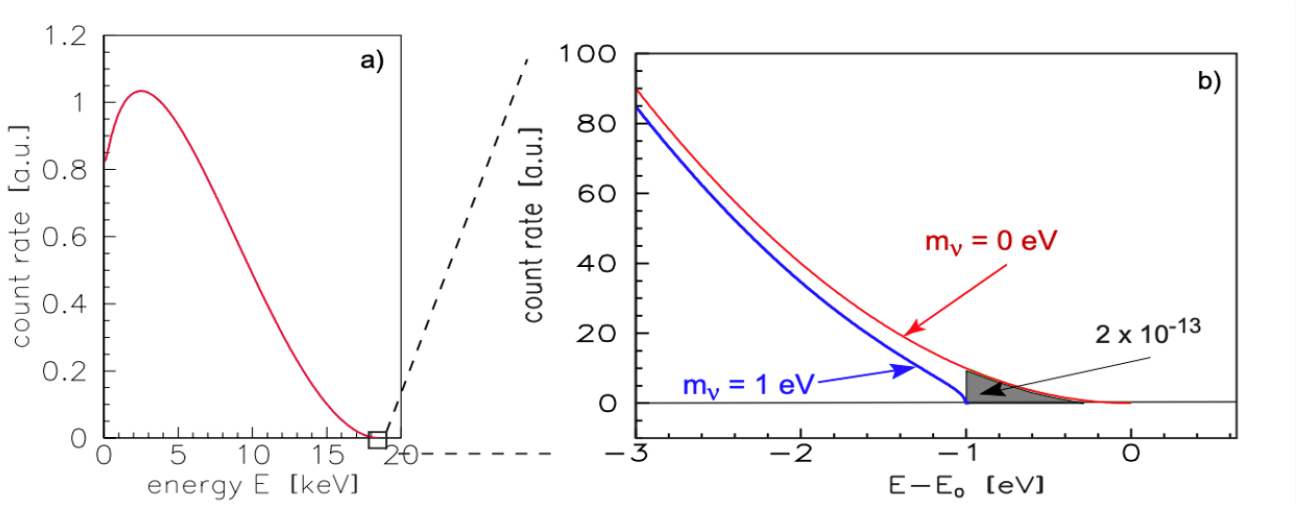

Figure 1.4: Tritium β decay energy spectrum illustrating the discrepancy in the high energy tail due to the emission of a massive 1 eV neutrino [14].

By measuring the energy loss of the beta electron with a massive and massless neutrino, the average of the neutrino mass weighted by the mass state coupling to ν_e is,

$$\langle m_\beta \rangle = \sqrt{\sum_i |U_{ei}|^2 \, m_i^2} \tag{1.26}$$

As the beta decay energy of tritium is of low energy, the endpoint is more sensitive to $\langle m_\beta \rangle$ shifts in the beta electron spectrum, making it a particularly good decay for probing the electron neutrino mass especially considering the simplicity of the decay. The neutrino mass square m_ν^2 as a function of the effective β decay endpoint E_0 is shown in Figure 1.5 and illustrated how the neutrino mass is sensitive to the end point of the β decay spectrum.

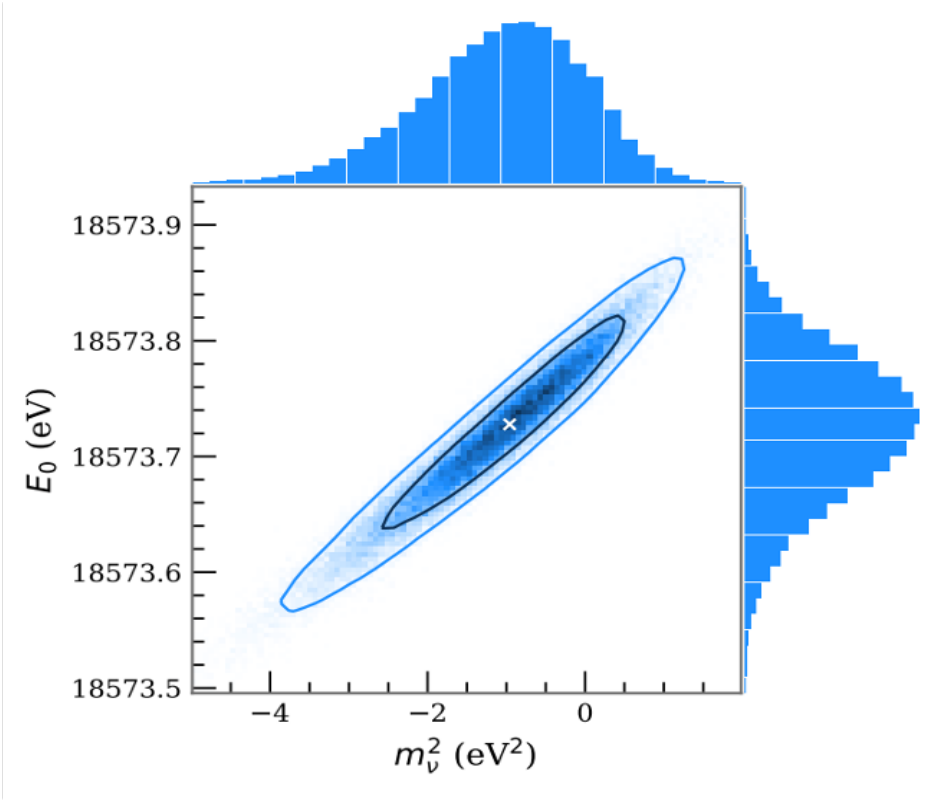

Figure 1.5: Scatter plot of the fit values for the neutrino mass squared and tritium β decay end point energy, including the 1-σ (black) and 2-σ (blue) error contours surrounding the best fit cross. The plot was developed using pseudo-experimental data [15].

The Karlsruhe Tritium Neutrino (KATRIN) experiment currently holds the best upper limit on the mass of the electron neutrino, at $\langle m_\beta \rangle$ <0.8 eV (at 90% CL)[15], an improvement on the previous upper limit of $\langle m_\beta \rangle$ <2 eV (at 95% CL) [16]. The KATRIN experiment is expected to improve the sensitivity on m_ν by an order of magnitude, to roughly 0.2 eV (at 90% CL), in the next couple of years [15]. Constraints on the neutrino mass from tritium beta decay allows for

constraints to be set on the CP violating Majorana phases α_1 and α_2 from Equation 1.5, using the following relationship,

$$\langle m_{\beta\beta} \rangle < \langle m_{\beta} \rangle < \frac{\langle m_{\beta\beta} \rangle}{|\cos(2\theta_{12})| \left(1 - |U_{e3}|^2\right) - |U_{e3}|^2 |} \tag{1.27}$$

Tritium decay measurements can therefore provide constraints for the absolute mass of the neutrino but additionally, can infer the scale of the CP violating Majorana phases, when combined with the observables θ_{12} U_{e3} from oscillation experiments.

1.5.2 Oscillation

As mentioned at the beginning of Section 1.5, neutrino oscillation measurements are incapable of constraining the upper limit of the absolute neutrino mass but provides limits for the lower bound of the heaviest neutrino mass state, whether it is m_3 (normal hierarchy) or m_1 (inverted hierarchy). $|\Delta m^2_{23}|$, the largest neutrino mass splitting, has been measured (Table 1.1) by previous oscillation experiments such as MINOS [17]. The lightest mass state, whether normal or inverted cannot be less than zero therefore $|\Delta m^2_{23}|$ can place a lower bound on the highest mass state of 0.05 eV.

1.5.3 Cosmological Constraints

Cosmological observations can yield limits on the sum of the neutrino masses, by combining a number of cosmological observables. Neutrinos played a significant role in the structure and development of the early universe and the influence of neutrinos can be measured using a number of different tools, including, baryonic acoustic oscillation in the cosmic microwave background (CMB), CMB temperature anisotropy and large scale structure formation. Using the minimal ΛCDM + Σm_ν, with the most up to date CMB data, the 95% confidence limit for the Σm_ν bounds are Σm_ν <0.12 eV, Σm_ν <0.15 MeV and Σm_ν <0.17 MeV for the degenerate, normal and inverted hierarchies respectively [18]. Additionally, the normal hierarchy is mildly preferred to the inverted hierarchy. One important note is that limits from cosmological models often combine many observables, using a large volume of data, however the constraints are extremely model dependant

1.5.4 Neutrinoless Double Beta Decay

Neutrinoless double beta decay is the final type of experiment used to extract constraints on the neutrino mass and is a second order beyond standard model interaction, that, if observed, would confirm the neutrino to be a Majorana particle. Neutrinoless double beta decay is also useful for determining the absolute mass of a Majorana neutrino. Using the light neutrino exchange mechanism discussed in Section 2.3, the effective mass of the Majorana neutrino is,

$$\langle m_{\beta\beta} \rangle = \left| \sum_i U_{ei}^2 m_i \right| \tag{1.28}$$

The effective mass of the Majorana neutrino ($\langle m_{\beta\beta} \rangle$) provides a constraint on the limits for the mass of the lightest mass eigenstate dependant upon the correct mass hierarchy. The current best limits on the half-life sensitivity to neutrinoless double beta decay come from the KamLAND-Zen and GERDA experiments [19], [20], with $\left(T_{1/2}^{0\nu}\right)$ of the order 10^{26}, corresponding to an upper limit of 61 - 165 meV for $\langle m_{\beta\beta} \rangle$. The range of values for $\langle m_{\beta\beta} \rangle$ is shown in Figure 1.6, alongside the normal and inverted hierarchy regions for $\langle m_{\beta\beta} \rangle$ vs $m_{lightest}$ [19]. The upper limit is given as a range to reflect the uncertainty on the nuclear matrix element calculations.

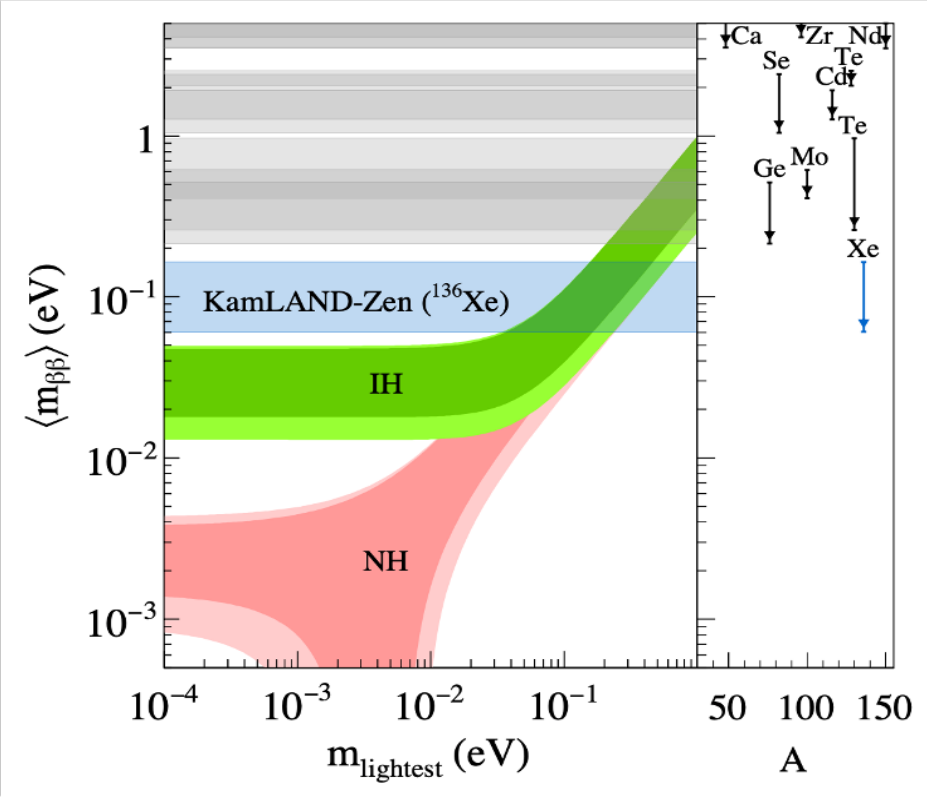

Figure 1.6: $\langle m_{\beta\beta} \rangle$ as a function of the lightest neutrino mass, illustrating the best fit (dark) and 3σ (light) regions for the 'normal' and 'inverted' hierarchy regions.The best limit on $\langle m_{\beta\beta} \rangle$ from the KamLAND-Zen experiment is shown in blue and the best limits for other DBD isotopes are shown in grey [10].

An upper limit of 61 - 165 meV almost completely negates the possibility of the effective neutrino mass being found in the quasi-degenerate region, which combines predictions from the normal and inverted hierarchy. Next generation $0\nu\beta\beta$ experiments are expected to reduce this upper limit

in order to validate or deny the presence of the effective neutrino mass in the inverted hierarchy region. Limits on the effective Majorana neutrino mass only hold true if the neutrino is in fact a Majorana particle. If no evidence for $0\nu\beta\beta$ is found, the limits for observing the decay and identifying neutrinos as Majorana particles become more stringent.

Chapter 2

Double Beta Decay

2.1 Beta Decay

Beta decay is a type of radioactive nuclear decay, in which a atomic nucleus undergoes a transmutation from one element into another with the emission of a beta particle alongside a corresponding neutrino, conserving both Baryon and Lepton numbers. Beta decay is a weak force, charged current interaction, mediated by a $W^{\pm}$ boson. Three different beta decays are commonly observed, β^- decay, β^+ decay and electron capture, resulting in the emission of either a neutrino or antineutrino. β^- decay occurs when a neutron decays into a proton, producing an electron and lepton number conserving antineutrino,

$$n \rightarrow p + e^- + \overline{\nu_e} \tag{2.1}$$

β^+ decay occurs with the decay of a proton into a neutron, emitting a positron and neutrino,

$$p \rightarrow n + e^+ + \nu_e \tag{2.2}$$

and finally, electron capture occurs when an atomic electron is captured by a proton inside the nucleus, which decays into a neutron, similar to β^+ except with the emission of a sole neutrino.

$$p + e^- \rightarrow n + \nu_e \tag{2.3}$$

For $\beta^{\pm}$ decays to occur, the daughter nuclei must have a lower energy than the decaying nuclei, with the energy difference used to create the emitted particles. Moreover, the energy difference must exceed the rest mass energy of the charged lepton and neutrino, with the additional energy providing the particles kinetic energy. Knowing the decay energy of a beta decaying isotope and measuring the energy of the beta electron provides the energy of the neutrino without directly measuring it. The decay energy is extracted using the mass of the parent and daughter nuclei, which are calculated using the Semi-Empirical Mass Formula (SEMF) [21]. The SEMF estimates the mass of an atomic nucleus given the atomic and molecular numbers, in order to determine if the daughter nuclei has a lower energy than the parent, making the decay energetically possible.

The semi-empirical mass formula takes the form[21],

$$m = Zm_p + (A-Z)m_n - a_V A + a_s A^{2/3} + a_c \frac{Z^2}{A^{1/3}} + a_A \frac{(A-2Z)^2}{A} + \delta(A,Z) \tag{2.4}$$

where,

$$\delta(A,Z) = \begin{cases} \frac{a_p}{A^{1/2}} & N \text{ even } (A \text{ even}) \\ 0 & A \text{ odd} \\ \frac{-a_p}{A^{1/2}} & N \text{ odd } (A \text{ even}) \end{cases} \tag{2.5}$$

and m is the mass of the nucleus, A the mass number and Z the atomic number. From left to right, terms one and two approximate the mass of the individual nucleons inside the atom. The remaining terms describe the corrections to the mass, from volume, surface, Coulombic, neutron/proton asymmetry and nucleus spin coupling. In an attempt to describe the energetically viable beta decays, the atomic number Z is plotted below, for a fixed even mass number A,

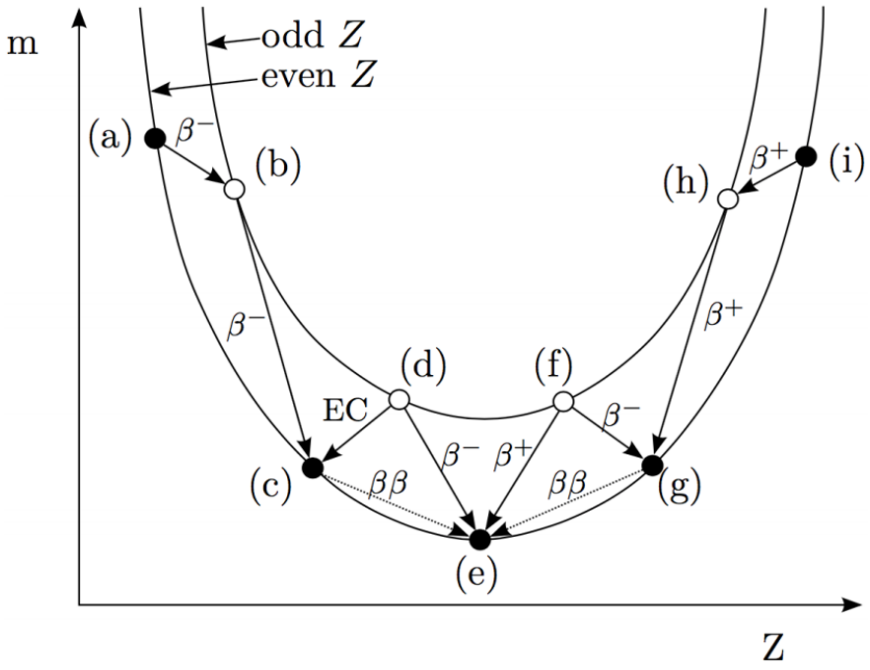

Figure 2.1: SEMF [7]

For an odd value of A, there is only one curve for Z, however, as shown in figure 2.1, for an even value of A, there are two curves, separated by the $\delta(A,Z)$ term described in equation 2.5. The possible $\beta^{\pm}$ transitions between the even and odd Z curves are shown by the arrows in figure 2.1.

2.2 Two Neutrino Double Beta Decay ($2\nu\beta\beta$)

As shown in Section 2.1, Equation 2.4 can be used to determine the mass of a nuclei and whether a particular decay is energetically permitted. For an even-even isotope that is unable to decay directly via beta decay, such as isotope (c) in Figure 2.1, it is possible for them to decay via double beta decay. During double beta decay, two neutrons simultaneously undergo β^- decay, resulting in the emission of two electrons and two corresponding electron neutrinos for the two neutrino variation of double beta decay,

$$(A, Z) \rightarrow (A, Z+2) + 2e^- + 2\bar{\nu}_e \tag{2.6}$$

Double beta decay was first proposed by M. Goeppert-Mayer in 1935 [22] and has been observed in a number of isotopes that have their regular beta decay rate suppressed or forbidden. Like single beta decay, the two emitted electrons lead to a continuous energy spectrum that has an end point at the decay energy $Q^{\beta\beta}$. $2\nu\beta\beta$ has been measured for isotopes including ^{82}Se, ^{100}Mo and ^{136}Xe and has currently been observed for 13 different isotopes ***can't find ref***. Of the measured double beta decaying isotopes, the NEMO-3 experiment studied 7 [23], including ^{82}Se which is the isotope of choice for the SuperNEMO experiment. The reasons for which ^{82}Se was chosen as the source for SuperNEMO will be discussed further in chapter 3.

$2\nu\beta\beta$ is a second order weak interaction that is allowed in the Standard Model, but is extremely rare, with a measured half-life of the order 10^{20} years. The Feynman diagram of the decay is shown in figure 2.2,

From [24], the half-life $\left(T^{2\nu}_{1/2}\right)^{-1}$ of the decay is related to the phase space factor $G^{2\nu}\left(Q_{\beta\beta}, Z\right)$ and the nuclear matrix element $M^{2\nu}$ as,

$$\left(T^{2\nu}_{1/2}\right)^{-1} = G^{2\nu}\left(Q_{\beta\beta}, Z\right)\left|M^{2\nu}\right|^2 \tag{2.7}$$

$G^{2\nu}$ is a four body phase space factor that is calculated analytically and $M^{2\nu}$ represents the transition probability from the initial to the final state of the decay. Measuring double beta decaying isotopes reduces the uncertainties on the values of $M^{2\nu}$ improving the precision of the calculated half-life and phase space factors.

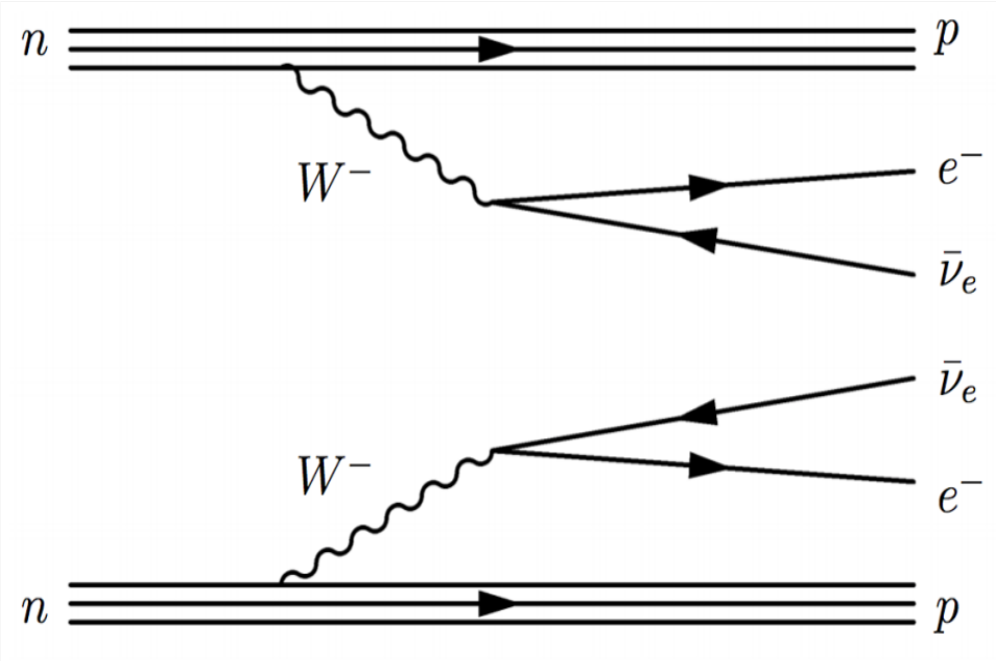

Figure 2.2: Feynman diagram for the Standard Model two neutrino double beta decay ($2\nu\beta\beta$) [7].

2.3 Neutrinoless Double Beta Decay ($0\nu\beta\beta$)

Neutrinoless double beta decay is the neutrinoless analogue of the double beta decay presented in the previous section and is a hypothesised decay which if observed would demonstrate that the neutrino is a Majorana particle [25]. $0\nu\beta\beta$ was first proposed by W.H. Furry in 1939 [26], as an alternative to the two neutrino decay making the decay a possibility for all double beta decaying isotopes. During neutrinoless double beta decay, two beta electrons are simultaneously emitted, however unlike the two neutrino decay, no antineutrinos are emitted (LNE, Section 2.3.1) and all the decay energy is carried by the two electrons,

$$(A, Z) \rightarrow (A, Z + 2) + 2e^{-} \tag{2.8}$$

As a result, the sum energy of the two electrons is equivalent to $Q^{\beta\beta}$ and so we observe a monochromatic line at $Q^{\beta\beta}$ as shown in Figure 2.3.

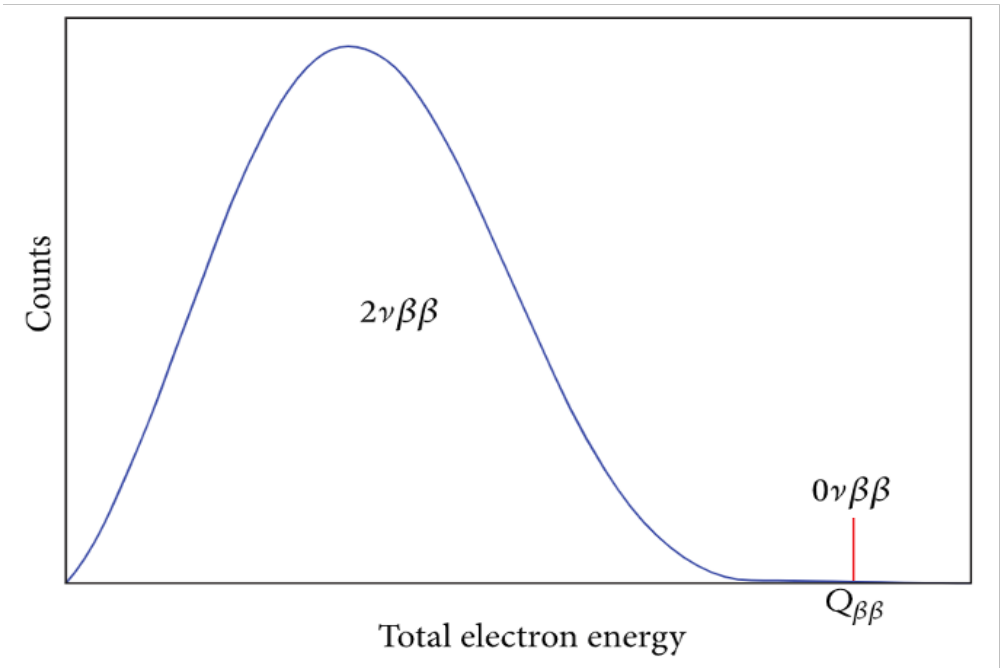

Figure 2.3: $0\nu\beta\beta$ and $2\nu\beta\beta$ theoretical electron energy spectra. $0\nu\beta\beta$ is represented by a single monochromatic line [27].

Without emitting the two associated antineutrinos, $0\nu\beta\beta$ violates lepton number conservation and is therefore a forbidden standard model interaction. The hypothesised mechanisms through which the neutrinoless decay is thought to occur include light neutrino exchange (neutrino mass mechanism), right handed currents, Majoron emission and the more exotic R-parity violating supersymmetry, extra dimensions and squark mixing. Only $0\nu\beta\beta$ experiments that are capable of

detecting individual electrons can differentiate between the different possible decay mechanisms, as shown in Figure 2.9. Precise topological reconstruction is a major advantage of the NEMO-3 and SuperNEMO experiments compared to rival experiments.

If $0\nu\beta\beta$ is observed, light neutrino exchange is the most natural and expected method of decay as it requires the most minimal extension of the Standard Model. Figure 2.4 illustrates neutrinoless double beta decay via light neutrino exchange, where a right handed antineutrino emitted from one W boson is absorbed as a left handed neutrino and only occurs if neutrinos are massive Majorana particles

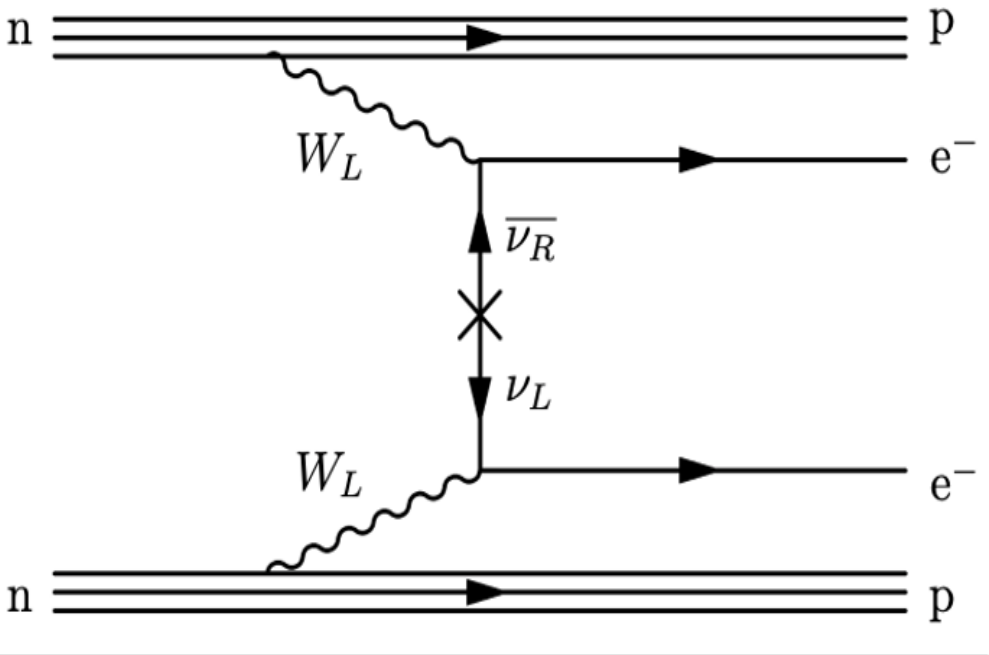

Figure 2.4: Feynman diagram for the forbidden neutrinoless double beta decay ($0\nu\beta\beta$) via the light neutrino exchange (LNE) mechanism [7].

The light neutrino exchange mechanism in figure 2.4 clearly illustrates the Majorana nature of neutrinos, however, amongst the other $0\nu\beta\beta$ mechanisms, neutrinos are often not involved making conclusions regarding the nature of the neutrino less obvious. In 1980, Schechter and Valle [28] illustrated that for any $0\nu\beta\beta$ decay, regardless of the beyond Standard Model intermediary process, neutrinos are Majorana even though they are not directly involved in the decay. The $0\nu\beta\beta$ mechanism can therefore be replaced with a 'Black Box' that is independent of the decay mechanism as shown in figure 2.5.

For $0\nu\beta\beta$ decay, the decay rate takes the form,

$$\left(T_{1/2}^{0\nu}\right)^{-1} = G^{0\nu}\left(Q_{\beta\beta}, Z\right)\left|M^{0\nu}\right|^2 \eta_{LV}^2 \tag{2.9}$$

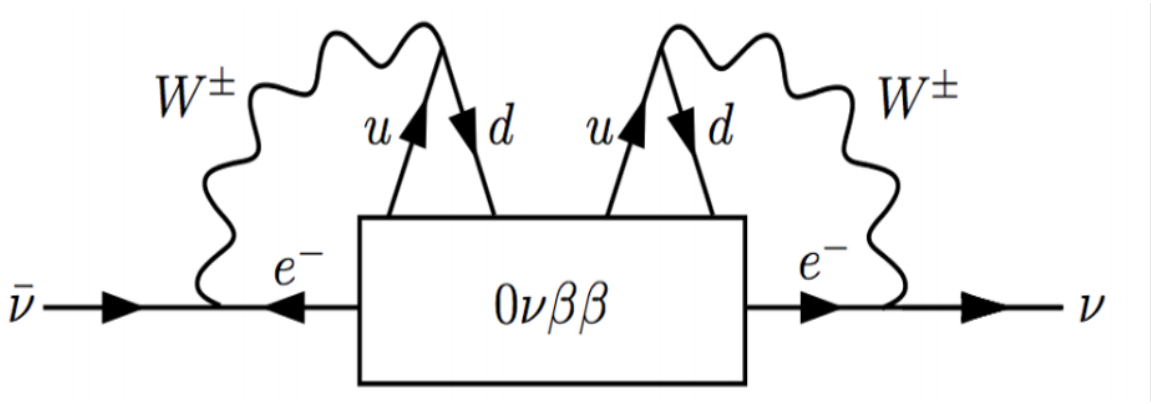

Figure 2.5: Feynman diagram for neutrinoless double beta decay ($0\nu\beta\beta$), illustrating the Majorana nature of neutrinos for any intermediary decay mechanism [28].

where $G^{0\nu}$ is the two particle phase space factor, $M^{0\nu}$ the nuclear matrix element for the neutrinoless decay transmission and η_{LV} the lepton number violating parameter that is unique to each of the decay mechanisms. Light neutrino exchange, right handed current and Majoron emission will be briefly discussed in the following sections, focusing on the relationship between the decay mechanism and the corresponding decay rate.

2.3.1 Light Neutrino Exchange

As mentioned, light neutrino exchange is the proposed interaction that most closely resembles a current Standard Model interaction and is shown by the exchange of a neutrino/antineutrino pair in figure 2.4. If the neutrino is a Majorana particle, the exchanged neutrino and antineutrino are effectively the same particle but with a flip in handedness. A Dirac mass neutrino would be capable of changing handedness via an interaction with the Higgs, with the strength of the interaction proportional to the mass of the neutrino.

The decay rate for this interaction is,

$$\left(T^{0\nu}_{1/2}\right)^{-1} = G^{0\nu}\left(Q_{\beta\beta}, Z\right)\left|M^{0\nu}\right|^2 \langle m_{\beta\beta}\rangle^2 \tag{2.10}$$

where the lepton number violating parameter in equation 2.9, is replaced by the effective Majorana mass $\langle m_{\beta\beta}\rangle$. $\langle m_{\beta\beta}\rangle$ is defines as,

$$\langle m_{\beta\beta}\rangle = \left|\sum_i U^2_{ei} m_i\right| \tag{2.11}$$

and for three light active neutrinos with mass m_i, is equal to,

$$= \left|\cos^2\theta_{13}\left(m_1\cos^2\theta_{12} + m_2 e^{i\alpha_1}\sin^2\theta_{12}\right) + m_3 e^{i(\alpha_2-2\delta)}\sin^2\theta_{13}\right| \tag{2.12}$$

using the PMNS matrix shown in equation 1.4 and the Majorana phases in equation 1.5. From equation 2.12, the decay rate of the light neutrino exchange is sensitive to the absolute scale of the neutrino mass eigenstates. Therefore, if the half-life of neutrinoless double beta decay is measured, the effective mass $\langle m_{\beta\beta}\rangle$ can be determined as shown previously in Figure 1.6.

2.3.2 Majoron Emission

In the standard model of particle physics, there are a number of processes that conserve charge, energy and momentum, however they are still forbidden interactions because they violate other conserved quantities such as the baryon and lepton numbers. Fundamental particles have assigned quantum numbers used to determine whether an interaction is allowed or forbidden. Currently there are no interactions that violate the conservation of baryon or lepton number, but there are extensions of the Standard Model that allow small violations of baryon and lepton conservation as long as the baryon minus lepton (B-L) number is conserved. Example SM extensions include Goldstone Bosons or Majorons, which mediate neutrinoless double beta decay whilst conserving B-L.

$0\nu\beta\beta$ mediated by a single Majoron can be expressed as,

$$(A, Z) \rightarrow (A, Z+2) + 2e^- + \chi^0 \tag{2.13}$$

where χ^0 is the emitted Majoron. The decay rate for the interaction is given by,

$$\left(T_{1/2}^{0\nu\chi^0}\right)^{-1} = G^{0\nu\chi^0}\left(Q_{\beta\beta}, Z\right)\left|M^{0\nu\chi^0}\right|^2\langle g_{\chi^0}\rangle^2 \tag{2.14}$$

where $G^{0\nu\chi^0}$ $M^{0\nu\chi^0}$ are as previously defined, and the lepton number violating parameter in equation 2.9 is exchanged for $\langle g_{\chi^0}\rangle$ which represents the coupling between the Majoron and the neutrino. The Feynman diagram of the decay is shown in Figure 2.6,

The measured total electron energy of the decay can be used to infer the Majoron emitting decay mechanism, however with the addition of emitted particles other than the electron, the energy takes on a continuous spectra similar to that observed with $2\nu\beta\beta$ (Figure 2.3). The shape of the total electron energy spectra is dependent upon the Majoron model used during the decay, which can include up to two different Majorons as shown in figure 2.7

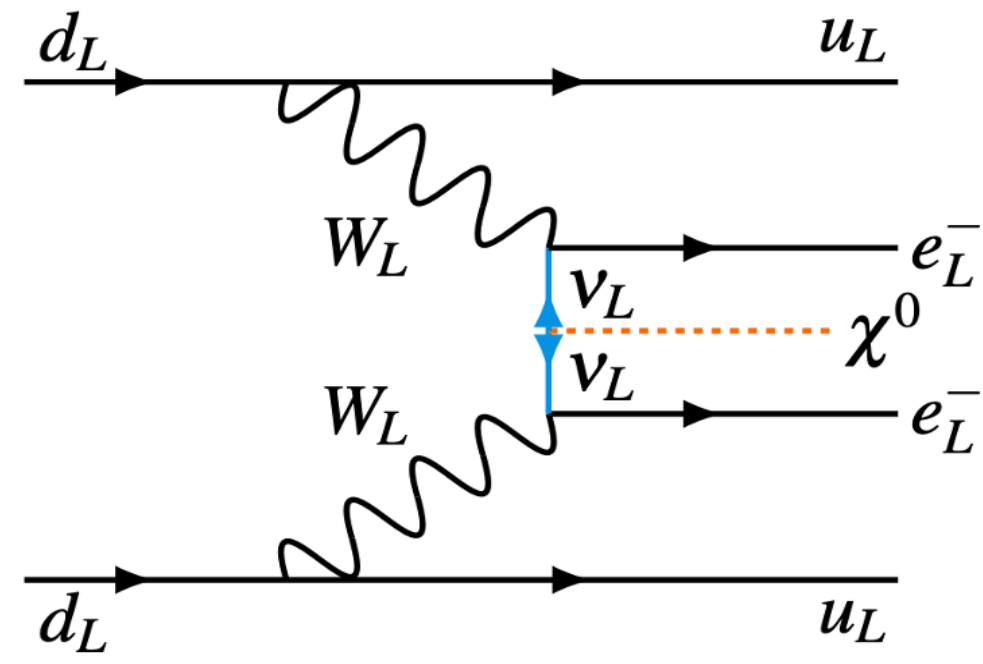

Figure 2.6: Feynman diagram for the forbidden neutrinoless double beta decay ($0\nu\beta\beta$) via the emission of an associated Majoron (χ^0) [30].

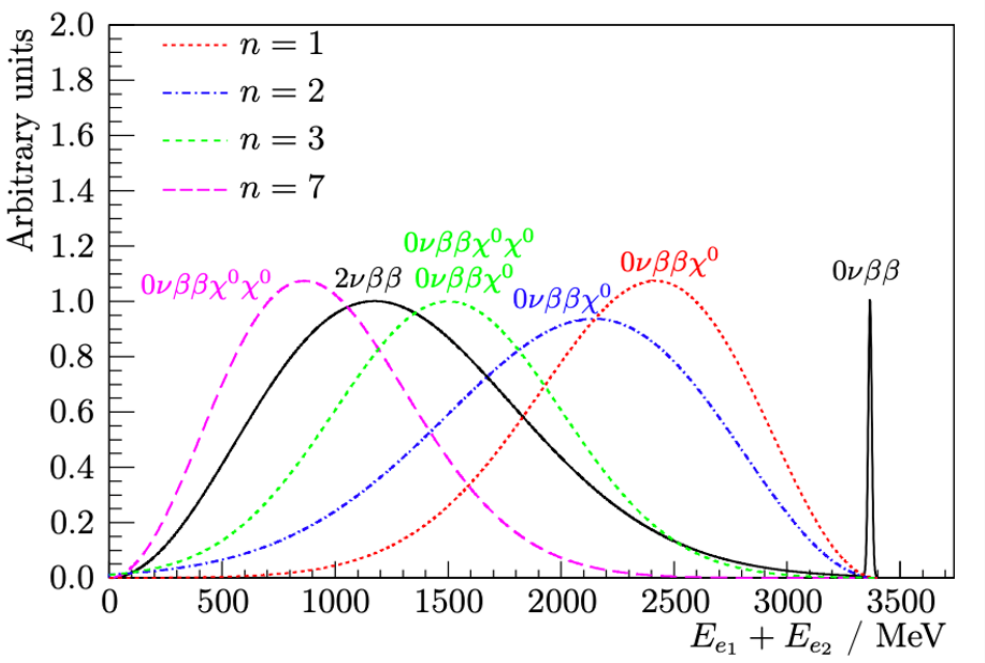

Figure 2.7: $0\nu\beta\beta$ and $2\nu\beta\beta$ energy spectra alongside four alternative Majoron decay modes with indices 1,2,3 and 7 [31].s

2.3.3 Right Handed Currents

Currently, the weak interaction is only propagated by a left handed W boson, however by proposing a right handed component of the weak force, a right handed gauge boson, may mediate a neutrinoless double beta decay with only right handed neutrinos. The hypothesized right handed gauge boson may be related to the W or Z bosons as a mixture of multiple boson states or could manifest as an entirely novel gauge boson. A Feynman diagram of $0\nu\beta\beta$ mediated by a right a right handed W boson and right handed neutrino is shown in figure 2.8 below,

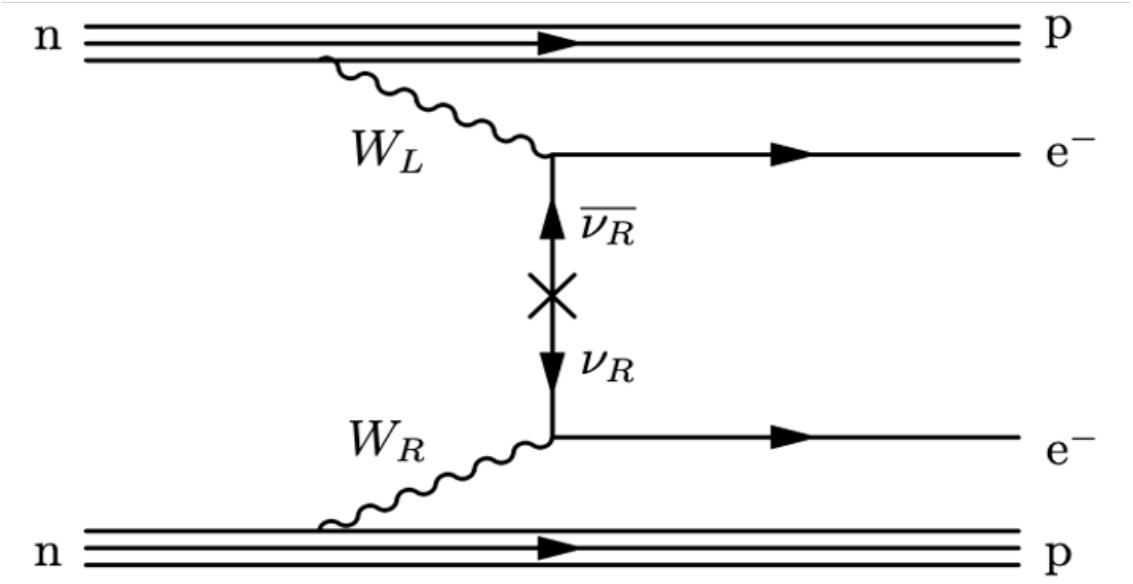

Figure 2.8: Feynman diagram for the forbidden neutrinoless double beta decay ($0\nu\beta\beta$) via the $\langle\lambda\rangle$ right handed weak current mechanism [29].

In figure 2.8, $0\nu\beta\beta$ is mediated by a right handed W boson and right handed neutrino which is a Majorana particle. The alternative decay kinematics may be probed by investigating opening angle and energy distributions as shown in figure 2.9, which highlights the difference in the distributions with changing decay mechanisms. For the purpose of describing the physics of the RH current mechanism, two new parameters are introduced, $\langle\lambda\rangle$, which describes the coupling between right handed leptons and right handed quarks, as shown in Figure 2.8 and $\langle\eta\rangle$, which describes the coupling between right handed leptons and left handed quarks. The two parameters $\langle\lambda\rangle$ and $\langle\eta\rangle$ represent the lepton number violation and are related to the $0\nu\beta\beta$ half-life by the following relations,

$$T^{0\nu\lambda}_{1/2} = G^{0\nu\lambda}\left(Q_{\beta\beta}, Z\right)\left|M^{0\nu\lambda}\right|^2\langle\lambda\rangle^2 \tag{2.15}$$

$$T^{0\nu\eta}_{1/2} = G^{0\nu\eta}\left(Q_{\beta\beta}, Z\right)\left|M^{0\nu\eta}\right|^2\langle\eta\rangle^2 \tag{2.16}$$

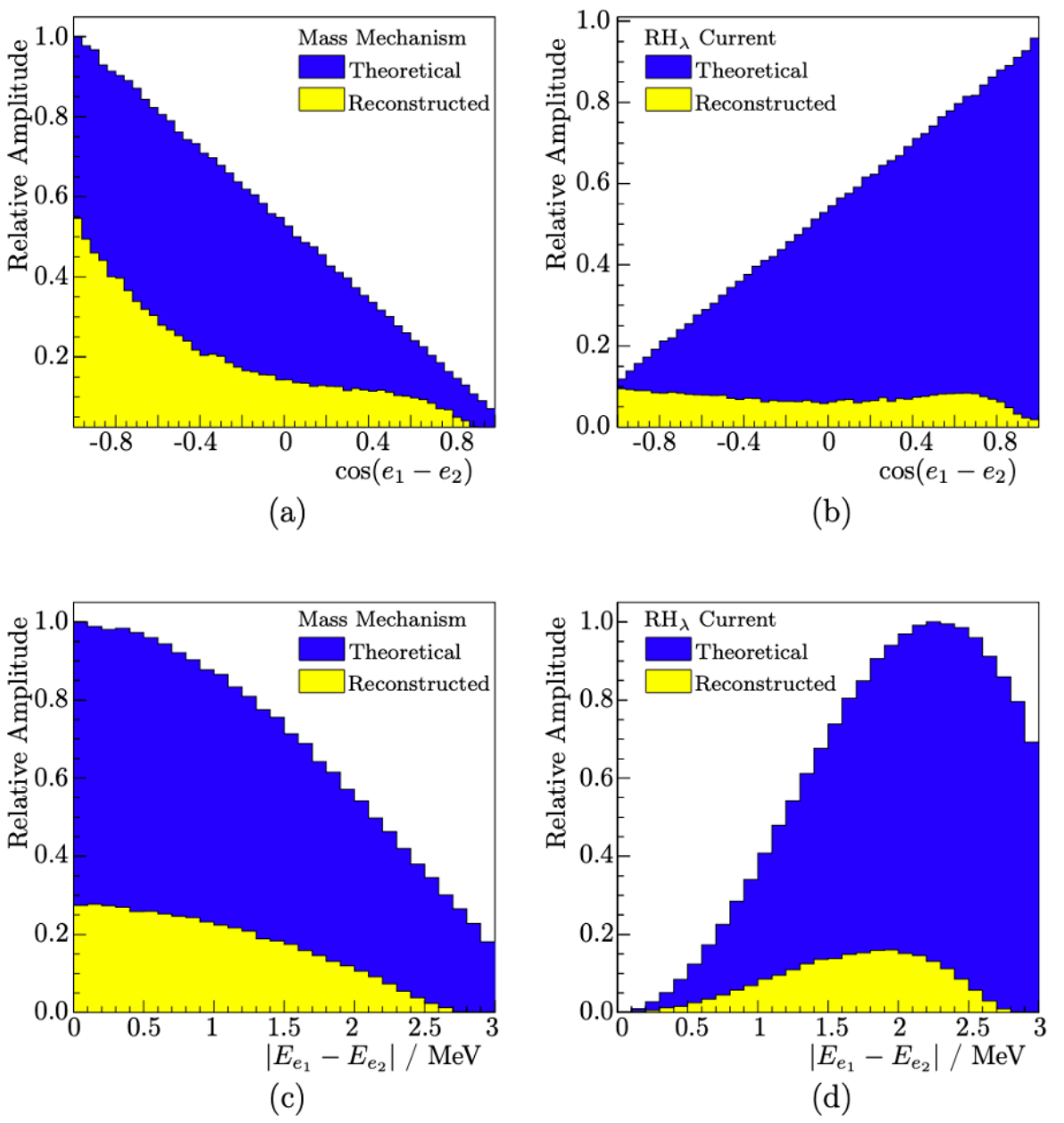

Figure 2.9: Electron energy difference and opening angle distributions for the light neutrino exchange (a,c) and right handed current (b,d) decay modes. The reconstructed distributions illustrate the predicted response from the SuperNEMO detector [32].

2.4 Nuclear Matrix Elements

Nuclear Matrix Elements (NMEs) are a key components for investigating double beta decay as shown in equation 2.9, where using both the NMEs and the measurable decay rate, the absolute neutrino mass $\langle m_{\beta\beta} \rangle$ can be probed for a particular decay mechanism such as light neutrino exchange shown in equation 2.10. By improving the precision of the NMEs calculations, improved limits can be determined for the absolute neutrino mass during double beta decay searches. In order to calculate the NMEs, nuclear structure theory is necessary, beginning with a many body Hamiltonian, which describes the interactions between nucleons. NME calculations are further complicated as the entire range of energy states for the decaying nuclei must be considered and their respective contributions to the transition rate determined to a high degree of accuracy. 5 different approximations [33] for calculating the NMEs will be discussed in the remainder of this section and the level of uncertainly with each model will be presented as a function of the decaying isotope.

- Interacting Shell Model (ISM) [34]: The interacting shell model considers a small number of nuclear orbitals that are closest to the Fermi level, but within each of the lower orbitals, the nucleons behave independently in a self imposed mean field. ISM accurately describes the the interactions between the limited number of nucleons and therefore the model predicts smaller nuclei such as ^{82}Se more accurately. Additionally, as only a few of the orbital shells are considered, the approximations made by the ISM are often on the lower end.

- Quasiparticle Random Phase Approximation (QRPA) [35]: Unlike the ISM, QRPA uses a greater number of different orbitals to calculate the NMEs, however the complexity of the nucleon interactions is reduced to compensate for this. Incorporating an increased number of nuclear orbitals increases the precision of QRPA for larger nuclei. For the purpose of calculating the NMEs, QRPA considers the initial and final states via a number of virtual intermediary states. The proton-proton interaction parameter g_{pp} can be constrained experimentally by measuring the decay rate of the two neutrino decay reducing the uncertainty of the model for $2\nu\beta\beta$, although the reduced uncertainty may not translate directly to the neutrinoless decay.

- Interaction Boson Model (IBM) [36]: The IBM is similar to the shell model approximation but denotes pairs of nucleons as single bosons with angular momentum of either 0 or 2. The advantages of the IBM are similar to that of the ISM however, similarly for large nuclei the uncertainty on the calculations increases.

- Projected Hartree-Fock Bogoliubov (PHFB) [37]: PHFB calculates the transition probability using the nuclear wave functions for neutron pairs with even values of angular moment and positive parity such as $0^+/2^+/4^+$. PHFB includes only quadrupole interactions with fewer model dependant parameters compared to the previous approximations.

- Energy Density Functional (EDF) [38]: The EDF method improves on the simple PHFB method by including the Gogny interaction for nucleons [39].

The different models are used to compute the NMEs of several double beta decaying isotopes, by firstly calculating the NMEs of $\beta^{\pm}$ decay as well as the two neutrino DBD and then estimating the values for $0\nu\beta\beta$ based off the previous measurements, taking into account the different intermediate states of the neutrinoless decay. The results for 11 double beta decay isotopes, using the five NME estimation models described above, are shown in figure 2.10. As mentioned, the different models produce different values for the NMEs and because of this there is a large uncertainty, up to an order of magnitude, between the estimated neutrinoless double beta decay half-lives.

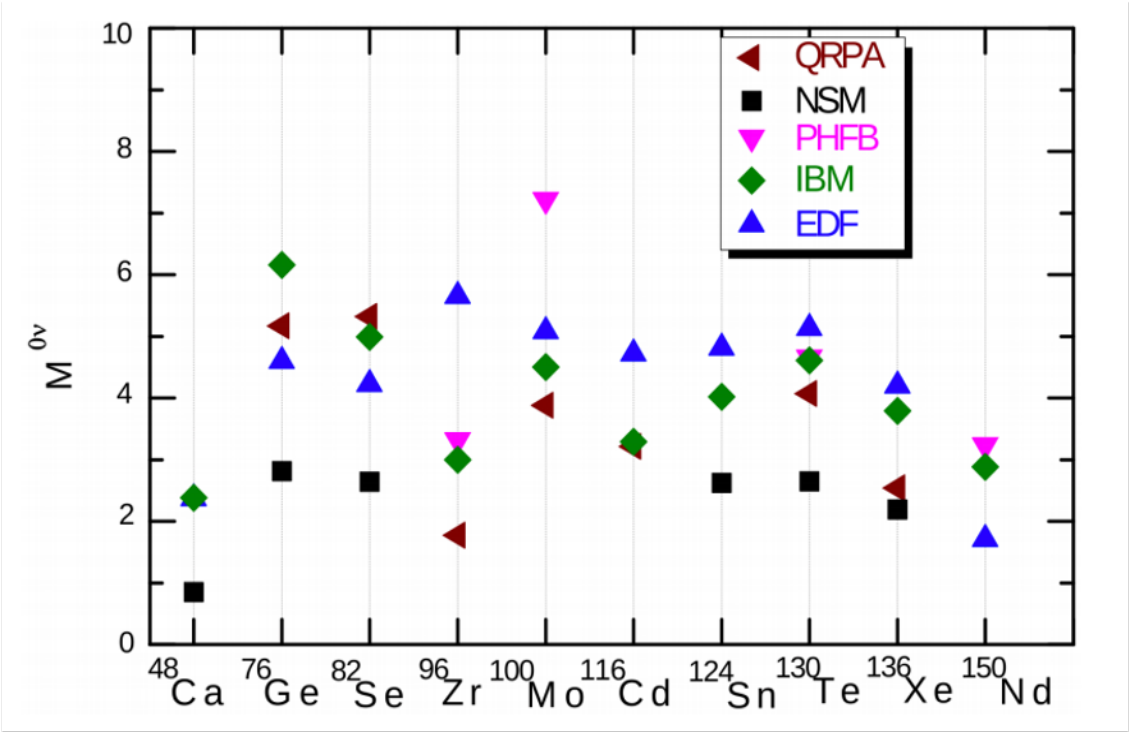

Figure 2.10: Nuclear matrix element (NME) values for the main double beta decaying isotopes used for experimentation, using the different methods described in Section 2.4 [40].

2.5 Experimental Design

Double beta decay experiments look for a potential $0\nu\beta\beta$ (Section 2.3) signal by measuring the kinematics of the beta decay electrons emitted from the source. Simultaneously, the $2\nu\beta\beta$ spectrum is measured and is used to improved the precision of parameters such as the NMEs discussed in Section **??**. The detectors also measure any natural radioactive background for the purpose of background rejection, improving the $0\nu\beta\beta$ half-life sensitivity.

For a $0\nu\beta\beta$ decay, no neutrinos or antineutrinos would be produced and so the total energy of the electrons is expected to be equal to $Q_{\beta\beta}$ (shown by the mono-energetic spectrum in Figure 2.3) and so the region of interest (ROI) for a double beta decay experiment is usually a small energy window, around the decay energy. The width of the ROI is dependent upon the energy resolution of the detector.

The expected half-life sensitivity of an experiment is given by [41],

$$T^{0\nu}_{1/2} > \frac{4.16 \times 10^{26}\text{yr}}{n_\sigma} \left(\frac{\epsilon a M t}{Z}\right) \sqrt{\frac{1}{N_B}} \tag{2.17}$$

with $T^{0\nu}_{1/2}$ the half-life sensitivity to neutrinoless double beta decay, ϵ the signal detection efficiency, a the isotopic abundance, Mt the total exposure of the experiment (kg yrs), n_σ the number of standard deviations for a given confidence limit ($n_\sigma = 1.64$ for 90% CL), Z the molecular weight of the double beta isotope, N_B the number of expected backgrounds events. Equation 2.17 is a simple window method that utilises a Gaussian approximation to calculate a half-life sensitivity $T^{0\nu}_{1/2}$. Modern experiments employ more advance methods, taking advantage of complete energy spectral shapes, however for a comparative estimate of the sensitivity, between different magnetic field configurations, Equation 2.17 is useful.

A $0\nu\beta\beta$ detector should optimise the half-life sensitivity, by maximising the parameters such as the signal detection efficiency and exposure whilst minimising the background contamination. For a background free experiments, which can be established using advanced background suppression techniques and radiopure materials, the half-life sensitivity formula in Equation 2.17 becomes,

$$\left(T^{0\nu}_{1/2}\right) \propto \begin{cases} aM\varepsilon t & \text{background free} \\ a\varepsilon\sqrt{\frac{Mt}{B\Delta E}} & \text{with background} \end{cases} \tag{2.18}$$

2.6 Isotope Choice

Currently there are 13 (***Ref) isotopes that have been observed to undergo double beta decay, however in order to be chosen for use in an experiment searching for neutrinoless double beta decay the isotope should fulfil certain conditions including,

- Readily available at a high mass, with a reasonable cost
- Low atomic mass
- High isotopic abundance or otherwise, a simple enrichment process
- High decay energy with the aim of reducing the prominent low energy backgrounds

Table 2.1 lists the properties of a few commonly used double beta decay isotopes,

Isotope	Natural Abundance (%)	$Q_{\beta\beta}$ MeV
^{48}Ca	0.187	4.263
^{76}Ge	7.8	2.039
^{82}Se	8.7	2.998
^{96}Zr	2.8	3.348
^{100}Mo	9.8	3.035
^{116}Cd	7.5	2.813
^{130}Te	34.08	2.527
^{136}Xe	8.9	2.459
^{150}Nd	5.6	3.371

Table 2.1: Commonly used double beta decaying isotopes with decay energy ($Q_{\beta\beta}$ greater than 2 MeV. The decay energy and natural abundance are provided for each isotope.) [57]

A significant source of backgrounds for neutrinoless double beta decay is the irreducible $2\nu\beta\beta$ high energy tail as $2\nu\beta\beta$ is indistinguishable from $0\nu\beta\beta$ in the ROI. The $2\nu\beta\beta$ background can be suppressed by using an isotope with a high $2\nu\beta\beta$ half life, improving the energy resolution of the detector and maximising the $0\nu\beta\beta$ to $2\nu\beta\beta$ ratio, as shown by the following relation,

$$\frac{S}{B} \propto \left(\frac{Q_{\beta\beta}}{\Delta E}\right)^6 \frac{T^{2\nu}_{1/2}}{T^{0\nu}_{1/2}} \tag{2.19}$$

which also emphasis the significance of using an isotope with a high decay energy and a detector with a high resolution, particularly for isotopes such as ^{76}Ge which has a relatively low decay energy (Table 2.1).

The most prominent backgrounds for double beta decay searches are the naturally occurring radioisotopes from the uranium and thorium decay chains, commonly found in detector construction materials. Although materials are purified prior to construction, low levels of these isotopes remain and decay into problematic backgrounds. The most harmful decay progeny are ^{208}Tl and ^{214}Bi which occur from the ^{232}Th and ^{238}U/^{222}Rn decay chains respectively. ^{208}Tl has a decay energy of 4.99 MeV including a high energy 2.615 MeV γ which lies within the ROI of many double beta decay isotopes. Gamma particles are particularly problematic as they are able to penetrate a detector from an external source and deposit energy. ^{214}Bi undergoes β decay with an energy of 3.27 MeV and can also mimic double beta decay (Section 6.1). Tha majority of $\beta\beta$ isotopes have $Q_{\beta\beta}$ less than 3 MeV, hence, any experiment using those isotopes should have sufficient background rejection techniques in order to remove ^{208}Tl/^{214}Bi and low energy backgrounds. Background sources for SuperNEMO, including ^{208}Tl and ^{214}Bi, will be discussed further in Section 3.3.

Unfortunately, no single isotope stands out from among the double beta decaying isotopes and so, in order to maximise the half-life sensitivity of a detector, an isotope should be chosen so that it maximises as many physical parameters as possible, whilst also providing the scaling potential to hold a large amount of source material, increasing the exposure of the experiment. Current experiments study a variety of different isotopes which provides the additional benefit of reducing the uncertainty in the NMEs (Section 2.4), to better understand the translation between the two neutrino and neutrinoless double beta decays of the isotopes.

Previous double beta decay experiments measured the decay progeny of $\beta\beta$ decaying isotopes to infer data about the decaying particle, however current technology allows for the decay electrons to be directly measured (Section 2.7.1) so that the electron kinematics can be determined. Moreover, current detectors can measure the trajectories and topologies of particles, increasing the rate of rejection for α and γ backgrounds. Ultimately, the choice of isotope will depend upon experimental design and a combination of the factors mentioned at the beginning of the section, with the aim of maximising the half-life sensitivity to the $0\nu\beta\beta$ of the chosen isotope.

2.7 Experimental Overview

$0\nu\beta\beta$ searches first began in the 1960s [58, 59], first deploying a few grams of double beta decaying material and recording half-life sensitivities of the order 10^{20}. As time went on, detector technologies improved, increasing the source mass and signal detection efficiency whilst reducing the background contamination. Present day experiments are now capable of setting half-life limits of the order 10^{25} for $0\nu\beta\beta$ and measure $2\nu\beta\beta$ half-lives for the 13 [60] currently observed double beta decaying isotopes. A summary of the current half-life limits and corresponding effective neutrino mass for the light neutrino exchange model (Section 2.3.1) is shown in Table 2.2. The remainder of this section will briefly discuss the detector technologies used by previous, current and future $0\nu\beta\beta$ experiments and the latest results shown in Table 2.2 will be contextualised.

Isotope	$T^{0v}_{1/2} \times 10^{25}$ years)	$\langle m_{\beta\beta} \rangle \, eV$	Experiment
^{48}Ca	$> 5.8 \times 10^{-3}$	$< 3.5 - 22$	ELEGANT-IV
^{76}Ge	> 18	$< 0.08 - 0.18$	GERDA
	> 2.7	$< 0.20 - 0.43$	MAJORANA DEMONSTRATOR
^{82}Se	$> 3.6 \times 10^{-2}$	$< 0.89 - 2.43$	NEMO-3
^{96}Zr	$> 9.2 \times 10^{-4}$	$< 7.2 - 19.5$	NEMO-3
^{100} Mo	$> 1.1 \times 10^{-1}$	$< 0.33 - 0.62$	NEMO-3
^{116}Cd	$> 2.2 \times 10^{-2}$	$< 1.0 - 1.7$	Aurora
^{130}Te	> 2.2	$< 0.09 - 0.31$	CUORE
^{136}Xe	> 10.7	$< 0.061 - 0.165$	KamLAND-Zen
	> 3.5	$< 0.08 - 0.24$	EXO-200
^{150}Nd	$> 2.0 \times 10^{-3}$	$< 1.6 - 5.3$	NEMO-3

Table 2.2: The best half-life limits (90% CL) and the corresponding effective mass $\langle m_{\beta\beta} \rangle$ for each $0\nu\beta\beta$ isotopes used in ongoing experiments [56].

olny have t1/2 and not mev

Commonly used double beta decaying isotopes with decay energy ($Q_{\beta\beta}$ greater than 2 MeV. The decay energy and natural abundance are provided for each isotope.

2.7.1 Direct and Indirect Detector Experiments

Neutrinoless double beta decay experiments are generally divided into direct or indirect searches. Direct detector double beta decay experiments involve measuring the energy of the electrons emitted during the decay. Measuring the individual energies (and trajectories) of the decay electrons is one of the primary benefits of the SuperNEMO detector compared to its competitors, as it allows for the underlying decay mechanism to be probed. Direct detector experiments can be constructed as homogenous (active source), where the source is one of the detection components or heterogeneous (passive source), where the source is not part of the detection components.

Examples of homogeneous experiment detectors include liquid scintillators (such as KamLAND-Zen or SNO+ [61]), bolometers [62] and semiconductor (COBRA, Majorana and GERDA [63]). The principal benefits of homogenous detector experiments include high energy resolution and detector efficiency, whilst maintaining a compact detector structure which limits the natural radioactivity. Heterogeneous detector experiments, such as SuperNEMO, measure the energy, trajectory, time coincidences, vertices and opening angles of double beta decay electrons, however this comes at the cost of reduced energy resolution. Heterogeneous experiment detectors include tracker-calorimeter (SuperNEMO [53]) and time projection chambers (NEXT [64]).

Indirect detection searches use radiochemical and geochemical approaches to analyse isotopes that are capable of undergoing double beta decay. Radiochemical and Geochemical approaches are denominated as indirect searches because they do not directly measure the beta electrons but merely the decay progeny. As a result, indirect experiments are incapable of differentiating between $0\nu\beta\beta$ and $2\nu\beta\beta$ but can precisely measure the $2\nu\beta\beta$ half-life.

2.7.2 Semiconductor Experiments

High Purity Germanium (HPGe) detectors, enriched with ^{76}Ge, currently provide the most feasible technology for semiconductor detectors due to the use of HPGe detectors in γ ray spectroscopy. Alternate technologies include CdZnTe [65] and Complementary Metal Oxide Semiconductors (CMOS) pixel arrays [66], however they are currently still undergoing R&D and are not expected to be utilized for the next generation of detectors, particularly as their scalability is limited.

Semiconductors are grown, bottom up, as crystals and are therefore innately low in impurities and natural radioactivity, but suffer from low scalability as a result of the production process. Germanium semiconductors can be enriched with ^{76}Ge in order to produce a source-as-detector construction, with the source itself acting as a detector. The primary benefit of ^{76}Ge enriched materials is the improved energy resolution, achieving as much as 0.12% FWHM at $Q^{\beta\beta}$ [67] and increased signal detection efficiency.

The previous generation of ^{76}Ge experiments, Heidelberg-Moscow (170) [68] and IGEX (171) [69], set half-life limits of $T^{0\nu}_{1/2} > 1.85 \times 10^{25}$ years and $T^{0\nu}_{1/2} > 1.57 \times 10^{25}$ years which was improved

upon by the current generation of ^{76}Ge experiments, GERDA and the Majorana demonstrator. GERDA [70] and the Majorana demonstrator [71] improved upon the previous experiments, using point-contact HPGe detectors [72], that are capable of differentiating between single and multi site background events improving background suppression.

- **^{76}Ge: GERDA**

The Germanium Detector Array (GERDA), based in the Laboratori Nazionali del Gran Sasso (LNGS) in Laquila, like the Heidelberg-Moscow detector, which ran between 1990 and 2003. GERDA ran in two phases, with Phase I running from 2011 to 2013 and Phase II from 2015 to 2019. During Phase I, detectors from the Heidelberg-Moscow and IGEX experiments were deployed and supported a total of 17.8 kg of source material. An additional 3.6 kg of source was added during the phase, increasing the total source mass to 21.4 kg. Phase I concluded with an exposure of 21.6 kg yrs, resulting in a half-life limit of $T^{0\nu}_{1/2} > 2.1 \times 10^{25}$ years [73].

As mentioned, Phase II commenced in 2015, using a total enriched detector mass of 35.8 Kg and improved background rejection tool. Implementing the improved background rejection reduced the background level to $(1.0^{+0.6}_{-0.4}) \times 10^{-3}$ cts keV^{-1} kg^{-1} y^{-1} [74]. Phase II achieved a half-life limit of $T^{0\nu}_{1/2} > 1.8 \times 10^{26}$ years (90% CL) for ^{76}Ge for a total exposure od 127.2 kg yrs.

- **^{76}Ge: Majorana Demonstrator**

The Majorana demonstrator is located at the 4850 ft level of the Sanford Underground Research Facility, Lead San Diego, USA. Like GERDA, the Majorana experiment studies the neutrinoless double beta decay of ^{76}Ge, using 29.7 kg of germanium, enriched to 88% of ^{76}Ge [**?**]. Data taking began in 2015 and by 2018, the half-life limit for the detector was set at $T^{0\nu}_{1/2} > 2.7 \times 10^{25}$ years (90% CL) with an established background count of $4.7 \pm 0.8 \times 10^{-3}$ cts keV^{-1} kg^{-1} y^{-1} for 26 kg yrs pf exposure. At the same time, the energy resolution was measured to as 2.53 ± 0.08keV FWHM.

- **^{76}Ge: LEGEND**

The Large Enriched Germanium Experiment for Neutrinoless double-beta Decay (LEGEND) collaboration hopes to build upon the success of GERDA and Majorana, using the previously

developed technology to increase the scale of ^{76}Ge based, ultra low background, high resolution semiconductor detectors. LEGEND will attempt to construct a tonne scale detector increasing the relative exposure many fold compared to previous ^{76}Ge based experiments, with the aim of achieving a half-life sensitivity of around 10^{28} years. The initial phase (LEGEND-200), will utilize and improve the previous infrastructure from GERDA, increasing the capacity of the detector to 200 kg of enriched ^{76}Ge. LEGEND-200 is projected to achieve a half-life sensitivity of the order 10^{27} for an expected exposure of 1 t yrs [76] and has started data taking as of 2021 [76].

2.7.3 Scintillation Experiments

Although many experiments utilise scintillators, scintillation experiments are homogenous detectors that combine the source with scintillation medium. For double beta decay searches, the scintillation medium acts as a detector, producing light upon excitation from the emitted double beta electrons. Scintillator light is then captured by photomultiplier tubes (PMTs) which convert the light into a readable signal. The scintillation medium can be either solid, liquid or gas, be produced organically or inorganically and are relatively inexpensive, radiopure and scalable.

Scintillator detectors are composed of two main materials, a solvent and a fluor. Within the solvent, which represent the majority of the volume in the detectors, scintillation occurs from propagating charged particles and the fluor has the role of absorbing the scintillation light, then reabsorbing at higher wavelengths better suited to the photodetectors. Examples of fluors include POPOP (,4-Bis(5-phenyloxazol-2-yl)benzene) and PPOs (2,5-Diphenyloxazole).

Two previous examples of homogeneous experiments are ELEGANT VI and CANDLES III which studies the double beta decay of ^{48}Ca. ELEGANT VI used a total of 7.6 g of ^{48}Ca inside of CaF_2 crystal scintillators, for a total exposure of 0.015 kg yrs and a half-life limit of $T^{0\nu}_{1/2} > 5.8 \times 10^{22}$ years [77]. CANDLES III followed on from ELEGANT VI, but used a liquid scintillator which also provided the active shielding. 350g of ^{48}Ca was used and an ultra low background count of 10^{-3} cts keV^{-1} kg^{-1} y^{-1} [78].

- **^{136}Xe: KamLAND-Zen**

KamLAND-Zen (Kamioka Liquid scintillator AntiNeutrino Detector-Zero neutrino) is located at the Kamioka Observatory in the Gifu prefecture of Japan and probes the neutrinoless double beta decay of ^{136}Xe. The KamLAND-Zen detector is a liquid scintillator, using enriched ^{136}Xe (90%), loaded into a liquid scintillator mixture of 82% decane and 18% pseudocumene by volume. 2.7g/l of PPO is added as a fluor. The mixture of ^{136}Xe and the the liquid scintillator (Xe-LS) is held in a 25 μm thick nylon 'mini balloon', suspended at the centre of the 13m diameter 'main balloon', which is filled with liquid scintillator. The 'main balloon' is positioned inside of an 18m wide stainless

steel spherical vessel, filled with non-scintillating buffer oil. Light signals are collected and read by 1879 17" and 20" PMTs that are on the vessel. The entire assembly is surrounded by a 3.2 kt water-Cherenkov detector to veto muon decays.

Phase I of KamLAnd-Zen, known as KamLAND-Zen 400, loaded 320 Kg of enriched ^{136}Xe with the liquid scintillator. The background ^{110m}Ag, which undergoes β decay, limited the sensitivity of the experiment [79] and was believed to be fallout from the Fukushima nuclear disaster in 2011 [80]. Prior to phase II the Xe-LS mixture was purified in order to reduce the contamination. Phase II ran with 380 Kg of enriched xenon with a total exposure of 504 Kg yrs, resulting in a $0\nu\beta\beta$ half-life sensitivity of $T^{0\nu}_{1/2} > 1.07 \times 10^{26}$ years (90% CL) [81].

A new, larger and more radiopure nylon 'mini balloon' was installed and is capable of holding 750 Kg of enriched ^{136}Xe for the following iteration of KamLAND, KamLAND-Zen 800. Data taking began on January 2019, following purification of the Xe-LS mixture from phase II of KamLAND-Zen 400 and updated background rejection tools. Currently, preliminary data following 132.7 days of data taking brought about a lower limit for the neutrinoless double beta decay of 4×10^{25} years (90% CL) [82] for ^{136}Xe. KamLAND-Zen 800 hopes to eventually achieve a half-life sensitivity of 2×10^{27} years after five years of runtime.

- **^{130}Te: SNO+**

SNO+ is the *** to the SNO (Sudbury Neutrino Observatory) experiment and is located at SNOLAB in Sudbury, Ontario, Canada. SNO+ uses the original SNO detector, which was a heavy water filled container that studied solar neutrinos, but fills the 12m acrylic sphere with 780 tons of a liquid scintillator, made up of a mixture of Liquid Alkyl Benzene (LAB), 2 g/l of PPO as a fluor and 3.8 tons of unenriched tellurium, with the high natural abundance of ^{130}Te (34%) resulting in over 1300 Kg of ^{130}Te. The acrylic sphere is shielded by water and instrumented with 9500 PMTs.

SNO+ will be run in three different phases including: a water phase; a scintillator phase and finally a tellurium phase. The water phase involves running the SNO+ detector as a pure Cherenkov water detector in order to perform the commissioning for the water shielding. The scintillator phase includes loading the detector with just the liquid scintillator to characterize the backgrounds and properties of the scintillation material. Finally, the tellurium phase will commence once the tellurium is added to the detector and will signal the beginning of data taking for the neutrinoless double beta decay of tellurium. Once the tellurium is added to the detector, data taking is expected to take place over 5 years resulting in an exposure of over 6500 Kg yrs and a corresponding $0\nu\beta\beta$ half-life sensitivity of $T^{0\nu}_{1/2} > 1.9 \times 10^{28}$ years (90% CL) [83]. Presently the water phase has been completed and the scintillator phase is expected to begin shortly.

2.7.4 Bolometer Experiments

Bolometer experiments refer to experiments wherein bolometers measure small increments in temperature that occur when the energy from a radioactive decay is observed. Bolometers are operated at cryogenic temperatures around 10 mK. At low temperatures, the heat capacity of a material is more sensitive to changes in temperature therefore, operating bolometers at low temperatures increases the energy resolution. The sensitive region of a bolometer detector is known as an absorber and is thermally connected to a low, constant temperature thermal reservoir. The change in temperature recorded by the absorber as a result of absorbing the decay energy can then be measured before the absorber recalibrates to the temperature of the reservoir.

Bolometer absorbers are grown as crystals, similar to semiconductors, using double beta decaying isotopes. The crystalline growth process ensures that the natural radioactivity is low. Examples of crystalline materials used in bolometers includes $^{130}TeO_2$, $^{116}CdWO_4$, $Zn^{82}Se$, $^{40}Ca^{100}MoO_4$, $Li_2^{100}MoO_4$, and $Zn^{100}MoO_4$.

Bolometer experiments benefit from having good energy resolution, given the temperature and noise from temperature fluctuations are controlled. Additionally, bolometers have superior counting statistics in the phonon channel. It has been shown that bolometers can reach an energy resolution of around 5 keV FWHM, at 2615 keV, which is comparable to the high energy resolution seen with High Purity Germanium (HPGe) detectors [84]. Bolometers do however suffer from limited scalability as increasing the size of the self shielding of the crystals and increases the difficulty of maintaining a low temperature environment. Moreover, solely using bolometry limits the particle identification and therefore background suppression as only a single energy readout is given.

- **^{130}Te: CUORE**

The Cryogenic Underground Observatory for Rare Events (CUORE) experiment is the successor to CUORICINO, which investigated the double beta decay of ^{130}Te using array of 62 TeO^2 crystals, from 2003 to 2008. A total of 507g of ^{130}Te was maintained at cryogenic temperatures using a dilution refrigerator and achieved a total exposure of 19.75 Kg yrs and achieved a corresponding half-life sensitivity of $T^{0\nu}_{1/2} > 2.8 \times 10^{24}$ [85]. CUORE is based at the LNGS and makes use of 988 5×5×5 cm^3 absorber crystals, each containing 750g of TeO^2 and cooled to a temperature of 7 mK. Like SNO+, CUORE uses unenriched tellurium, choosing to exploit the high natural abundance of ^{130}Te, resulting in the total mass of double beta decaying ^{130}Te to be around 250 Kg. Following an initial 2 months of data taking, for an exposure of 86.3 Kg yrs, setting a half-life limit of $T^{0\nu}_{1/2} > 1.3 \times 10^{25}$ years (90% CL) [86]. An energy resolution of 7.7 ± 0.5 keV FWHM was achieved at $Q_{\beta\beta}$ and a background level of 0.014 ± 0.002 counts keV^{-1} Kg^{-1} $yrrs^{-1}$ was measured. The combined limit using data from CUORICINO [85] and CUORE-0 [87] improves the limit to

$T^{0\nu}_{1/2} > 1.5 \times 10^{25}$ (90% CL). CUORE is expected to reach a sensitivity of $T^{0\nu}_{1/2} > 9 \times 10^{25}$ years following five years of runtime [88].

- **^{82}Se, ^{100}Mo and ^{130}Te: CUPID**

As mentioned, the particle identification and subsequent background suppression is limited for bolometer experiments such as CUORE, however the CUORE Upgrade with Particle IDentification (CUPID) collaboration attempts to improve on the CUORE design by implementing improved background rejection via active particle identification [**?**] by detecting the minute Cherenkov light signal from charged particles propagating through the TeO_2 crystal [90]. A second approach interchanges the absorber for a scintillating material such as $Zn^{82}Se$ (used in CUPID-0 [91]) or $Zn^{100}MoO_4$ and $Li_2^{100}MoO_4$ (used in LUMINEU [92]). CUPID-0 and LUMINEU are two research and development projects and part of the CUPID project, investigating the practicability of using scintillating materials as bolometers. CUPID aims to reach a background level of 0.1 counts t^{-1} $yrs^{-1}$and a half-life limit of $T^{0\nu}_{1/2} > 10^{27} - 10^{28}$y [93].

- **^{100}Mo: AMoRE**

The Advanced Molybdenum based Rare process Experiment (AMoRE), located at the Yangyang Underground Laboratory (Y2L) in South Korea, is investigating the neutrinoless double beta decay of ^{100}Mo. AMoRE uses calcium molybdate scintillating crystal bolometers enriched to 95% ^{100}Mo [94]. In order to measure the temperature change and light output from particles interacting with the crystalline structure, Metallic Magnetic Calorimeters (MMCs) are attached to the crystals and are coupled to a gold film on a germanium wafer. Phonons generated from light absorption are collected by the gold film and then measured. Monitoring the temperature and light output ensures a high energy resolution and particle identification.

AMoRE-pilot, which ran as a pilot phase between 2015 and 2018, reached a half-life sensitivity of $T^{0\nu}_{1/2} > 9.5 \times 10^{22}$ years following 111 Kg yrs of exposure. The upcoming two phases are AMoRE-I and AMoRE-II and expect to load 5 Kg of depleted $^{48}Ca^{100}MoO_4$ crystals and 200 Kg of ^{100}Mo based crystals, with a corresponding expected half-life sensitivity of $T^{0\nu}_{1/2} > 10^{25}$y and $T^{0\nu}_{1/2} > 5 \times 10^{26}$y, respectively [95].

2.7.5 Time Projection Chambers

Time Projection Chambers (TPCs) benefit from easy mass scalability and good background discrimination making it an ideal technology for investigating neutrinoless double beta decay. TPCs use a gas or liquid filled volume, that undergoes ionisation from passing charged particles. An applied electric field causes the ionized particles to drift towards a collector which is capable of measuring the initial position of the ionization. The addition of scintillating material alongside the drifting ions confers the position, energy and topology of a decay. Furthermore, the ionization to scintillation ratio can be used to differentiate between α, β and γ particles, alongside the track lengths and timing information.

^{136}Xe is a suitable choice of isotope, for both the source and detection medium (homogenous detector) due to its availability and ease of scalability. The TPCs can accommodate both liquid and gas phases of ^{136}Xe and have been shown to achieve an energy resolution of 0.5% FWHM at $Q^{\beta\beta}$ [96]. Two phase xenon TPCs are also used for dark matter searches, such as DARWIN [97], which may in fact be able to search for $0\nu\beta\beta$, with a proposed half-life sensitivity of 8.5×10^{27} years (90% CL) with an expected exposure of 140,000 Kg yrs, equivalent to tonne scale sole $0\nu\beta\beta$ searches. Dark matte detectors are usually low energy threshold detectors, whereas $0\nu\beta\beta$ searches are optimised to maximise the energy resolution and minimise the the background count, making the single phase detectors the ideal choice.

- **^{136}Xe: EXO-200**

EXO-200 was a prototype of the Enriched Xenon Observatory (EXO) experiment and was located at the Waste Isolation Pilot Plant near Carlsbad, New Mexico, USA. EXO-200 used a homogenous liquid xenon TPC, loaded with 110 Kg of xenon enriched to 80.6% of ^{136}Xe and operated at a temperature of 167 K [98]. Scintillation light produced from propagating charged particles was read by avalanche photodiodes and detector planes holding crossed wire grids collected the ionised particles.

EXO-200 had two phases of data taking, with Phase I beginning in 2011and concluded with the the first reported observation of ^{136}Xe double beta decay [99]. Phase I was prematurely ended as a result of a fire in 2014 however Phase —— swiftly recommenced in 2016 and ran for two years. Phase II ultimately resulted in a $T^{0\nu}_{1/2}$ limit of 1.8×10^{25} years (90% CL) [100]. Moreover, EXO-200 exhibited an energy resolution of 2.90% FWHM at $Q_{\beta\beta}$, with a background level of $1.6 \pm 0.2 \times 10^{-3}$ cts keV^{-1} kg^{-1} y^{-1} in the ROI.

- **^{136}Xe: nEXO**

nEXO is the proposed successor to EXO-200 and is expected to be a tonne-scale liquid (single phase) xenon TPC, which will hold 5000 Kg of enriched xenon (90% ^{136}Xe). Using low noise silicon photomultiplier tubes (SiPMTs) in order to collect scintillation light, the energy resolution is expected to improve from EXO-200, to 2.4% FWHM at $Q_{\beta\beta}$. nEXO is expected to reach a half-life sensitivity of around 10^{28} years [**?**]. The improved energy resolution and background suppressing capabilities of nEXO are expected to reduce even the $2\nu\beta\beta$ background to negligible levels.

- **^{136}Xe: NEXT**

The Neutrino Experiment with a Xenon TPC (NEXT) is a prospective TPC detector, using a high pressure gas (single phase) ^{136}Xe TPC and will be located at the Laboratorio Subterraneo de Canfranc (LSC) in Spain. The initial version of the detector (NEXT-100), is expected to deploy 100 Kg of enriched ^{136}Xe at a pressure of 15 bar and will be capable of reconstructing β electrons and importantly will be sensitive to increases in energy deposition, that are observed with double beta decays as the electrons become non-relativistic, acting as a significant background tool.

Surrounding PMTs will measure the scintillation light and an array of SiPMTs will be used to reconstruct the charged particle tracks. NEXT-100 is projected to reach a half-life sensitivity of 2.8×10^{25} years (90% CL), with an initial background rate of 4×10^{-4} cts keV^{-1} kg^{-1} y^{-1} and after three years of running.

2.7.6 Tracker-Calorimeter Experiments

Tracker-Calorimeter experiments isolate the source material from the detector components used to probe the the emitted particles. The tracker volume allows the decay progeny to travel for a short amount of time before reaching the calorimeters, wherein they come to rest and deposit their energy which is then measured. The tracker should also be capable of measuring the trajectory of a passing particle using a combination of gases which allow the particle to easily propagate whilst accurately measuring its trajectory from the interactions with the gaseous mixture. The topological information gained from particles passing through the tracker is important for background suppression and particle identification, even with the accommodating reduction in energy resolution. Additional benefits of the tracker-calorimeter structure include; being able to measure the opening angle between the beta electron pair as well as the individual particle energies, both of which are key factors for studying the underlying neutrinoless double beta decay mechanism.

NEMO-3 was the only detector with a tracker-calorimeter construction, prior to the completion of the SuperNEMO demonstrator module. NEMO-3 ran during 2003-2011, collecting data for

various double beta decaying isotopes, ^{100}Mo, ^{82}Se, ^{130}Te, ^{116}Cd, ^{150}Nd, ^{96}Zr and ^{48}Ca. The NEMO-3 detector was capable of successfully reconstructing the trajectory and measuring the energies of the $2\nu\beta\beta$ electrons for the constituent isotopes. ^{82}Se was selected as the isotope of choice for SuperNEMO, however the structure of the SuperNEMO enables the source to be replaced without deconstructing the detector.

- **^{82}Se: NEMO-3**

NEMO-3 was the successor to the NEMO-1 and NEMO-2 [102] experiments and was constructed in the underground Laboratoire Souterrain de Modane (LSM) in south east France. As mentioned NEMO-3 ran during 2003-2011, with seven double beta decaying isotopes studied. NEMO-3 had a toroidal structure, split into multiple sections, with each section housing a thin foil of double beta decaying material. The source foils were placed in the middle of each section, surrounded by a tracker comprised of low pressure gas and tracking wires. The toroidal structure of NEMO-3 is shown in Figure 2.11, with reference to the source foils, tracker and calorimeters. Borated water and wood encompassed the entire detector and acted as shielding against neutrons.

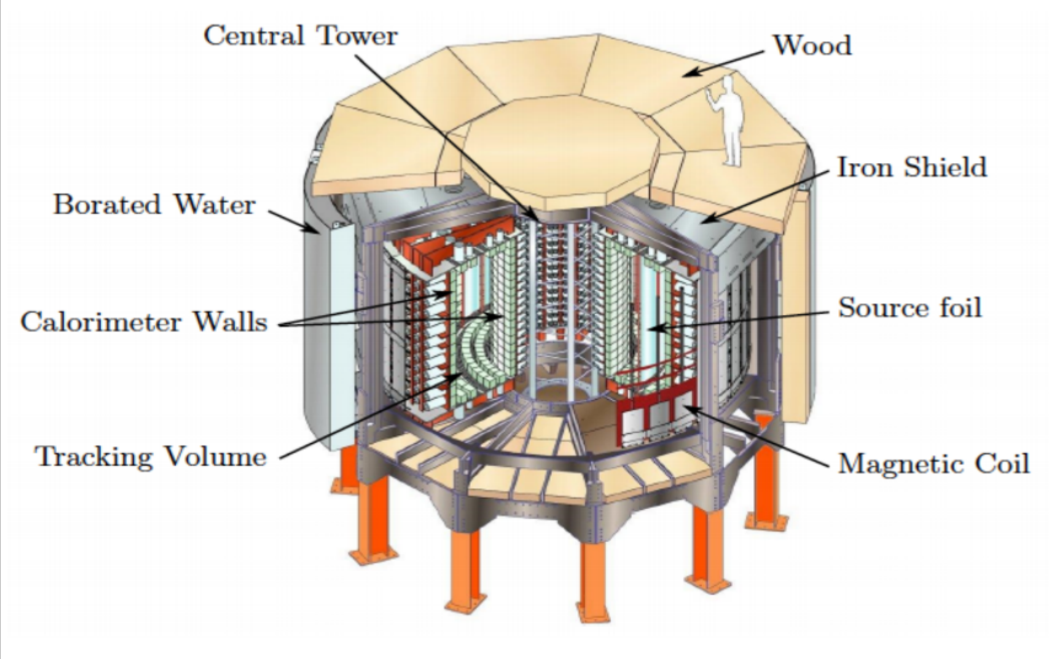

Figure 2.11: Open view of NEMO-3, illustrating the structure and the key components of the detector [56].

Calorimeters were installed around the source foils to allow the emitted electrons to traverse

through the tracker volume before coming to rest inside of the calorimeters. NEMO-3 was capable of accurately reconstructing the trajectory of the electrons, using data from the tracker. Figure 2.12 visualises a real ^{100}Mo double beta decay with a vertex on the source foil and two corresponding charged particle tracks and calorimeter hits.

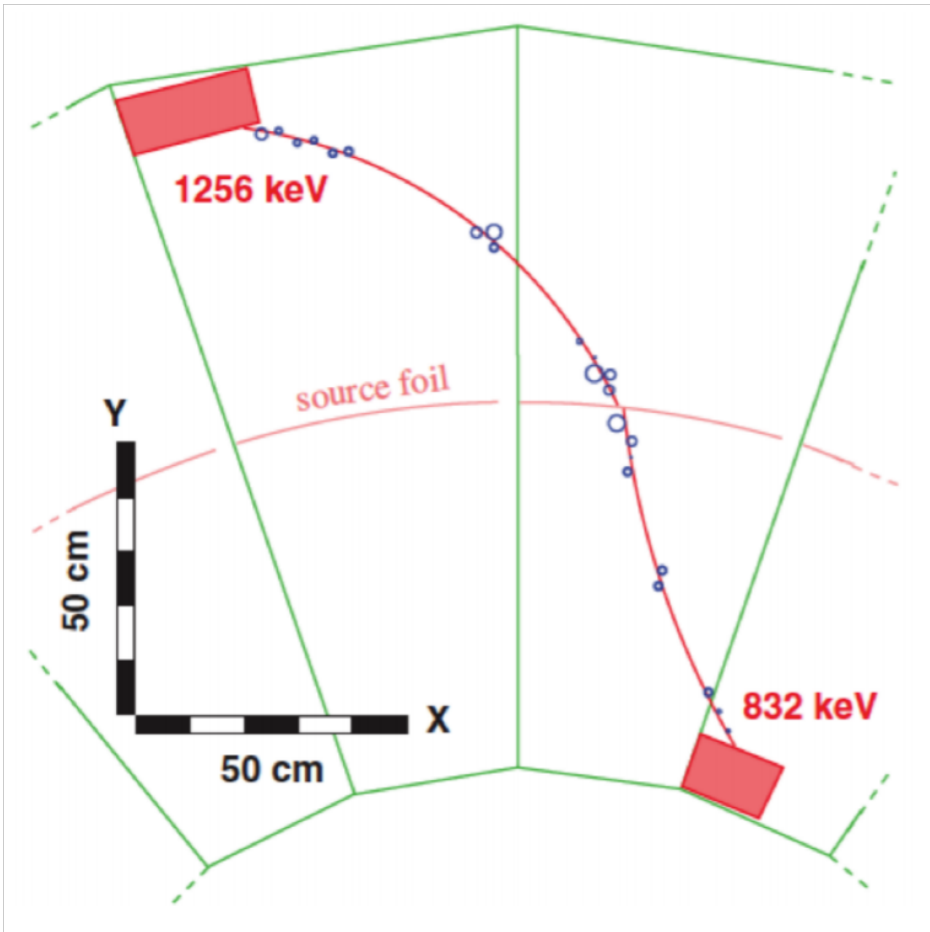

Figure 2.12: NEMO-3 events display, showing a two electron event originating from the source foil. The topology and energy of the electrons indicates the event is a ^{100}Mo double beta decay [103].

^{100}Mo was the main focus of the NEMO-3 experiment, with a total of 6.9 Kg of source material, representing over $\frac{2}{3}$ of the total source foil mass. The distribution of the source foils throughout the toroidal detector is shown in Figure 2.13 and includes the two additional foils of copper and natural tellurium which were added to the structure for the purpose of validating backgrounds.

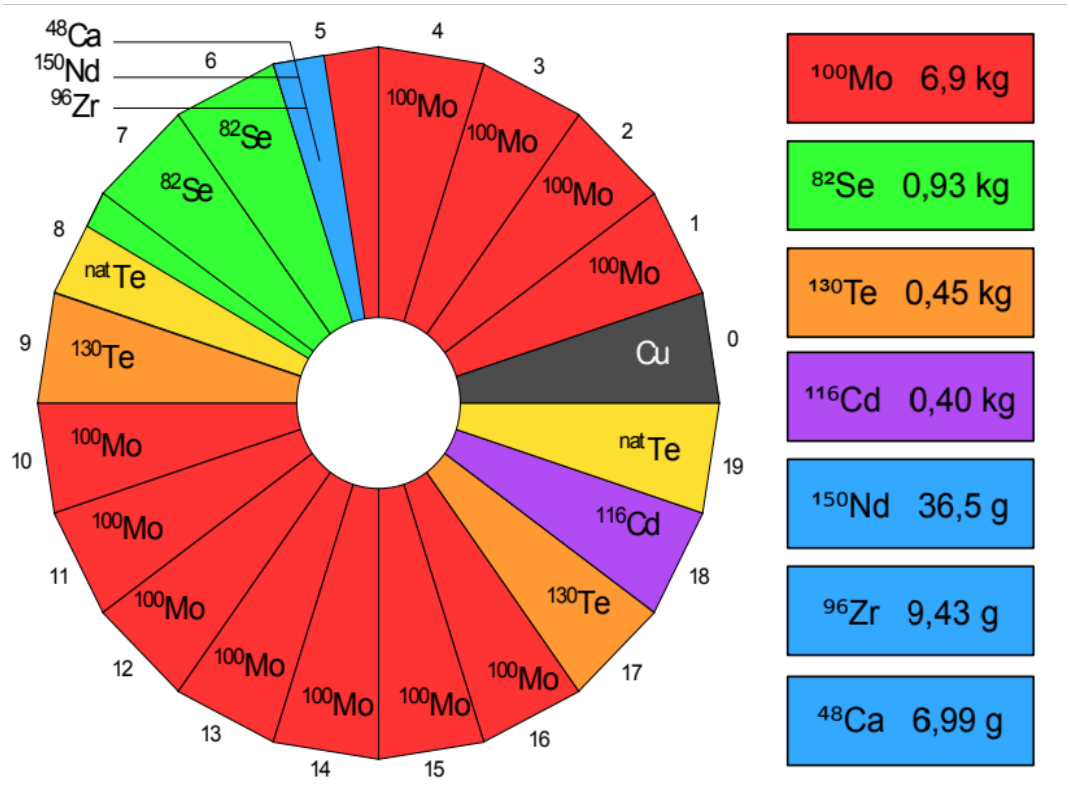

Figure 2.13: Distribution of source material across the 20 sections of the NEMO-3 detector [103].

Following data taking, no $0\nu\beta\beta$ signal was observed and the strongest $0\nu\beta\beta$ limit came from ^{100}Mo, with $\langle m_{\beta\beta}\rangle < 0.3 - 0.8$ eV, translating to a half-life of $T^{0\nu}_{1/2} > 1.1 \times 10^{24}$ yrs with a 90% confidence level, for an exposure of 34.5 Kg yrs [42]. Moreover, NEMO-3 provided world leading measurements for the $2\nu\beta\beta$ half-lives of ^{48}Ca, ^{82}Se, ^{96}Zr, ^{100}Mo, ^{116}Cd and ^{150}Nd [104, 109]. Figure 2.14 presents the tail energy of the two electron events in NEMO-3 following 34.7 Kg yrs of exposure with ^{100}Mo. The energies are given for the ^{100}Mo region of interest (2.8-3.2 MeV) around the $Q_{\beta\beta}$ value of the decay and includes both the double beta decay spectrum of ^{100}Mo as well as the various backgrounds and potential $0\nu\beta\beta$ signal.

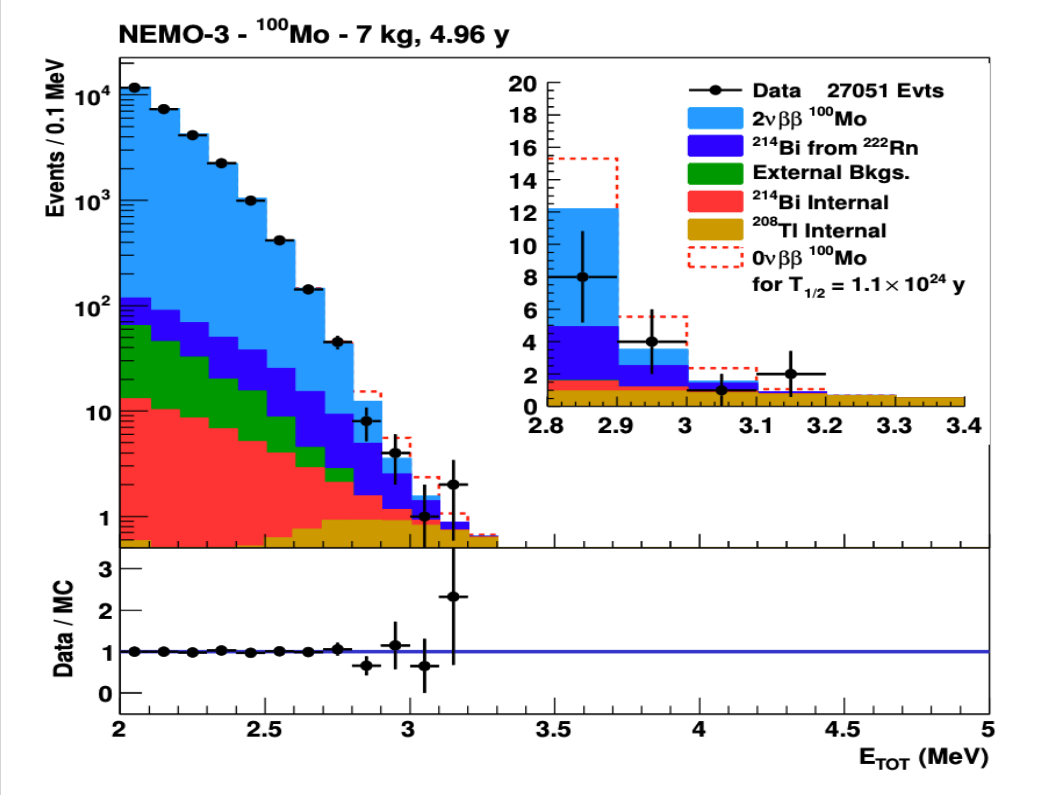

Figure 2.14: Energy distribution of ^{100}Mo double beta candidate events as well as the background contributions in the ^{100}Mo ROI [103]. The exposure for ^{100}Mo is 34.4 kg yrs.

The success of the NEMO-3 project gave rise to the SuperNEMO demonstrator and subsequent detector, which uses the same tracker-calorimeter technology as its predecessor but using a planar structure rather than the toroidal NEMO-3 detector. SuperNEMO will initially be constructed as a demonstrator module, using 7 Kg of ^{82}Se as the double beta decaying source foil with a running time of 2.5 years giving an exposure of 17.5 Kg yrs. The SuperNEMO demonstrator is expected to reach a $0\nu\beta\beta$ half-life sensitivity of $T^{0\nu}_{1/2} > 6.5 \times 10^{24}$ years with the aim of scaling to the full SuperNEMO detector, which would hold 100 Kg of isotope and reach a half-life sensitivity of the order 10^{26}.

2.7.7 Future Outlook

Before introducing the chapter on the SuperNEMO experiment, a short summary of the ongoing and future experiments presented in this section, is shown in Table 2.3. Unfortunately, of the experiments listed, the SuperNEMO demonstrator has the lowest predicted half-life sensitivity and as a result is the least likely to observe a $0\nu\beta\beta$ signal during detector operation. Although, as mentioned, when considering the fully scaled up SuperNEMO detector, the half-life sensitivity is

expected to improve significantly. The major advantage of the NEMO detectors compared to other detectors is the tracker-calorimeter structure, which can accurately reconstruct the topology of an event which will be an important tool for studying any potential $0\nu\beta\beta$ discovery.

Experiment	Mass kg	$T^{0\nu}_{1/2}$ y	$\langle m_{\beta\beta} \rangle$ meV
LEGEND-200	200	$> 10^{27}$	$<$ 34 - 78
LEGEND-1000	1000	$> 1.3 \times 10^{28}$	$<$ 9 - 21
CUORE	200	$> 2.2 \times 10^{25}$*	$<$ 90 - 305
CUPID-0	240	$> 1.1 \times 10^{27}$	$<$ 12 - 20
nEXO	5000	$> 1.35 \times 10^{28}$	$<$ 5 - 15
NEXT-100	100	$> 1 \times 10^{26}$	$<$ 60 - 160
KamLAND-Zen 800	750	$> 2.0 \times 10^{26}$	$<$ 30 - 80
KamLAND2-Zen	1000	$> 2.0 \times 10^{27}$	$<$ 12 - 53
SNO+	800	$> 2.0 \times 10^{26}$	$<$ 13 - 45
SuperNEMO Demonstrator	6	$> 6.5 \times 10^{24}$	$<$ 200 - 400
SuperNEMO	100	$> 10^{26}$	$<$ 40 - 110

Table 2.3: Summary of the ongoing and future double beta decay experiments, including the mass of the isotope, timescale of the detector operation, expected half-life sensitivity and the corresponding effective mass [110].

* indicates a current latest result

Chapter 3

The SuperNEMO Demonstrator

SuperNEMO is the successor to the NEMO-3 experiment [42] which ran during 2003-2011 collecting data for the following double beta decaying isotopes, ^{100}Mo, ^{82}Se, ^{130}Te, ^{116}Cd, ^{150}Nd, ^{96}Zr and ^{48}Ca. Unlike NEMO-3 however, SuperNEMO will initially focus solely on the isotope of ^{82}Se. SuperNEMO is located in the underground Laboratoire Souterrain de Modane (LSM), within the Frejuis road tunnel linking Modane to Bardonnecchia. The underground location is necessary to protect the detector from cosmic radiation and further protection comes in the form of an anti radon tent as well as iron and water shielding, which reduces the impact of the natural radiation found in the surrounding rock.

NEMO-3 used a cylindrical design, divided into 20 equal sections of isotopic source material whereas SuperNEMO demonstrator uses a modular structure and planar geometry, with the thin source foils located at the centre of the detector, surrounded by the tracker and calorimeters as shown in figure 3.1. The source foils consist of close to 6 kg of the double beta decaying ^{82}Se and hopes to achieve a sensitivity of $T^{0\nu}_{1/2} > 6.5 \times 10^{24}$ years, which corresponds to an effective neutrino mass $\langle m_\nu \rangle$ <(200 - 400) meV, following roughly three years of running [43]. The SuperNEMO demonstrator is the first out of 20 modules (totalling 100 Kg of isotope material) of the full SuperNEMO detector. If a signal is observed at a level of 50 meV by any double beta decay experiment, the full 20 module SuperNEMO detector would be deployed, with a sensitivity of the order 10^{26} yrs, corresponding to an effective neutrino mass of $\langle m_\nu \rangle$ <(40-100) meV. The major benefit of a full SuperNEMO detector would be the unique ability to disentangle the underlying mechanism (Section 2.3 and Figure 2.9) behind neutrinoless double beta decay via full topological reconstruction of the final states.

One of the key component of the SuperNEMO demonstrator (or full SuperNEMO detector) is the magnetic field, which is expected to be applied to the tracker volume during the demonstrator/detector operational lifetime. A magnetic field is used for the purpose of identifying the charge of a particle passing through the tracker volume which is a key part of the SuperNEMO topological reconstruction. However, prior to activating the magnetic coil, the influence of different magnetic field configurations will first be investigated in this thesis to determine the optimum magnetic field choice for data taking. The following chapter will describe the structure of the SuperNEMO detector, the current progress of the detector commissioning, the main backgrounds for the ^{82}Se $0\nu\beta\beta$ search and finally the role of the magnetic field within the detector and the configuration of the realistic field, which is the normative magnetic field that is expected during detector operation.

3.1 The SuperNEMO Demonstrator Design

The SuperNEMO demonstrator module is comprised of three main sub-modules, the source foil, the tracker volume and the segmented calorimeter as shown in figure 3.1. Unlike other double beta decay experiments, the SuperNEMO sub modules are arranged in a source-tracker-calorimeter sequence (figure 3.1), with the source foil at the centre. The structure of the demonstrator allows both the particle energy and the associated trajectory to be determined. Compared to other double beta decay experiments, the SuperNEMO demonstrator structure provides multiple advantages including,

- Record particle trajectories in three spatial dimensions.
- Being able to identify and differentiate particles such as the electron, positron, photon and alpha particle.
- Probing a variety of decay channels, primarily the two electron channel for double beta decay as well as the 1e1α channel or other background decay channels.
- Measuring the energies of single electrons as well as the opening angles of double beta candidate events.
- Can be scaled to increase the exposure of ^{82}Se.
- Any isotope which can be processed into a thin source foil can be used.

However there are also a number of disadvantages as a result of the detector design including,

- Scalability is limited by the thickness of the source foil. If the source foil is too thick it will inhibit the emission of electrons from inside the foil reducing the detection efficiency.
- Lower detection efficiency (Section 4.4.1) and energy resolution compared to germanium and bolometer experiments.

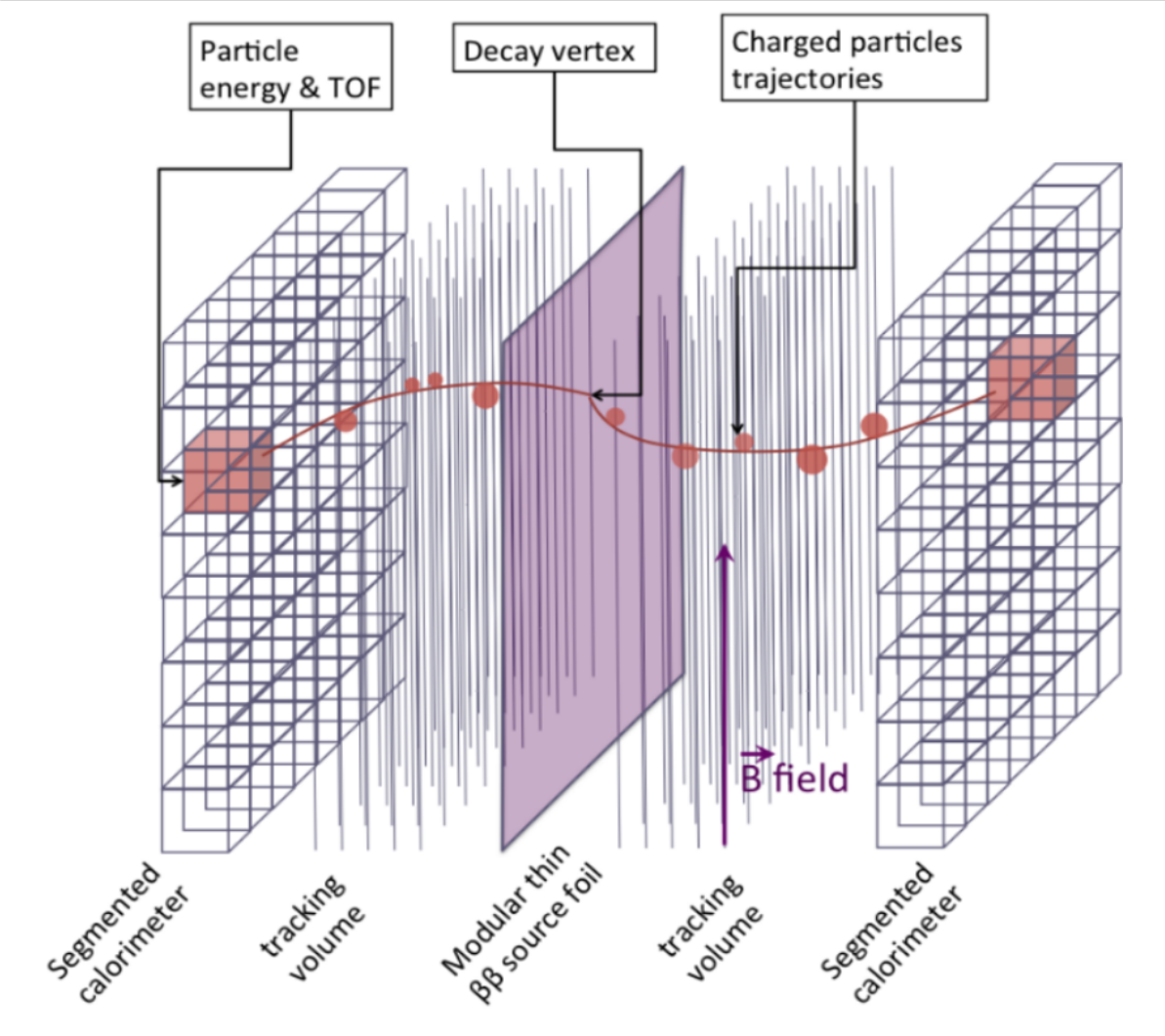

Figure 3.1: Open view of the SuperNEMO demonstrator module, illustrating the structure and the detection principal of the demonstrator module. An example double beta decay originating on the source foil is shown, including the particle tracks and calorimeter hits [126].

3.1.1 Source Foil

As mentioned, the SuperNEMO detector uses a source-tracker-calorimeter with the use of a passive source, that is, a source that is not part of detection, unlike many other double beta decay experiments (Section 2.7). The modular structure allows for both the particle energy and trajectory through the tracker volume to be reconstructed, providing the ability to identify a particles topology and kinematics. This is particularly important for identifying particular backgrounds that can mimic

double beta decays, but also provides information for single electrons which can be used to infer the underlying mechanism of the decay.

The source foil is located at the centre of the detector, surrounded by the tracker volume and finally the calorimeters. The structure of the SuperNEMO demonstrator enables the source foils to be removed and replaced by an alternative source material. The source foil is a thin, mechanically processed foil, that is enriched in ^{82}Se. The narrowness of the foil allows for improved emission of charged particles from the source foil and into the tracker chamber. In total, the source foil mass was measured to be approximately 6.11 kg of enriched ^{82}Se (97.6% enriched) [127], whilst being approximately 2.7m in length. Two methods were used to produce the source foil, the first taken from NEMO-3 and involved mixing ^{82}Se powder with PVA, which acts as a binding agent. The mixture of ^{82}Se and PVA is then poured into perforated Mylar, with a thickness of 12μm [45]. The second, novel method, pours the ^{82}Se/PVA mixture into a special mould. One drying is complete, the long foil is removed from the mould and cut into stand-alone pads, which are then inserted into a raw Mylar protector [46]. The foils are finally installed into a frame which can be placed in the centre of the demonstrator module. Of the 36 SuperNEMO demonstrator foils, 12 were produced using the NEMO-3 methodology, 18 with the novel method ([46]) and the remaining two are made out of ultrapure Cu (0.4 Kg), for the purpose of calibration and measuring external backgrounds. [45]. The surface density of the source foils is between 40 and 60 mg/cm^2 and the foils have a thickness of 0.3 mm.

^{82}Se was selected as the isotope of choice for the SuperNEMO demonstrator, amongst the isotopes used in the NEMO-3 detector because of its relatively high decay energy ($\approx$ 3MeV), high $2\nu\beta\beta$ half-life, relatively high natural abundance, and ease of enrichment (Tables 2.1 and 2.2).

3.1.2 Tracker

In order to track the trajectories of the charged particles propagating from the source foil, each side of the surrounding tracker chamber comprises of 113 columns of nine drift cells, totalling 2034 cells for both sides of the tracker. Each tracker cell is 3m long with a diameter of 4cm (figure 3.2). Each cell contains a central anode wire which is run at a high voltage, surrounded by 12 grounded field shaping wires and two ring shaped copper cathodes at on either end of the cell. Unlike NEMO-3 which had a rounded tracker chamber, the SuperNEMO tracker is planar to the source foil increasing the coverage of the segmented calorimeter surrounding the tracker.

The tracker volume is filled with gas, a mixture of He (95%), ethyl alcohol (4%) and Ar (1%). As charged particles enter the tracker chamber they ionize the gas and the time taken for the ionized electron shower to drift towards the anode infers the distance of the charged particle from the centre of the cell. Tracker cells are run in Geiger mode, so that when an ionisation occurs from a passing charged particle, the high electric potential in the tracker cell accelerates the freed electrons, further ionizing the gas, producing an avalanche. Avalanching results in the formation of a positive plasma that propagates along the length of the tracker cell until the entire cell is completely ionised

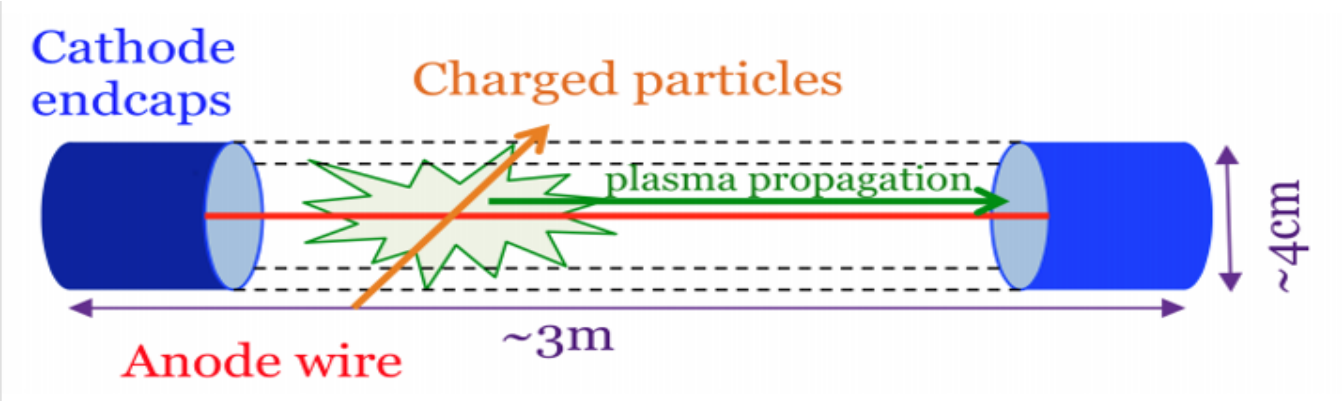

Figure 3.2: A SuperNEMO tracker cell illustrating detection principle [51].

and the plasma is able to enter the cathode ring, creating a positively charged electric field which induces a negative charge on the inside of the cathode ring. Electrons from the ground neutralise the positively charged field, resulting in a potential drop between the ground and cathode, which is measured as a timed signal by the electronics. Finally, the two cathode end caps measure how far along the the tracker cell the charged particle was when generating the electronic shower, which is key for reconstructing the Z-coordinate of the decay electron.

The z-coordinate of a charged particle is determined by the equation [52],

$$z = \frac{L_{eff}}{2}\frac{t_{c2}-t_{c1}}{t_{c2}+t_{c1}}\left[1 - K\frac{L_{eff}}{2}\left(1 - \left|\frac{t_{c2}-t_{c1}}{t_{c2}+t_{c1}}\right|\right)\right] \tag{3.1}$$

where L_{eff} is the effective length of the cell (the distance from the edge of one cathode to the next) and K is a constant equal to 0.408×10^{-4}. t_{c1} and t_{c2} are the timings of the first and second cathode peaks from the plasma propagation. The transverse hit resolution is 0.7 mm and the longitudinal hit resolution 1.3 cm [53]. The signals from the anode and cathode are used to extract multiple variables which can be used to reconstruct the position of the charged particle as it propagates through the tracker.

3.1.3 Calorimeter

The final component of the SuperNEMO demonstrator module structure is the segmented calorimeter wall, which surrounds each side of the tracker. There are a total of six calorimeter walls for SuperNEMO, two of each of the following; Main Wall, X Wall and the Gamma Veto or Veto Wall. Each wall is comprised of a different number of optical modules (OM) with the corresponding PMT size,

- Main wall: 220 8” calorimeters and 40 5” calorimeters.

- X wall: 64 5” calorimeters.
- Veto wall: 32 5” calorimeters.

totalling 712 OMs. Figure 3.5 shows one of the two Main Walls installed at the LSM. Each OM comprises of a plastic scintillator, shown in figure 3.3a and a Hammatsu PMT. The plastic scintillators are made of polystyrene (PST) and is doped with PTP (para-terphenyl) and POPOP (1.4-bis(5-phenyloxazol-2-yl) benzene), which act as a primary scintillating agent and wavelength shifter respectively [55]. Plastic scintillators used for the SuperNEMO demonstrator are manufactured by NUVIA. Alongside the NUVIA PST scintillators, a small number of polyvyniltoluene (PVT) ELJEN scintillators are used. When an incident particle strikes a plastic scintillator block, it loses energy from multiple scatterings, resulting in a number of photons being emitted proportional to the incident particle energy. Scintillator blocks are wrapped in both aluminised mylar to increase light collection and protect against UV radiation from the tracker or adjacent OMs and teflon to increase photon collection efficiency.

5” PMTs (Hamamatsu, R6594 [55]) were recycled from NEMO-3, however new 8” PMTs (Hamamatsu, R5912-MOD [55]) were acquired directly from Hamamatsu. The 8” calorimeters provide improved energy resolution and thus are mostly confined to the Main Wall. By carving the plastic scintillators, the PMT bulbs can be coupled to them using radiopure gel, combined to form the OM shown in figure 3.3b. Directly coupling the PMT and scintillator allows for the light guides to be removed (as used in NEMO-3), improving the energy resolution of the OM.

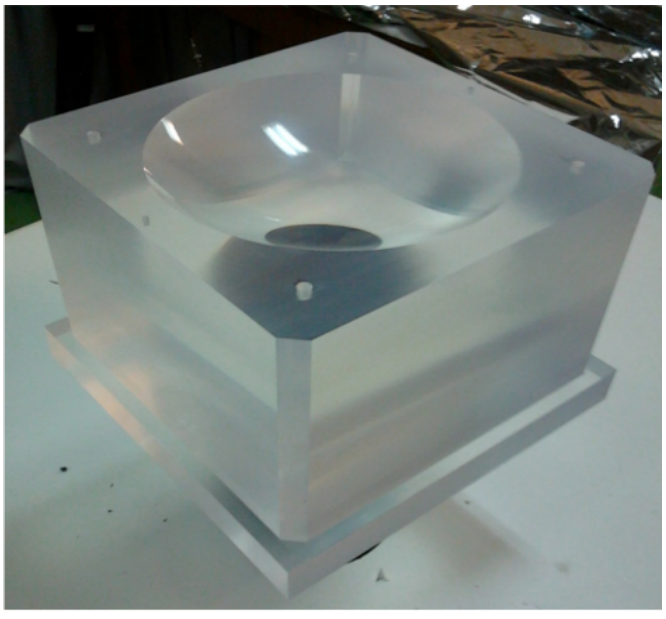

(a) Carved plastic scintillator produced from doped PST. The shape of the scintillator enables the PMT glass bulb to be directly coupled to the surface of the scintillator.

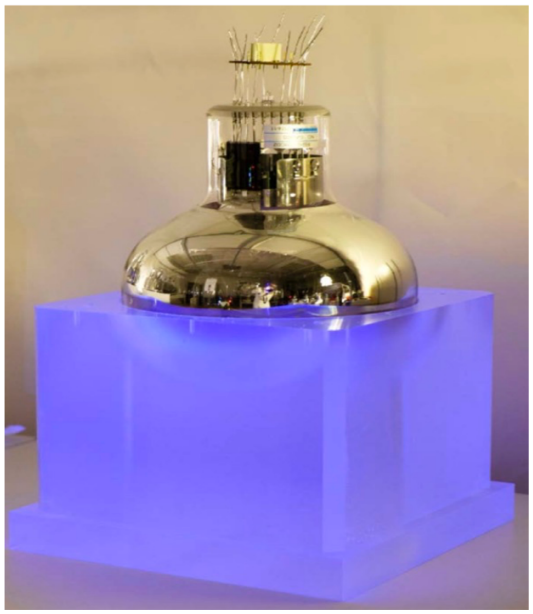

(b) SuperNEMO optical module, including a PMT coupled to the plastic scintillator in Figure 3.3a.

The 8" PMTs coupled directly to the plastic scintillators results in an increased energy resolution of roughly 7.3% FWHM at 1 MeV, compared to NEMO-3 which was 14-17% FWHM at 1 MeV. The energy resolution of the 8" PMTs as a function of electron energy is shown in Figure 3.4. The timing resolution at the same energy is 400 ± 90 ps [56].

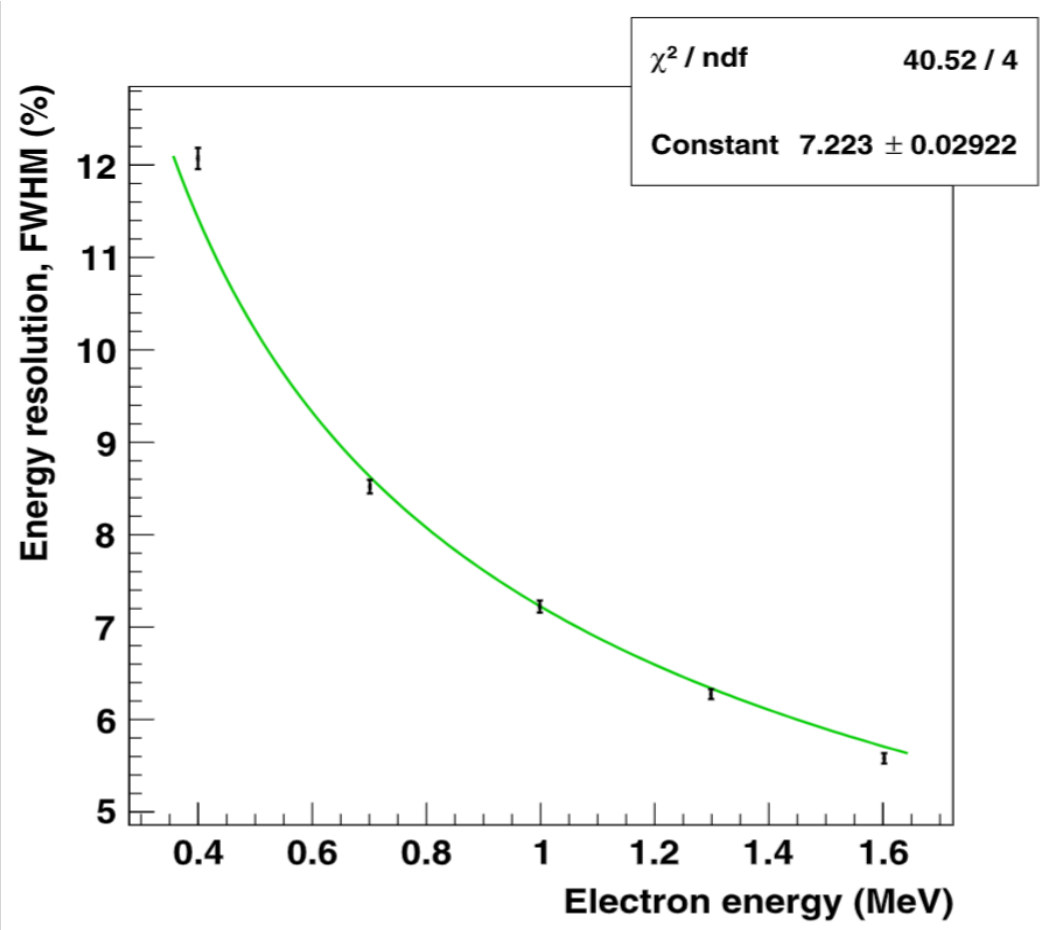

Figure 3.4: Energy resolution (FWHM %) as a function of the electron energy. Results were obtained using a ^{90}Sr based electron beam [55].

Figure 3.5: One of the Main Walls assembled at the LSM. Each Main Wall contains 220 8" calorimeters and 40 5" calorimeters [56].

3.1.4 Calibration

Multiple calibration methods will be used to determine the energy and time responses of the detector to known sources. To perform energy calibration for SuperNEMO, multiple ^{207}Bi sources will be deployed within the detector to obtain an absolute energy measurement. ^{207}Bi decays via electron capture, resulting in a number of conversion electrons emitted at energies of 482, 976 and 1682 keV, shown by the electron calibration lines in figure 3.6.

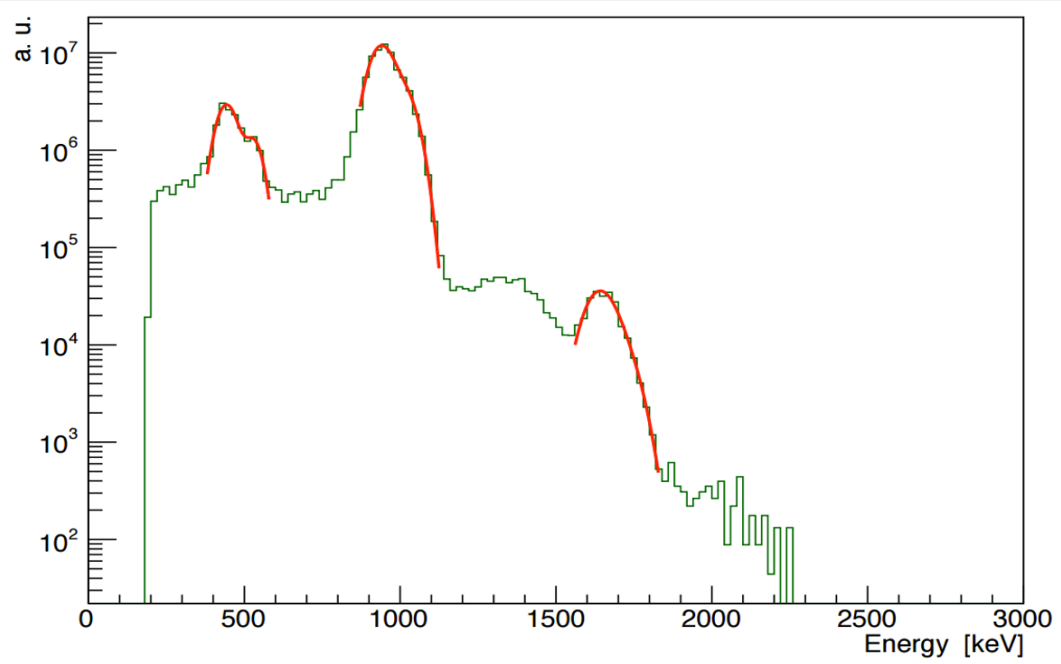

Figure 3.6: Reconstructed ^{207}Bi energy spectrum from a simulated calibration run. The three peaks correspond to the 482, 976 and 1682 keV energy lines [116].

For each source, a droplet of ^{207}Bi in between two layers of mylar will be encapsulated by a radiopure copper frame, following which they will be inserted into the gaps between the source foils via an automatic source deployment system. Calibration is expected to be performed regularly during detector operation to ensure energy measurements are accurate. The ^{207}Bi internal conversions will be reconstructed from the location of the copper frames to the calorimeters for the purpose of measuring the reconstructed energies and comparing to the true ^{207}Bi internal conversion lines. For neutrinoless double beta decay in the ^{82}Se region of interest (2.8-3.2 MeV), the greatest internal conversion energy line is 1682 keV, however this occurs with a low branching ratio making it difficult to use for calibration. However, until the tracker has been fully commissioned, the high voltage gain of the PMTs is equalized using the Compton edge of the ^{208}Tl high energy 2.61 MeV photon. Doing so reduced the spread of the optical modules gain to less than 10% although this is expected to improve once the ^{207}Bi energy calibration method is online [43].

Alongside the ^{207}Bi deployment close to the source foil, a Light Injection System (LIS - Figure 3.7) will be utilised to perform both time calibration and measure gain for the optical modules. The light injection system uses pulses of ultraviolet light from light emitting diodes, through optical fibres to illuminate OMs and measure their gain. The length of all fibres will be maintained at 20m to avoid any systematic time differences. ^{241}Am is used as a source with a reference OM to monitor and maintain the light level. In total, the LIS will allow any variations in gain from voltage fluctuations be tracked and corrected with a precision of 1% alongside the time calibration.

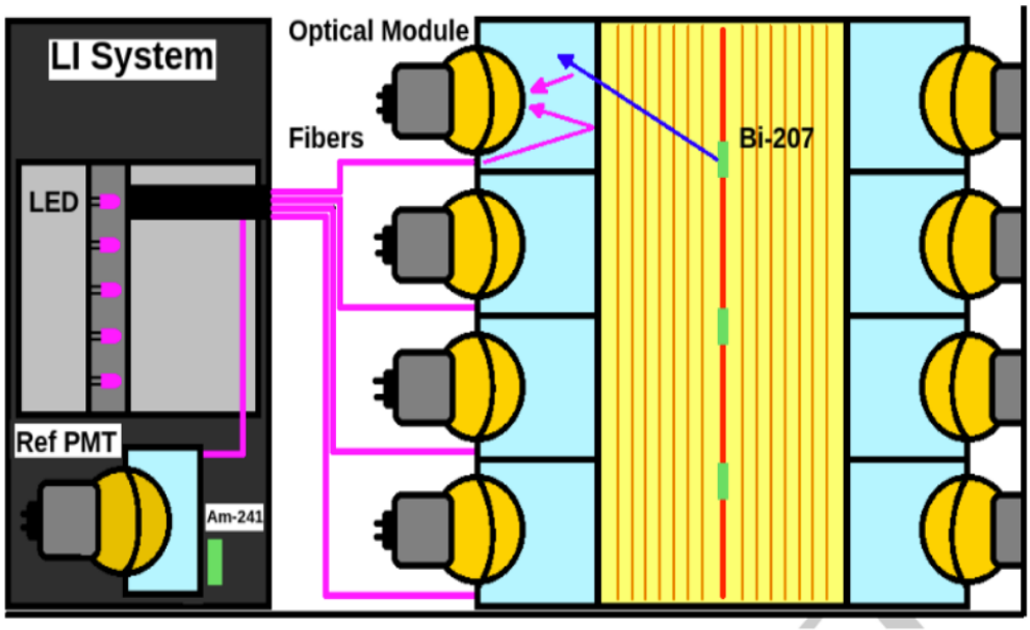

Figure 3.7: Illustration of the light injection monitoring system [117].

Additional time calibration will be performed using ^{60}Co, which produces two photons, the first being of energy 1.17 MeV and the second, 1.33 MeV. The two photons are emitted almost simultaneously (Δt = 0.41ps) from the source at a separation much lower than the time resolution of the PMTs. By placing the ^{60}Co source behind the main wall in one of nine different positions, at known distances from two PMTs, the energies and time separation of the two photons can be measured to determine the offset of the PMTs. Preliminary data has been taken using ^{60}Co in order to determine the time resolution. Initial results have shown the time resolution to be be <600 ps for photons with energy close to 1 MeV, which is expected to improve once the tracker is fully commissioned and ^{207}Bi can be used.

3.2 Commissioning Progress

Currently the ^{82}Se source foils have been installed, the calorimeters are active and being used to validate the calibration systems, such as LIS discussed in Section 3.1.4. Only a fraction of the tracker cells (252/2034) are currently powered on and collecting data, with the remainder of the tracker cells set to be activated by 2022. The magnetic coil has been installed, following completion of the tracker sealing. Commissioning has also been complete for the working gas mixture, the High Voltage (HV) board and the Data Acquisition (DAQ) readout chain.

Physics data taking has commenced, without passive shielding to inform the external background model. The passive shielding has been ordered and is expected to be installed over the following year. Data taking in the final configuration, with the shielding installed is proposed to begin in the summer and latter half of 2022. As of September 2021, the first tracks and associated calorimeter hits in the demonstrator module have been measured. The first double beta decay candidate event from the ^{82}Se foil has been successfully observed and reconstructed, including both tracker and calorimeter data. Figure 3.8 illustrates the double beta candidate event in relation to the structure of the SuperNEMO demonstrator module,

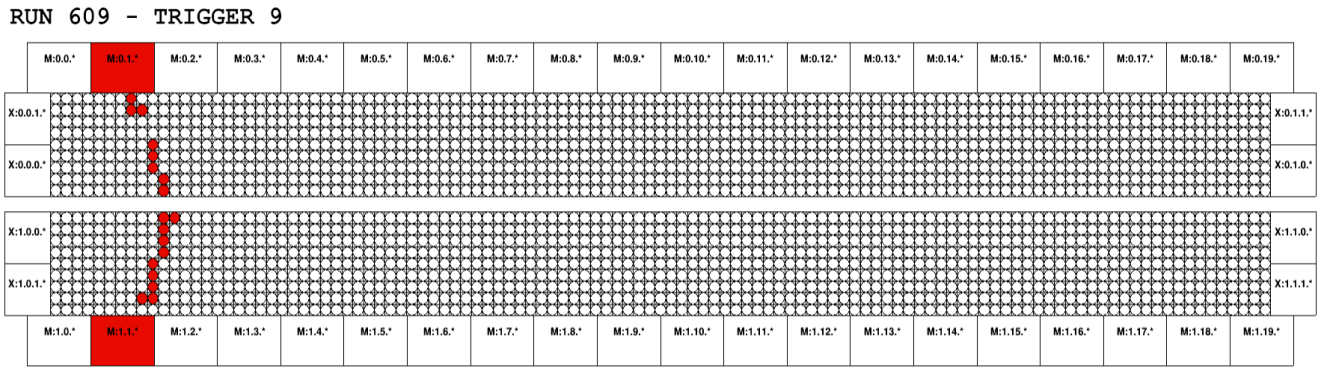

Figure 3.8: Event display of the first successfully reconstructed double beta candidate event using the SuperNEMO demonstrator module. The event display presents a top down image of the demonstrator module, with the calorimeters labelled with respect to their position in the detector. Main Wall calorimeters are labelled M:X.Y., where M denotes the Main Wall, X denotes the side of the detector and Y the column. Calorimeters on the X Wall are labelled X:A.B.C, where X represents the X Wall and A,B and C denote the top and bottom ends, the left and right sides and the column respectively (from a top down perspective).

3.3 Backgrounds Sources

The main SuperNEMO background contributions come from natural radioactivity found within the rocks surrounding the LSM, the laboratory itself, detector components and the source foil. The most significant backgrounds come from the decay chains of the long lived radioisotopes ^{232}Th and ^{238}U as shown in figures 3.9 and 3.10 respectively. ^{232}Th and ^{238}U are two naturally occurring backgrounds, found in small amounts within all materials. The decay progeny of ^{232}Th and ^{238}U are high energy electron and photon emitters, which can mimic double beta decays (Section 6.1) in the ^{82}Se region of interest (2.8 - 3.2 MeV).

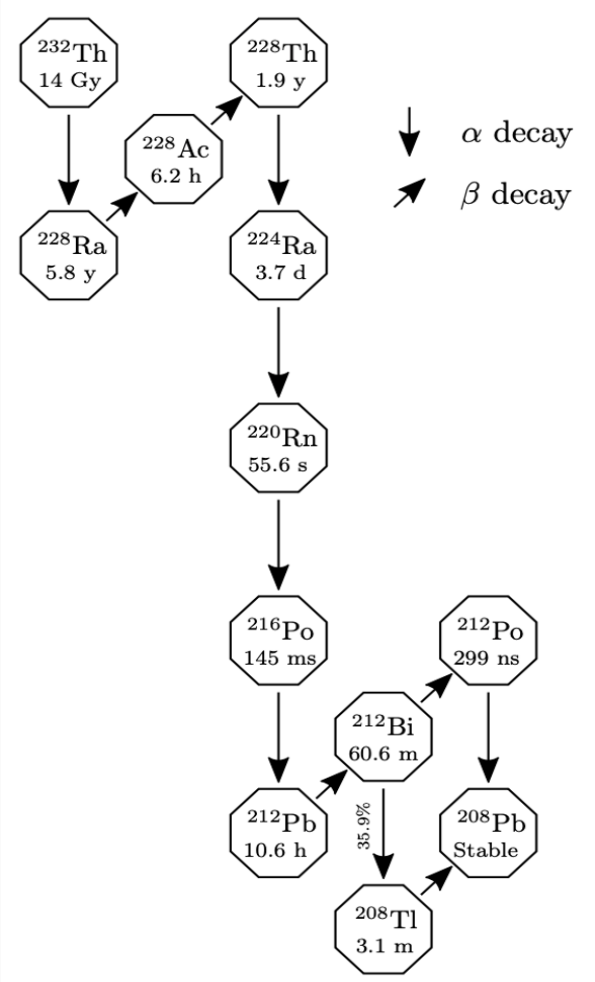

Figure 3.9: ^{232}Th decay chain, known as the thorium series. Alpha decays are represented as downward arrows, illustrating a change in the atomic mass of the isotope. Beta decays are illustrated by the slanted arrow. When an isotope is capable of decaying into multiple modes, the branching ratios for the alpha decay mode is given [7].

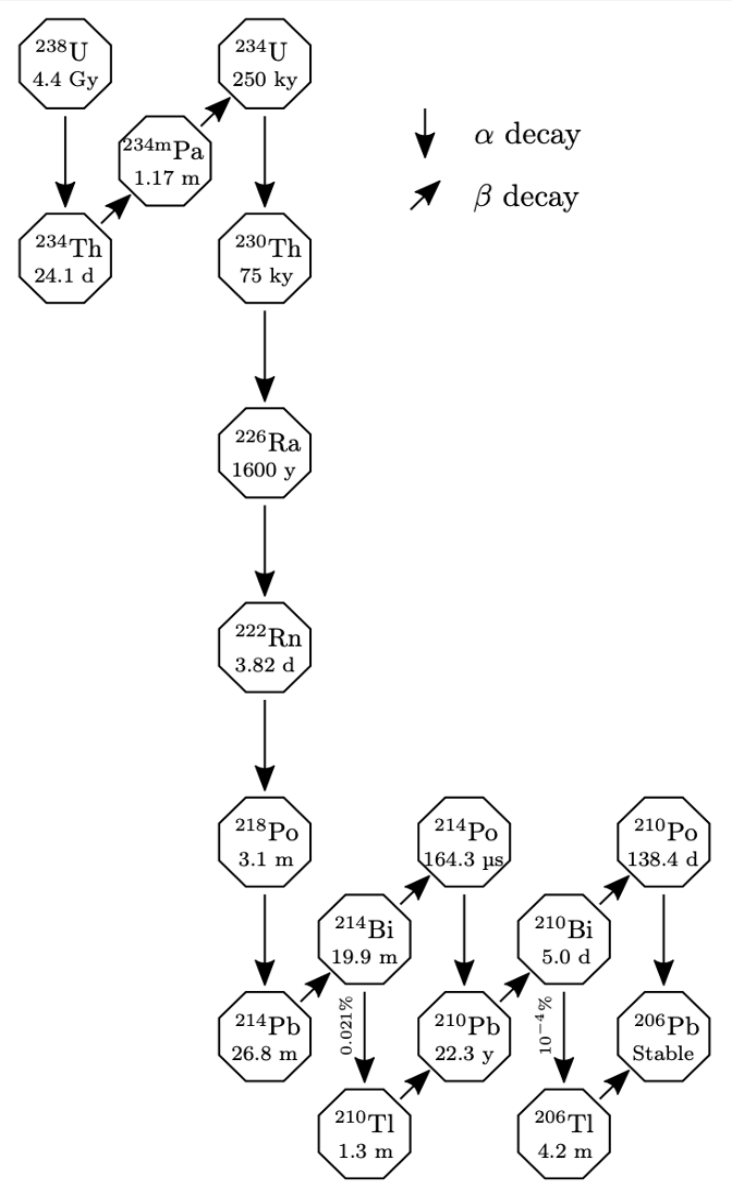

Figure 3.10: ^{238}U decay chain, knows as the radium series. The same notation is used between this figure and Figure 3.9 [7].

3.3.1 Background Locations

As mentioned in Section 2.6, the two main SuperNEMO backgrounds are ^{208}Tl and ^{214}Bi, which have decay energies of 4.99 and 3.27 MeV respectively. The backgrounds can be discriminated based on their locations within the detector, although backgrounds within the surrounding rocks and outside of the detector are not expected to be problematic on account of the detector shielding and the high ^{82}Se $Q^{\beta\beta}$. External neutron backgrounds may also contribute to the neutrinoless double beta decay sensitivity, however they are not considered in this work. Details of the neutron backgrounds and shielding for SuperNEMO can be found in [111].

The three main background locations considered in this study are:

- Internal - for backgrounds located within the source foil.
- Radon - for backgrounds that originate from radon contamination within the tracker volume.
- External - for non-radon backgrounds originating outside of the source foil but within the detector components.

To minimize the intrinsic background contamination, all materials were screened using a HPGe gamma spectroscopy detector, which has a sensitivity of 0.1-10 mB/kg for ^{232}Th, ^{238}U and ^{40}K [112]. An additional BiPo detector, which has its name derived from the decay of Bismuth to Polonium, was developed in [114], to measure the ^{208}Tl and ^{214}Bi contamination in thin materials, including the SuperNEMO source foils. The sensitivity of the BiPo detector for measuring the contamination of the SuperNEMO source foils was found to be <2 μBq/Kg for ^{208}Tl and <140 μBq/Kg for ^{214}Bi (90% C.L.) after 6 months of measurements. The SuperNEMO target activities for internal ^{208}Tl and ^{214}Bi are 2 μBq/kg and 10 μBq/kg respectively and the measured values are shown in Table 6.1 (Chapter 6).

For radon in the tracker volume, the target activity is <0.15 mBq/m^3. Additional methods are used alongside material screening to ensure the radon background is suppressed including, constant monitoring of the radon background levels and purification of the tracker gas. Radon can continuously emanate into the tracker volume so the gas inside the tracker is flushed to maintain the low background level. The most significant reduction in radon levels is achieved by flushing out the contaminated tracker gas with clean gas at a controlled rate. At a certain point, increasing the rate at which gas flows through the tracker becomes detrimental to the performance of the tracking detector and so a compromise between the performance and radon levels is met at a maximal flow rate of 2m^3/h [113].

The current BiPo detector BiPo-3, derived from the BiPo prototypes [115], works by detecting the emission of an electron followed by a delayed alpha (1e1α channel), for the BiPo decays of ^{212}Bi and ^{214}Bi. ^{212}Bi is used to determine the ^{208}Tl contamination as it is the predecessor to ^{208}Tl and decays into ^{208}Tl 36% of the time (figure 3.11).

The activity of ^{208}Tl is then calculated by measuring the alpha emission ($T^{\alpha}_{1/2} \approx 300$ ns) of

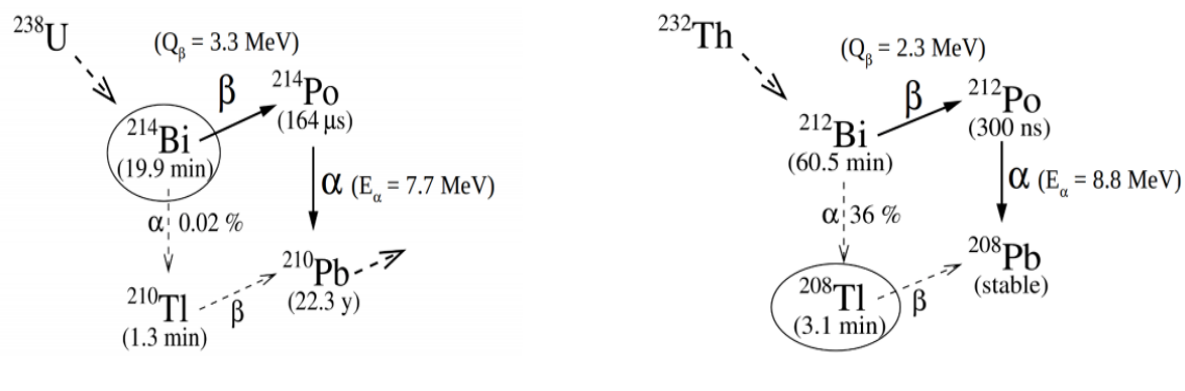

Figure 3.11: The two cascades, ^{214}Bi $\rightarrow$ ^{214}Po and ^{212}Bi $\rightarrow$ ^{212}Po, used to determine the contamination of ^{214}Bi and ^{208}Tl respectively [114].

^{212}Po which is produced by the remaining 64% of ^{212}Bi decays. ^{214}Bi decays to ^{214}Po, which is also an alpha emitter, but with $T^{\alpha}_{1/2} \approx 164$ μs. To measure the contamination of the source foils, the foils are placed between two thin ultra radiopure plastic scintillators as shown in figure3.12, which then detects the beta decays of ^{212}Bi and ^{214}Bi as an energy deposition in one scintillator with no coincident signal in the second scintillator. The alphas are then measured as a delayed signal in the second scintillator without a coincident deposition in the first scintillator. The events are labelled as back-to-back events since the beta and alpha particles are detected in the different scintillators on the opposite side of the foil. ^{212}Bi and ^{214}Bi are differentiated based on the alpha timing and the energy of the alpha is used to determine if the decay originates from the surface or bulk of the source foil.

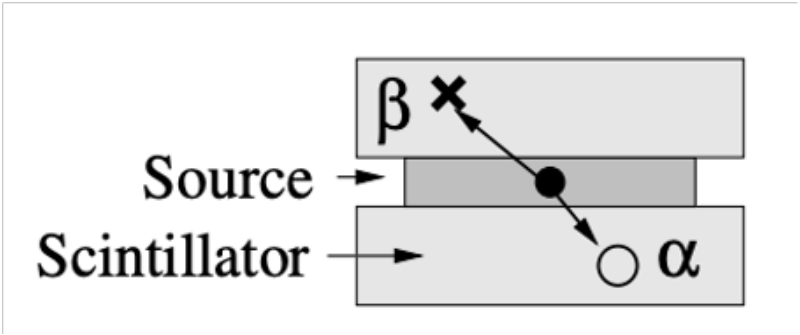

Figure 3.12: Schematic view of the BiPo measurement technique. The dot indicates the location of a decay inside the source foil, with the emission of a prompt β and delayed α. The position of the decay can be inferred from the alpha energy as alphas from the bulk lose more energy compared to those emitted from the surface of the foil [114].

3.3.2 Magnetic Coil and Shielding

The magnetic field for the SuperNEMO detector will be generated by a copper magnetic solenoidal coil, recycled from old NEMO-3 copper rods. The coil is expected to produce a magnetic field of 25 Gauss, normal to the ground and will be built to surround the detector as shown in Figure 3.13, ensuring the magnetic flux is contained to the tracker volume. Electrons from ^{82}Se double beta decay are of relatively low energy and so do not require high magnetic field strengths to significantly curve their tracks

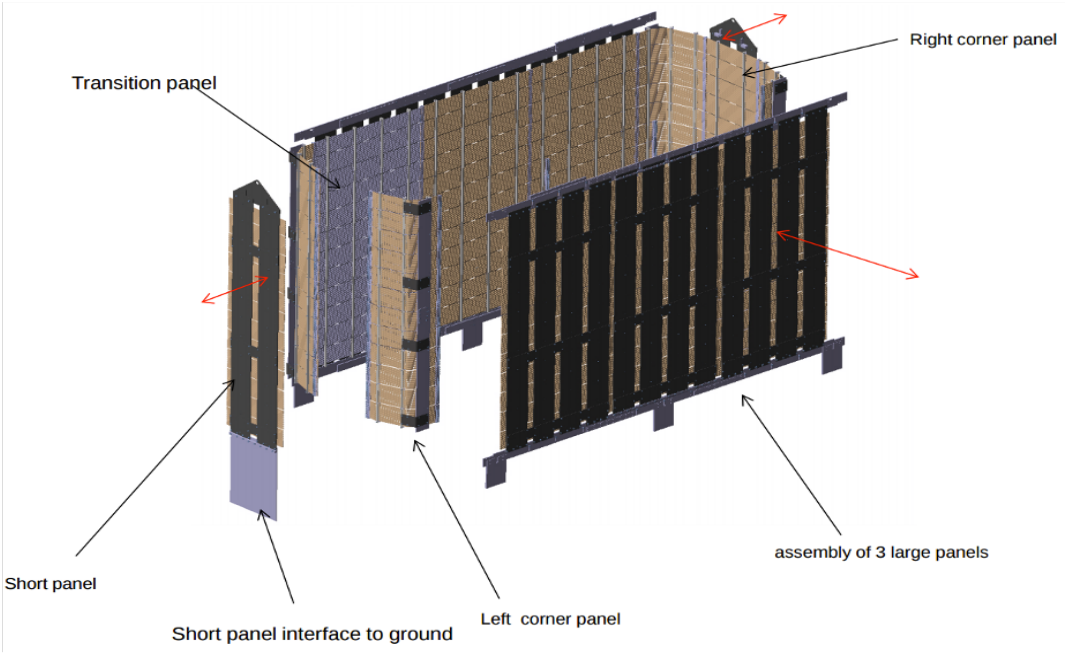

Figure 3.13: Open view of the magnetic coil illustrating the key components of the structure [118].

The dimensions of the magnetic coil are 6097 × 2198 × 3483 mm and it weighs a total of 9 tonnes. It is imperative that the magnetic field is contained within the tracker volume and does not permeate into the calorimeter walls as the presence of magnetic flux inside the glass of a PMT significantly reduces the performance of the PMT even at very low field strengths as shown in Figure 3.14,

Unlike NEMO-3, SuperNEMO does not use a light guide with the OMs as the PMTs are directly coupled to the plastic scintillators as shown in figure 3.3b. As a result, the PMTs are exposed to the tracker volume and the magnetic flux. To prevent the PMT performance being reduced by the magnetic field, iron shields will be used to protect the PMTs and remove any magnetic field from within their volume.

The working mechanism of a PMT is shown in Figure 3.15 and involves incoming photons generating photoelectrons that are focused onto the the first dynode. Secondary electron emission

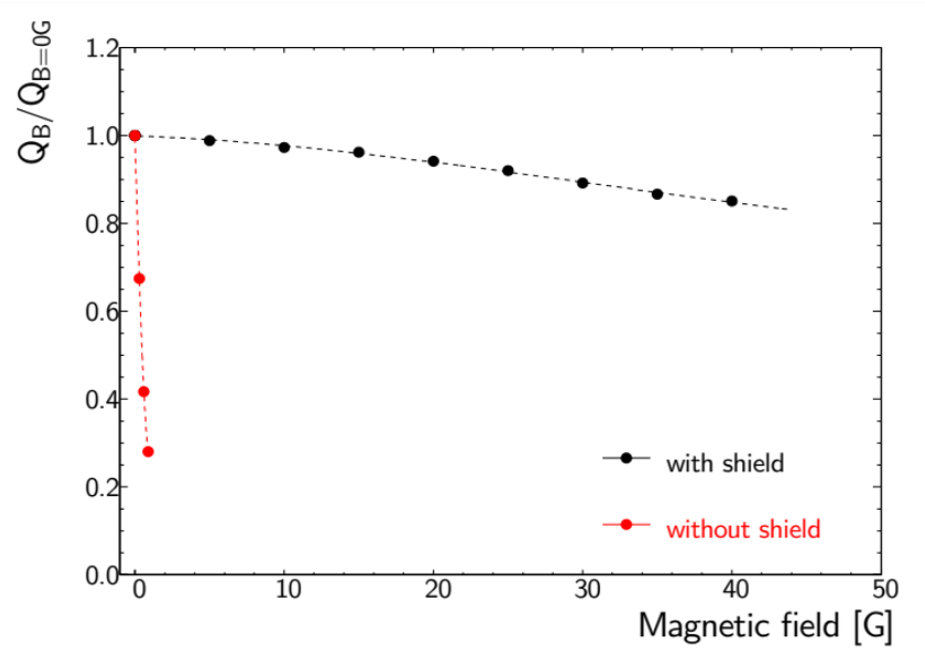

Figure 3.14: Photoelectron collection efficiency as a function of magnetic field strength. Data was collected using SuperNEMO PMTs [119].

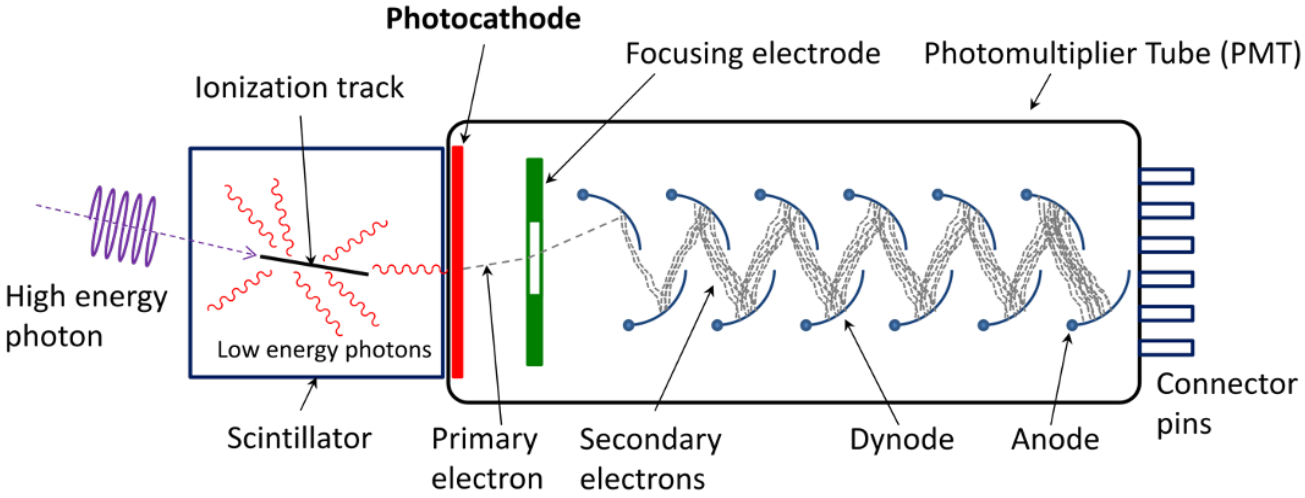

Figure 3.15: Schematic view of the working principle of a PMT coupled to a scintillator. The scintillation photons are focused within the PMT and read as an electric signal at the anode [120].

from the dynodes carries a charge which is collected by the anode. The collected current provides

an output signal to indicate a hit to the calorimeter.

With the addition of even a small a magnetic field, the low energy photoelectron trajectories are altered, reducing the collection efficiency of the dynodes. Even at a field strength of 1 Gauss the reduction in collection efficiency results in a complete loss of signal as is seen in Figure 3.14. Furthermore, there is the possibility of PMT components, in particular, the dynode substrate and the electrode, being permanently magnetised following exposure to weak magnetic fields for long periods of time. The residual magnetisation can result in a change to the gain of a PMT, ultimately reducing performance. Over the length of time taken for detector operation any changes in the gain of PMTs should be monitored to ensure the precision of energy measurements are maintained. As mentioned in Section 3.3.2, magnetic shielding will be installed and will protect the PMTs from being exposed to the magnetic flux. The reduction in magnetic field with and without the shielding was investigated and is presented in Section 3.4.2.

3.4 Motivation for Magnetic Field Studies

The magnetic field allows electrons and positrons to be differentiated by the directionality of their associated track curvatures. It provides a useful tool for removing significant backgrounds, in particular photons with energy greater or equal to 1.02 MeV, which are capable of pair producing an electron positron pair. Other sources of positrons include rare positron emitting decays however they are seldom observed and not expected to be problematic. Moreover, the magnetic field helps to identify crossing electrons as they propagate from one side of the detector to the other, producing two non coincident electron tracks, with only one track originating from the source foil. Visualisations of these two backgrounds are shown in Figures 4.4 and 4.5 (Chapter 4) respectively.

External gamma ray background flux is significant, so being able to identify positrons efficiently is important. The magnetic field provides the best option for identifying positrons however it may be possible to use the detector without a magnetic field if it improves the half-life sensitivity of the detector. Although removing the magnetic field will increase the rate of backgrounds from positrons, an increase in the signal detection efficiency may offset the increased background count, resulting in a net gain in sensitivity. It may be possible to remove the positron backgrounds without the use of a magnetic field with a simultaneous improvement in signal detection efficiency.

Three magnetic field configurations were investigated, including the uniform field, no field and the 'realistic' field. The uniform field is defined as having a nominal 25 Gauss field, with uniform strength and shape throughout every part of the detector. No field is characterised by having no magnetic field (0 Gauss) throughout the detector and corresponds to having the magnetic field turned off. The 'realistic' field is a mathematically computed field, representing the shape and strength of the field taking into account the design of the detector and material used, with a nominal 25 Gauss applied via a magnetic coil [121].

The performance of the three magnetic field configurations is studied using their respective

sensitivities to the $0\nu\beta\beta$ decay estimated using a Minimum Detectable Activity (MDA) method as the Figure Of Merit (FOM), described in Section 4.5.1. The results reported in this thesis, will be used to inform when or if the magnetic field will be switched on for the SuperNEMO demonstrator module.

3.4.1 The Realistic Field

Magnetic shields are required for the SuperNEMO demonstrator optical modules as a consequence of the detector geometry exposing the PMTs to magnetic flux. The removal of a light-guide coupled to the surface of the PMTs exposes the vacuum tube of the PMT to the magnetic field inside the tracker volume. As shown in figure 3.14 the presence of a magnetic field is extremely detrimental to the performance of a PMT and so the shielding should ensure that all magnetic flux is removed from the volume of the PMTs.

As a result of using the magnetic shields however, the shape and strength of the field is altered so that is it no longer uniform in shape or strength. As mentioned earlier, the expected magnetic field is labelled the realistic field and represents a 25G magnetic field transformed by the addition of the magnetic shielding. The shape and strength of the realistic field is shown in the Figure 3.16 below,

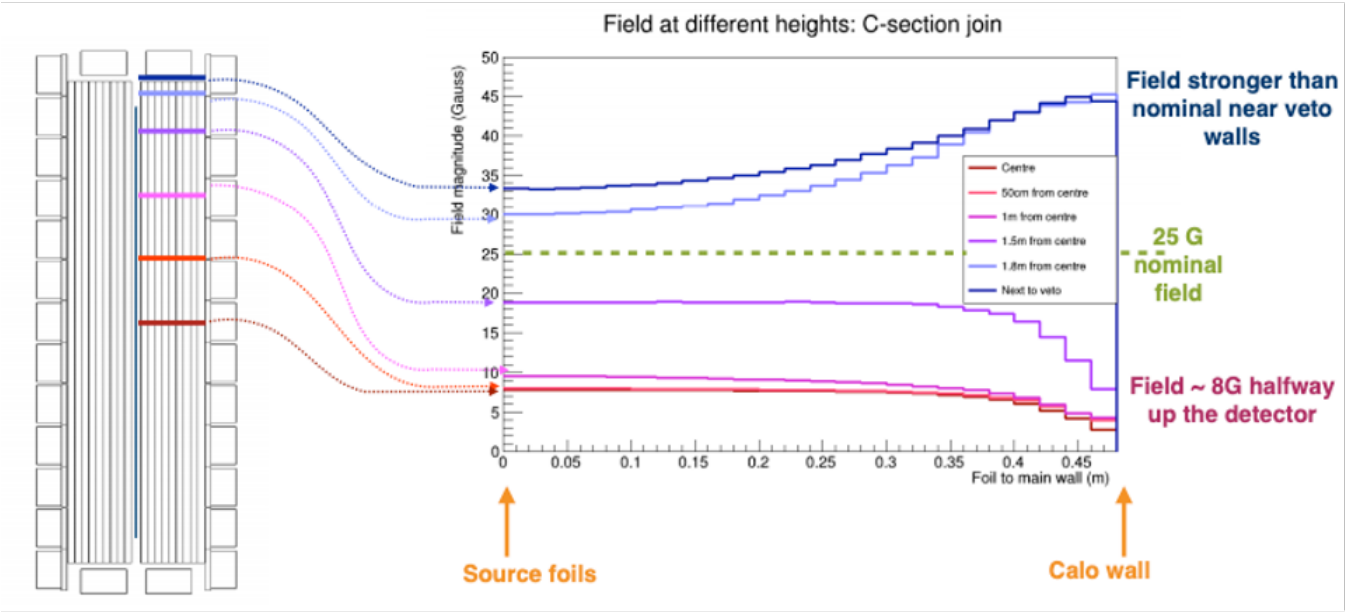

Figure 3.16: Visualisation of the realistic field including the active field strength at different locations within the detector. The strength of the magnetic field is dependant upon the direction in both the X-Y and X-Z planes[122]. Figure 3.16 was calculated using a finite element analysis with the FlexPDE simulation package discussed in [121].

Figure 3.16 presents the magnetic field strength ('Field magnitude (Gauss)') as a function of the distance from the foil ('Foil to main wall (m)'), including a cross section of the detector through the X-Z plane. The colours indicate the position from the centre of the detector in the Z axis (parallel to the foil) and runs from the centre of the foil to the Veto Walls (Figure 3.1). From Figure 3.16, the magnetic field strength is higher, the further away as you move away from the centre of the detector and is highest closest to the Veto Wall. Concurrently, moving from the source to the Main Wall ('Calo wall') reduces the magnetic field between the centre and 1.5m from the centre. Above 1.5m from the centre, there is an increase in the magnetic field closer to the 'Calo wall'.

The main aim of the magnetic field analysis described in this thesis is to compare the performance of the three field configurations, the uniform, realistic and no field, to determine which of the three fields is most advantageous for use during and throughout the detectors operational lifetime. Although the uniform field does not correctly depict the non-uniformity of the magnetic field during operation, it provides a nominal comparison for the other fields. Investigating the no field scenario allows for the performance of the detector without an applied magnetic field can be determined. If no field displays an increased performance over the realistic and uniform fields it may be advantageous to run the detector without a magnetic field and to remove positron backgrounds through other avenues. Additionally, there is the option to run the detector without the magnetic field for a short period of time and to determine at what point, if at all, to turn on the magnetic field during experimentation. Once the magnetic field is turned on, it is impossible to reverse the effects of the applied field on the detector components even if the field is later turned off and so it is important to identify what approach to take and if or when the magnetic field should be applied.

3.4.2 Magnetic Shield Testing

Prior to installation, individual magnetic shields, previously used in NEMO-3, were tested to ascertain whether they were still able to significantly reduce magnetic flux from within the volume inside. To measure the efficiency at which the shields remove magnetic flux from within their own volume, the magnetic field with and without shielding was measured. A copper solenoid was connected to a controlled current source to generate a magnetic field. The solenoid was coiled around an impermeable container to retain the field inside of the container. A simple search coil magnetometer, which utilises a magnetic core surrounded by copper coils to measure a current corresponding to the magnetisation of the core, was used to measure the field strength within the container. The field was calibrated to 25G following each measurement and the magnetometer measured the field strength, with and without shielding to determine the influence of the shield on the magnetic field inside of it.

Over 250 shields were tested, both for 8" and 5" PMTs, with the majority expelling over 95% ($\mathbf{B}$ <1.25G) of the magnetic field within the shielded volume. Once tested the shields were packed and shipped to the LSM to be installed as part of the detector.

Figure 3.17: Image of the copper solenoid and impermeable container used to measure the ability of the shields to remove the magnetic field within their volume [119].

Chapter 4

Analysis Techniques

The analysis techniques chapter introduces the software package Falaise, which is used in order to generate Monte Carlo simulated decays inside the SuperNEMO demonstrator module. The different components of the software package will be explained and their role within the simulation process will be presented. Following this, the reconstructed topologies of particles will be established, for the electron, positron, alpha and gamma particles, taking advantage of the modular structure of the SuperNEMO demonstrator, which allows the the trajectory of a particle to be measured and the nature of the particle to be determined, as shown in chapter 3. Finally, the tools required for the analysis of simulated data, including the internal and external hypothesis, the signal detection efficiency and background survival efficiency, the number of expected events, the figure of merit (FOM) and half-life calculations will be presented and used in the proceeding chapters to compare the three proposed magnetic field configurations.

4.1 Falaise

Falaise provides the overarching software environment and is used as the primary tool for the simulation, processing and analysis of data for the SuperNEMO collaboration. Falaise uses the DECAY0 event generator in combination with GEANT4 and the C++ Bayeux library to generate and propagate particles throughout the depiction of the detector geometry.

Falaise is comprised of four principal components:

- Flsimulate

  The primary tool for simulating data

- Flreconstruct

  Pipeline structure used to process the output from flsimulate and produce reconstructed data

- Flvisualize

  Event viewer for the visualization of the detector geometry, simulated and reconstructed data

- LibFalaise

  The core libraries

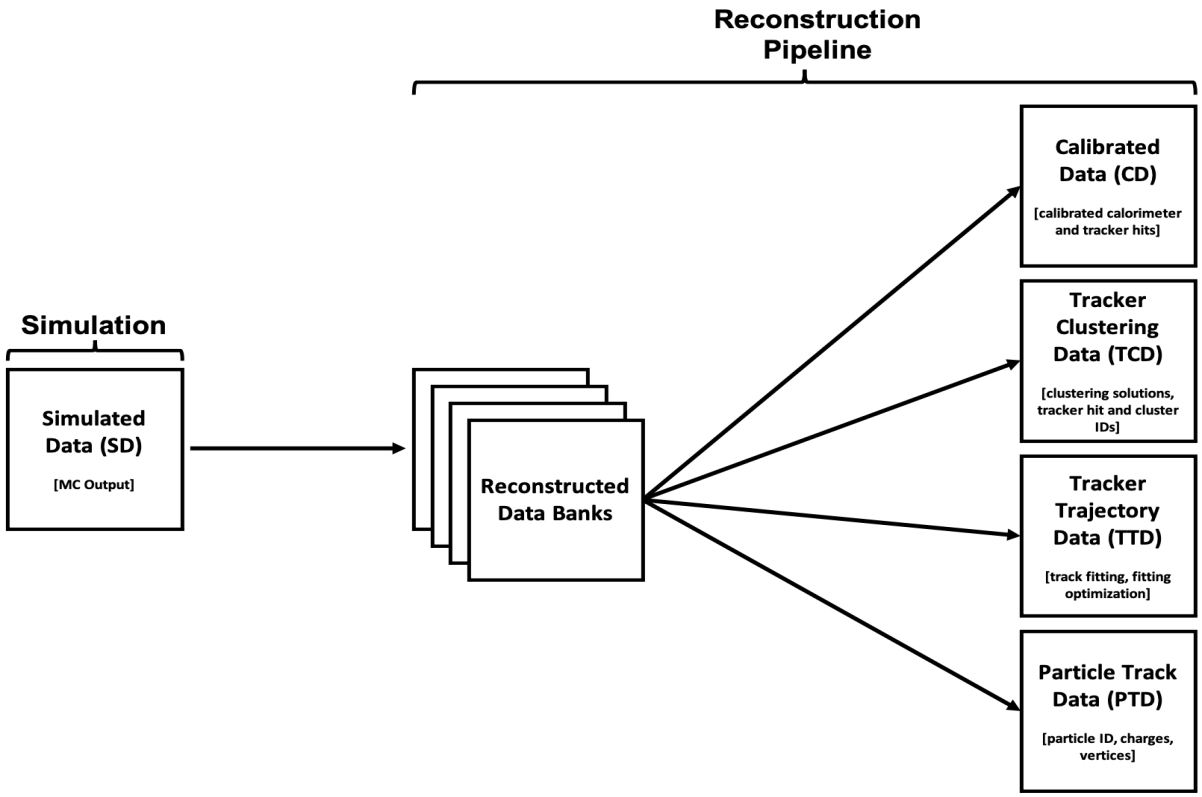

Figure 4.1: Visualization of the Falaise pipeline structure, beginning with simulation and ending with the stored data banks for reconstructed data.

Data production follows the route displayed in Figure 4.1. Firstly, events are simulated as described in section 4.1.1, after which the simulated data is processed via a reconstruction pipeline to generate reconstructed data (section 4.1.2). Reconstructed data incorporates detector effects such as noise and energy resolution into the simulated data, producing data in the same format as the detector electronics.

4.1.1 Simulation

Flsimulate is the main simulation tool for SuperNEMO. Flsimulate is a command line program which accepts a configuration file that provides instructions for simulating events. The configuration file allows the user to determine multiple criterion for simulation, including;

- The initial decay particle
- The availability of raw data for secondary particles. Secondary particles are generated as a result of primary particle interactions with the detector (as described by GEANT4).
- Location of the decay vertex
- Number of simulations
- Magnetic field configuration

The DECAY0 event generator [123] is responsible for generating the initial radioactive decay particle with appropriate energies, timing, kinematics and branching ratios. Propagation of decay particles through the detector is determined by the object-oriented toolkit GEANT4 [124], which simulates the interactions of decay particles with the detector geometry and materials. GEANT4 also manages detector hits, tracks and visualisation for each simulated event. Flsimulate provides a default output file type of Boost over Root I/O (.brio) as suitable input for both reconstruction (flreconstruct) and visualization (flvisualize).

4.1.2 Reconstruction

The simulated output is processed with flreconstruct, using a customizable reconstruction pipeline, which runs through the raw data. Modules can be sequentially selected to generate and fill multiple data banks with reconstructed data. The reconstruction pipeline highlighted in Figure 4.1 illustrates the data banks and the types of data they include. Calibrated Data (CD) includes data with the addition of detector noise and resolution effects. Tracker Clustering Data (TCD), using pattern recognition software, stores reconstructed tracker hits and clusters. Track fitting and χ^2 optimization of the clusters is stored in the Tracker Trajectory Data (TTD) and finally particle identification is accomplished, using the CD and TTD banks as inputs in order to identify the particle charges and vertices, storing the data in the Particle Track Data (PTD) bank. Combined, the different data banks provide all the reconstructed data for simulated decays, which provides an accurate depiction of the real data that is processed during detector operation.

An additional factor for reconstruction is the fitting type used by the TrackFit pipeline module. Charged particles can either be fitted with a straight track or a helical track, determined by the χ^2 of the proposed track. χ^2 measures the agreement between the reconstructed track and the reconstructed tracker hits. The track with the lowest χ^2 is selected from amongst the calculated tracks and is fitted to the simulated track. For no field simulations we expect the charged particle

tracks to be straight and optimised to straight line fitting, however, for technical reasons, all three magnetic fields had both line and helical fitting active, which were fitted to the tracks solely based on the χ^2 value of the fitted track. Information regarding the curvature of charged particle tracks with no field was consequently discarded. Gammas are reconstructed using the gamma tracking module and are important for distinguishing the different background channels, such as eγ or e2γ.

4.1.3 Visualization

Event display visualization of both raw and reconstructed data is possible using the GUI display, flvisualize. Flvisualize provides an interface for both 2D and expansive 3D visual projections of the detector. Visualised data is shown within the framework of the detector to allow for visual analysis of simulations. The left hand panel of flvisualize provides a 2D display of either the top, side or front of the detector. The second panel displays a 3D projection of the detector including all three spatial dimensions. Flvisualize also provides multiple panels, including a 'Tracks' panel, which displays reconstructed data structures with selective visuals, allowing the user to determine which visuals they wish to display. The remaining panels, 'Options' and 'Selections', provide additional functions however they are unimportant.

4.1.4 Secondary Particle Information

Secondary particle information provides increased true/GEANT level information, including additional insight into interactions of simulated particles with the detector materials, producing secondary particles. Secondary particle information provides the following:

i Particle designation (electron/positron/photon) for all true simulated particle tracks

ii Particle classification (primary or secondary) contingent on if the particle originated from the initial decay (primary) or from any other source (secondary)

iii Number of true GEANT level hits for each particle track

iv Simulated true track visuals in flvisualize

Additional simulations, with access to secondary particle information, were simulated in order to shed more light on the underlying mechanism behind the considerable number of double beta candidate events from external ^{208}Tl on the 8" Main wall PMTs. Understanding the underlying mechanism allowed for the background to be explicitly targeted and removed, in order to reduce the total background contamination, as will be discussed in chapter **??**.

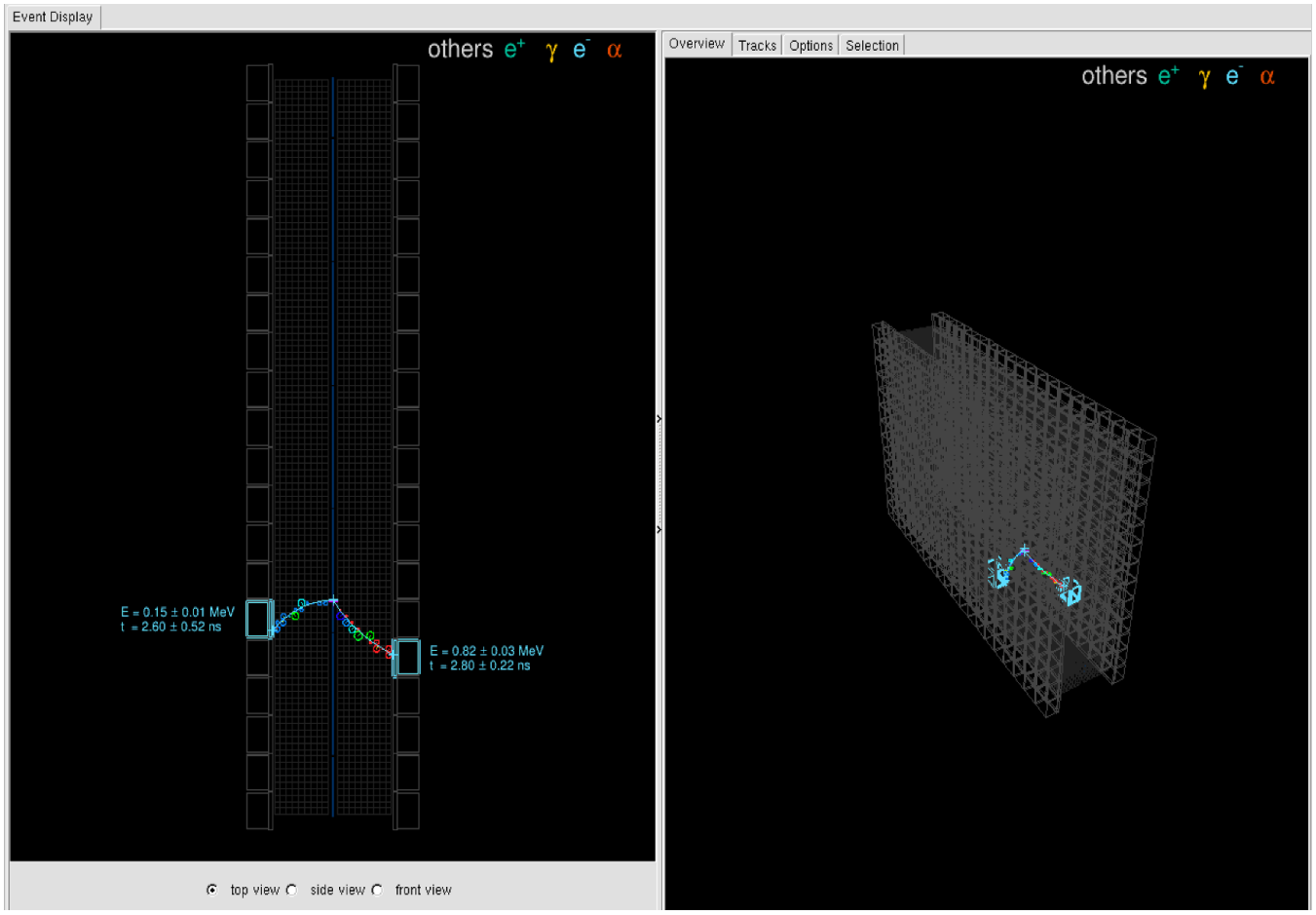

Figure 4.2: User interface of the Flvisualize tool used for visually displaying simulated and reconstructed events. The left hand side displays a 2D top view of the detector whereas the right hand side displays a 3D projection of the detector parallel to the foil. The user interface illustrates a double beta decay occurring at the source foil, resulting in the emission of two electrons from the source foil, which come to rest in the calorimeters, following propagation through the foil.

4.1.5 Sensitivity Module

Sensitivity Module is a Falaise pipeline module which converts stored data from the Falaise data banks into easily readable ROOT nTuples. Sensitivity Module uses the output from flreconstruct to generate nTuples containing both simulated and reconstructed data. The combination of true and reconstructed data forms can be used to validate an analysis, by ensuring the true data supports inferences made using the reconstructed data.

Sensitivity Module can be uniquely compiled to add supplementary nTuple branches, containing

a multitude of variables that may not already be encompassed into the pipeline. This allows additional parameters to be investigated as long as they can be computed from the Falaise data banks. By establishing the parameters necessary for identifying double beta decays, the selected parameters can be used to devise a double beta candidate cut flow.

The cut flow is a sequential application of data cuts, to determine the number of events in a particular decay channel, such as the 2e signal channel or one of the many background channels (eα and eγ). Events that pass all of the selected cuts are labelled as candidate events for the corresponding decay channel. During experimentation, the cut flow will be used on real data to probe various channels. By measuring the efficiency of reconstructing backgrounds in the two electron channel, the contribution of individual backgrounds to the $0\nu\beta\beta$ sensitivity can be determined.

4.2 Reconstructed Topologies

To identify double beta candidate events from reconstructed data, the reconstructed topology of charged particles must first be established so that the corresponding cuts can be identified and applied to the Sensitivity Module root nTuples. A double beta candidate event, in the 2e channel has a two electron topology, so the reconstructed topology of two electrons are combined. For the multitude of different backgrounds channels like eα and eγ, the reconstructed topologies of the photon and alpha particle are required.

4.2.1 Electrons and Positrons

Electrons are the primary particles for double beta decay so it is vital they are identified and differentiated from other particle topologies. Within the Falaise environment, the light charged particles (electron/positron) are characterized by a curved reconstructed track, with a vertex on the source foil (for events which originate in the source foil) and an associated calorimeter hit, as defined above. For radon in the tracker the vertex is located outside of the source foil. An example of a double beta decay event, with the origin at the source foil and two coincident electrons is illustrated in figure 4.3. The subtle difference between the particle topology of an electron and a positron is the curvature of the track under an applied magnetic field as shown in Figure 4.4. As a result of its' positive charge, the positron curves in the opposite direction to the electron; clockwise from a top down perspective. Whereas the negatively charged track curves anti-clockwise from a top down view. The curvature of a charged particle is also dependant upon the direction of travel, so for a positron travelling from the calorimeter to the source, the direction of curvature is identical to an electron travelling from the source to the calorimeters and vice versa. Charged particles travelling from the calorimeters to the foil can still be differentiated from source electrons by using timing and time of flight cuts (section 4.3). Internal and External probability can also be used to identify crossing electrons (Figure 4.5) as the two electron tracks are not coincident and are separated by the time it takes for the crossing electron to reach the source foil after being scattered by the incident gamma.

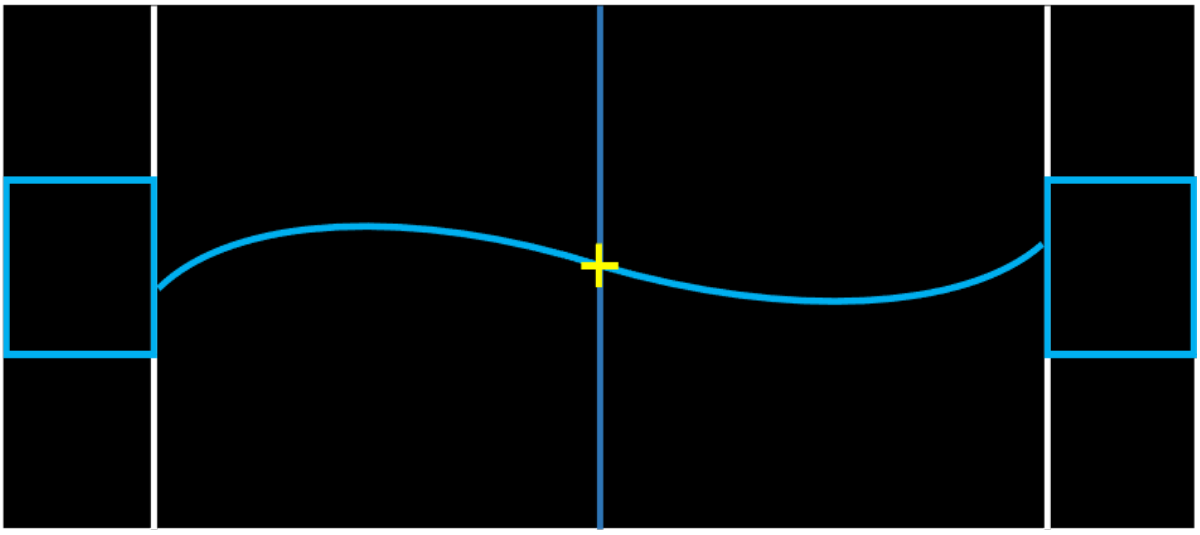

Figure 4.3: Representation of a reconstructed event with two charged particle tracks, both of which are electrons (blue track), with an initial decay vertex on the source foil.

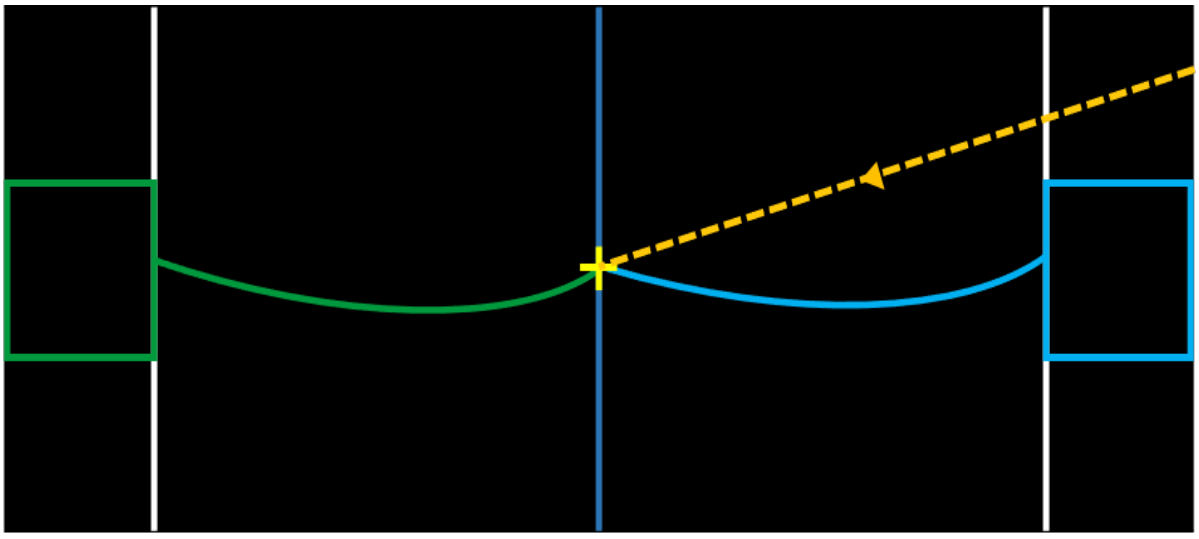

Figure 4.4: Representation of a reconstructed event with two charged particle tracks, the first belonging to an electron (blue track) and the second to a positron (green track) induced by an incident external gamma. The gamma particle interacts with the source foil, undergoing pair production, producing the electron positron pair.

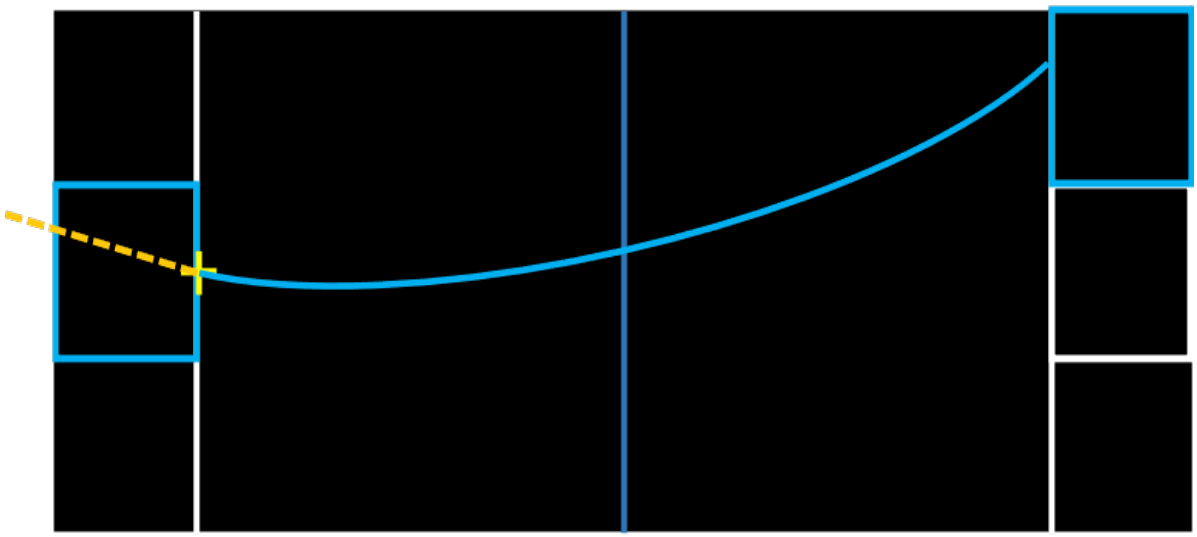

Figure 4.5: Representation of a reconstructed event with two charged particle tracks, both of which are electrons (blue track), induced by a gamma particle Compton scattering a crossing electron at the surface of the scintillator. The crossing electron traverses the detector producing two non coincident electron tracks. E and t represent the energy and timings of the respective calorimeter hits.

Electrons and positrons are identical under reconstruction until the charge is identified. For no field there is no separation of charge and so electrons and positrons cannot be differentiated. By separating electrons and positrons, double beta candidate events that involve positrons can be identified and removed. The most significant source of positrons for the SuperNEMO demonstrator is the pair production from gamma particles interacting with the source foil, as illustrated in section 3.3. Differentiating positrons from electrons provides a useful mechanism for removing the gamma contamination. The electron topology is most important for probing the 2e channel which is the decay channel used to search for neutrinoless double beta decay. The requirements for double beta candidate events in the two electron channel will be discussed in section 6.1.

4.2.2 Gammas

When attempting to identify and measure the activities of selected backgrounds, it is important to establish the reconstructed topology of particles other than the electron and positron. Neutrinos are of course undetectable by the SuperNEMO demonstrator however the detector does allow for both photons and alpha particles to be identified. As discussed in section 3.3, ^{208}Tl and ^{214}Bi are the two prominent background beta decays for SuperNEMO. The beta decay of ^{208}Tl results in the emission of multiple photons alongside the beta electron and ^{214}Bi beta decay is followed by the emission of a delayed alpha particle (figures 6.1 and 6.2). Establishing the additional particles that constitute these background decays helps to identify and remove them, reducing the total background count.

Unlike electrons and positrons, photons do not leave tracks in the detector and can only be identified by unassociated calorimeter hits, that is, calorimeter hits with no associated track or initial vertex. Furthermore, the time of flight cuts (internal and external probabilities) can be used to determine whether the timing of the unassociated calorimeter hit corresponds to that of a photon or an electron travelling from the source foil to the calorimeter. Calorimeter hits with energies lower than the detector trigger energy of 50 keV are labelled as noise regardless of whether there is an associated track or not. During visualization, gammas can be identified by a yellow calorimeter hit with a dashed yellow line originating at the particle source, as illustrated in Figure 4.6.

The 1e2γ channel is the main gamma background channel and the primary channel for measuring the contamination of ^{208}Tl. The 1e2γ channel contains events with a single electron accompanied by two photons. For ^{208}Tl, the majority (99.8%) of decays result in the emission of a high energy 2.6 MeV photon which is often emitted alongside a number of lower energy photons. The decay scheme of ^{208}Tl is complicated (figure 6.1) and can result in more than two photons being emitted from the decay, however the most populated background channel is the 1e2γ channel. Measuring eNγ channels combines the reconstructed topologies of the electron and gamma, with addition of a shared vertex between the particles. Similarly, ^{214}Bi decays can result in the emission of multiple photons although the addition of the delayed alpha in ^{214}Bi beta decay allows for it to be measured in the 1e1α decay that will be discussed in the following section.

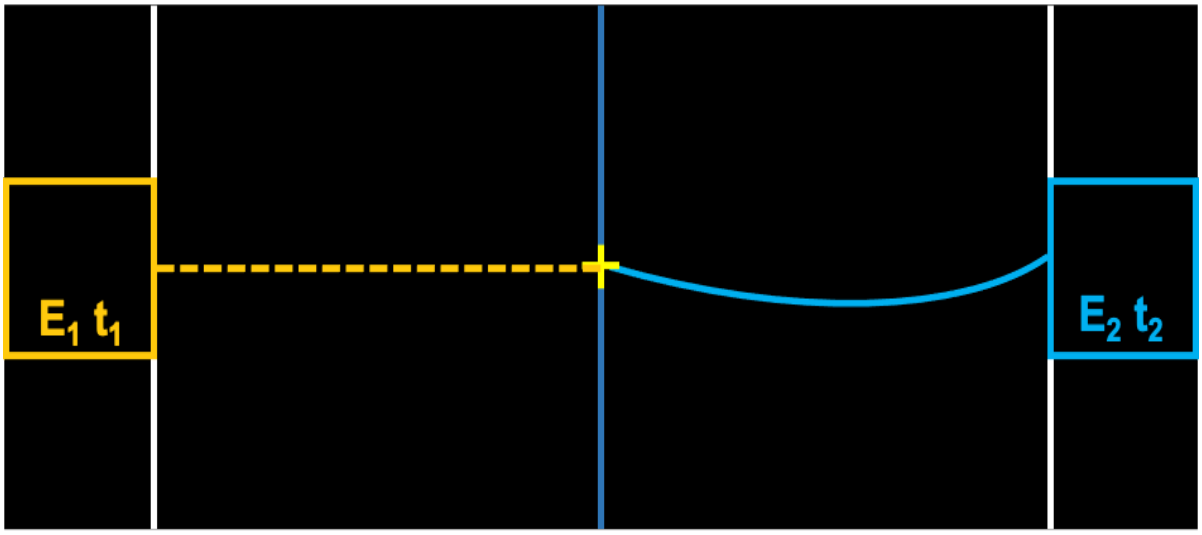

Figure 4.6: Representation of a reconstructed event with one electron (blue track) as well as a photon (yellow calorimeter hit with an unassociated/dashed track), with an initial decay vertex on the source foil. E and t represent the energy and timings of the respective calorimeter hits.

4.2.3 Alphas

Alpha particles have short straight delayed tracks, confined to the tracker volume. The large mass of the alpha particle suppresses it's propagation through the tracker and it rapidly loses its' energy within the tracker in close vicinity to the source foil. The main source of alpha particles for SuperNEMO is the beta decay of ^{214}Bi to ^{214}Po, from the ^{238}U decay chain shown in Figure 3.10. ^{222}Ra diffuses into the tracker volume and undergoes a number of decays, eventually resulting in the presence of ^{214}Bi on the surface of the source foil and tracker wires. ^{214}Bi undergoes beta decay to ^{214}Po which subsequently decays via alpha emission, with a half-life of 164.3 μs. The short red track in Figure 4.7 demonstrates a typical reconstructed delayed alpha track alongside an electron. As mentioned earlier in the chapter, the number of tracker hits for a reconstructed alpha can be fewer than the three tracker hits required for a charged particle track. For non delayed tracker hits that are not part of a larger track, the hits are registered as noise, whereas isolated delayed hits are reconstructed as alphas.

Reconstructed alphas permit the BiPo (^{214}Bi-^{214}Po) activity to be measured in the 1e1α channel, throughout the detector. The rate of 1e1α decays and consequently the BiPo activity within the different parts of the detector can be used to determine the contamination level of ^{214}Bi at those locations. For the 1e1α channel, the reconstructed variables outlined for the electron and alpha, are combined with the following additional constraints:

- There only being one prompt track

- The delayed alpha track occurs at least 4μs after the prompt electron with an upper limit of 700 μs
- The two tracks share a vertex

As no other SuperNEMO background produces a delayed alpha, the 1e1α channel can be precisely measured to determine the BiPo activity.

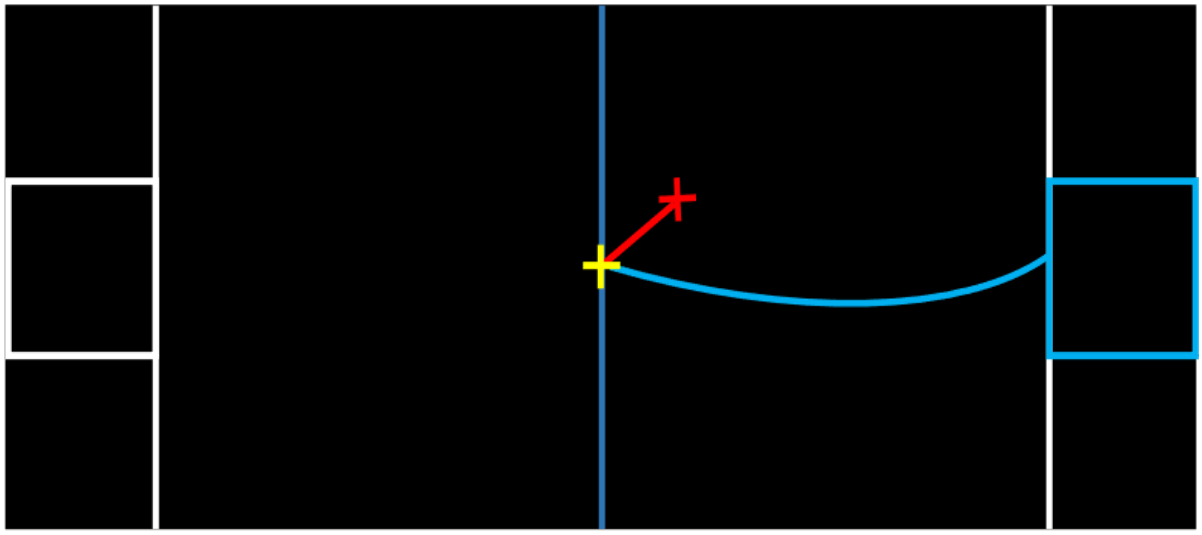

Figure 4.7: Representation of a reconstructed event with one electron (blue track) as well as an alpha (short red track), with an initial decay vertex on the source foil.

4.3 Internal/External Hypothesis

Any internal contribution, whether signal ($0\nu\beta\beta$) or background, must originate from within the source foil and should not be induced by interactions originating from a source external to the source foil. Time of flight information is used to establish the origin of the initial decay. The time of flight cuts used are the internal and external probabilities, which estimate the probability that a reconstructed event was induced by a decay interior or exterior to the source foil respectively. To do this, the internal/external hypothesis measures whether the two calorimeter hits are coincident or not (taking into account the time resolution), using the timing of the calorimeter hits. The external probability does not differentiate between an event originated from radon in the tracker or one of the many external background sources outlined earlier. For $0\nu\beta\beta$, time of flight information is most useful for identifying and removing double beta like events that may have originated from a source external to the source foil, whilst simultaneously the internal probability is used to ensure that any real double beta decays originated from within the source foil.

The internal hypothesis assumes a measured particles originated from within the source foil and the probability of this hypothesis can be calculated using the calorimeter hit timing of the particles. To calculate the internal probability, given two different calorimeter hit times t_1^{meas} and t_2^{meas}, first the theoretical time of flight t_i^{tof} is calculated using

$$t_i^{\text{tof}} = \frac{l_i}{\beta_i} \tag{4.1}$$

with l_i the length of the particle track which is curved for charged particles and straight line for photons. Additionally, for photons $\beta_i = 1$ and for electrons is calculated using

$$\beta_i = \frac{\sqrt{E_i\left(E_i + 2m_e\right)}}{E_i + m_e} \tag{4.2}$$

with E_i the calibrated energy recorded by the calorimeter and m_e the rest mass of an electron. The emission time of a particle, t_i^{int}, takes into account the measured time in the calorimeter as well as the theoretical time of flight and is given as

$$t_i^{\text{int}} = t_i^{\text{meas}} - t_i^{\text{tof}} = t_i^{\text{meas}} - \frac{l_i}{\beta_i} \tag{4.3}$$

A χ^2 test representing the approximately Gaussian timing distribution is used with the corresponding χ^2 variable

$$\chi^2_{\text{int}} = \frac{\left(\left(t_1^{\text{meas}} - \frac{l_1}{\beta_1}\right) - \left(t_2^{\text{meas}} - \frac{l_2}{\beta_2}\right)\right)^2}{\sigma^2_{t_1^{\text{int}}} + \sigma^2_{t_2^{2}\text{int}}} \tag{4.4}$$

where $\sigma^2_{t_i^{\text{int}}}$ represents the variance of the emission timing t_i^{int} . $\sigma^2_{t_i^{\text{int}}}$ depends on multiple factors including the uncertainties on the measured time, particle speed and distance travelled. For photons, the particle speed is c and so there is no uncertainty on this value, however the uncertainty surrounding the path length is unknown as photons are not tracked in SuperNEMO.

χ^2_{int} is converted into a probability by transforming the Gaussian distribution into a flat distribution between 0 and 1. The internal probability is therefore defined as

$$P\left(\chi^2_{\text{int}}\right) = 1 - \frac{1}{\sqrt{2\pi}} \int_0^{\chi^2_{\text{int}}} x^{-\frac{1}{2}} e^{-\frac{x}{2}} dx \tag{4.5}$$

Unlike the internal hypothesis, the external hypothesis assumes an incident external photon interacts with the detector to produce either a 1e1γ event or a crossing electron. The external background results in the generation of an event in the 2e channel via a number of mechanisms that will be outlined later on. Calculating the external probability is done in a similar manner to the internal probability, but the time of flight t^{tof} is given as

$$t^{\text{tof}} = \frac{l_1}{\beta_1} + \frac{l_2}{\beta_2} \tag{4.6}$$

which sums the timing for both particle tracks.

The χ^2 for the external hypothesis is then

$$\chi^2_{\text{ext}} = \frac{\left((t_2^{\text{meas}} - t_1^{\text{meas}}) - \left(\frac{l_1}{\beta_1} + \frac{l_2}{\beta_2}\right)\right)^2}{\sigma^2_{t_1^{\text{ext}}} + \sigma^2_{t_2^{\text{ext}}}} \tag{4.7}$$

where $\sigma^2_{t_i^{\text{int}}}$ is the equivalent variance of emission for the external hypothesis. Like the internal probability in equation 4.5, the external probability is calculated with

$$P\left(\chi^2_{\text{ext}}\right) = 1 - \frac{1}{\sqrt{2\pi}} \int_0^{\chi^2_{\text{ext}}} x^{-\frac{1}{2}} e^{-\frac{x}{2}} dx \tag{4.8}$$

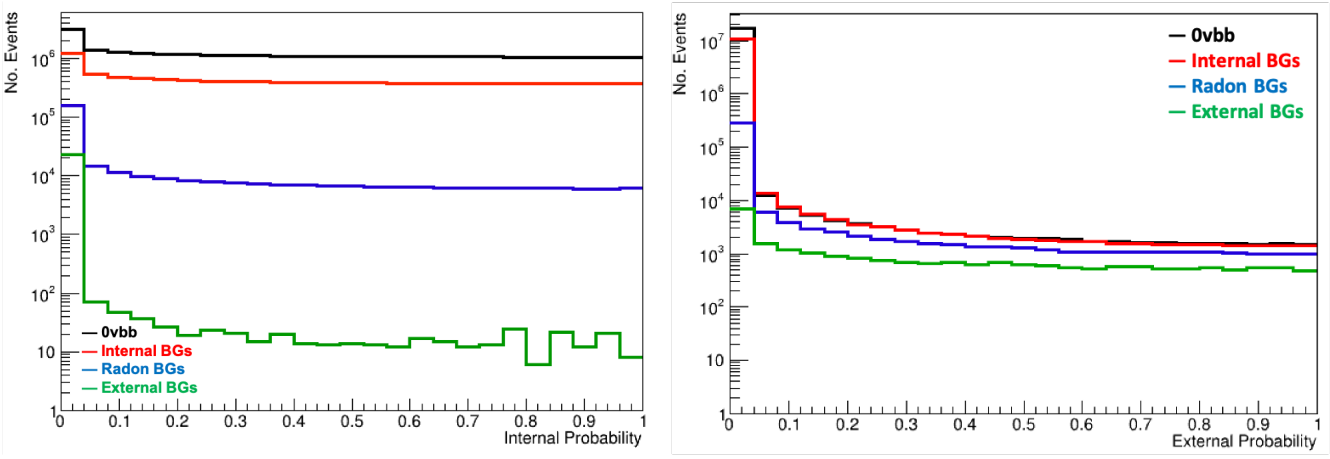

(a) Internal probability

(b) External probability

Figure 4.8: Internal (a) and external (b) probabilities for $0\nu\beta\beta$, internal, radon and external backgrounds with reconstructed 2e topologies. The probability distributions were calculated using the equations 4.5 and 4.8 respectively.

4.4 Figure of Merit Calculation

The purpose of this work is to quantify and compare the performance of the SuperNEMO demonstrator module using the three magnetic field configurations outlined in section 3.4. A Figure Of Merit (FOM) is used to measure the performance of the three magnetic fields and for this work the FOM is the half-life sensitivity described in section 4.4.2. To calculate the FOM, the detection efficiency (or survival probability for background simulations) is computed using Equation 4.9. The detection efficiency (survival probability) is subsequently used to calculate the number of expected events (Equations 4.10 - 4.13), which is finally inputted into the half-life sensitivity (Equation 4.19) to calculate the FOM for the three fields. In the following section the parameters needed to calculate the FOM will be derived alongside the half-life sensitivity equation.

4.4.1 Number of Expected Events

In order to determine the contribution of different backgrounds to a decay channel (for $0\nu\beta\beta$ this is the 2e channel), the number of expected events (N_{exp}) of the background is first calculated. The number of expected events represents the total number of expected decays of a particular background during the detectors operational lifetime. The number of expected events uses the two electron detection efficiency (Equation 4.9 also referred to as the survival probability for background simulations) and the corresponding activity of the decay in order to estimate the expected number of decays.The ratio of successfully reconstructed events in a given channel, from a known number of Monte Carlo simulations is denoted the detection efficiency and is given as the following,

$$\epsilon = \frac{N_{Survived}}{N_{TOTMC}} \tag{4.9}$$

with $N_{Survived}$ equal to the number of events that pass all the cuts and N_{TOTMC} the total number of simulated events. The number of expected events of ^{82}Se two neutrino double beta decay, in the source foil, is given by,

$$N_{2\nu\beta\beta} = \frac{N_A \times \ln 2 \times \epsilon \times m \times t}{T^{2\nu\beta\beta}_{1/2} \times M(^{82}Se)} \tag{4.10}$$

where N_A is Avogadro's constant, ϵ is the previously quoted reconstruction efficiency ratio, m is the total mass of the ^{82}Se source foil (6.23 Kg), t is the total run time of the experiment, $T^{2\nu\beta\beta}_{1/2}$ is the half life of ^{82}Se and $M(^{82}Se)$ is the mass number for ^{82}Se. For other internal backgrounds, such as ^{208}Tl and ^{214}Bi, the number of expected events is

$$N_i = A_i \times \epsilon_i \times m \times t \tag{4.11}$$

with A_i and ϵ_i designated as the activity and reconstruction efficiency respectively, for background i.

Radon induced backgrounds are calculated using the activity of the background within the volume of the tracker chamber. The volume of the tracker replaces the source foil mass in equation 4.11 and so the number of expected events for Radon simulations is given by,

$$N_i = A_i \times \epsilon_i \times V \times t \tag{4.12}$$

with V as the volume of the tracker chamber. External backgrounds were only simulated on the PMT glass bulbs, so the activity is a proportion of the total activity from the entire PMTs. The number of expected events for external backgrounds is given by,

$$N_i = A_{Glassbulb,i,j} \times \epsilon_i \times t \tag{4.13}$$

with $A_{Glassbulb,i,j}$ the activity of the PMT glass bulb for a given background i and PMT location j.

4.4.2 Half-Life Calculation: Window Method

The sensitivity of an experiment is often given as a half-life $T_{1/2}$, which incorporates the detection efficiency and N_{exp} from section 4.4.1. To derivation of the half-life formula is shown below, starting with the exponential decay of a radioactive isotope,

$$N(t) = N(0)e^{-\lambda t} \tag{4.14}$$

with $N(t)$ the number of remaining atoms of the isotope at time t, $N(0)$ the number of atoms at the beginning of the experiment and λ the decay constant. λ is related to the half-life $T_{1/2}$ by the following

$$\lambda = \frac{\ln(2)}{T_{1/2}} \tag{4.15}$$

The half-life of two neutrino ^{82}Se double beta decay is approximately of the order 10^{20} years and even greater for neutrinoless double beta decay so equation 4.14 can be Taylor expanded in λt to give the approximation

$$e^{-\lambda t} \simeq (1 - \lambda t) \tag{4.16}$$

The number of observed events can therefore be written as

$$N_{\text{obs}} = \epsilon N(0)\left(1 - e^{-\lambda t}\right) \simeq \epsilon N(0)\lambda t = \epsilon N(0)\frac{\ln(2)}{T_{1/2}}t \tag{4.17}$$

with the ϵ the detection efficiency of $0\nu\beta\beta$ and t the running time of experimentation. The number of atoms at the beginning of the experiment, N(0) is given by

$$N(0) = \frac{N_A m}{A} \tag{4.18}$$

and by inserting the definition of $N(0)$ into equation 4.17, the half life of $0\nu\beta\beta$ can be calculated using

$$T_{1/2}^{0\nu\beta\beta} = \frac{\epsilon}{N_{90\%\,\text{CL}}}\frac{N_A m}{A}\ln(2)t \tag{4.19}$$

where $N_{90\%\,CL}$ represents the number of counts with a 90% confidence level upper limit, providing a lower limit for $T_{1/2}^{0\nu\beta\beta}$.

There are various methods to approximate the half-life sensitivity established in section 4.4.2 , the most common of which use the full energy spectrum of both signal and background, separating them to determine their respective contributions. In this thesis, a basic counting approach (or window method) is utilized and uses the number of expected events found in a selected energy window to calculate the half-life. For ^{82}Se neutrinoless double beta decay, the initial counting window is established as 2.8 to 3.2 MeV (highlighted in Figure 4.9), encompassing the ^{82}Se Q value, corresponding to the peak of the $0\nu\beta\beta$ energy distribution. Counting methods are less precise than the more thorough complete energy spectrum methods, however as this thesis is a comparative analysis to determine which of the three magnetic field is most suitable for detector operation, a less precise but relative study between the three magnetic fields is beneficial. By attempting to compare the relative performance of the three magnetic fields, the precision of the sensitivity estimation can be compromised in order to increase the speed of the analysis.

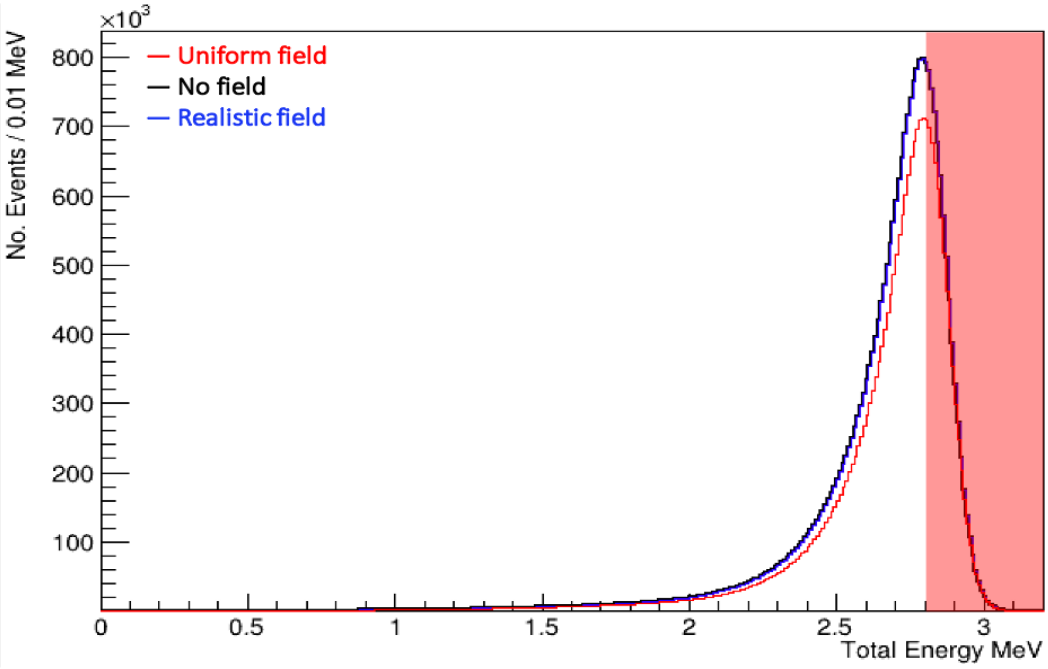

Figure 4.9: $0\nu\beta\beta$ total energy spectra for the three magnetic field configurations, with the region of interest (2.8 - 3.2 MeV) highlighted in red.

4.5 Limit Setting Procedures

As mentioned, for this work, a counting approach is utilized for estimating the half-life sensitivity of the SuperNEMO demonstrator. The method for calculating the counting method FOM (outlined in Section 4.4), requires the number of observed events (N_{obs} or $N_{90\%\,\text{CL}}$ for setting a lower limit on the half-life) to be calculated and inserted into the half-life illustrated in Equation 4.19. The first counting method is a Gaussian approximation, which is particularly useful for studies with low numbers of expected backgrounds. For the Gaussian approximation at 90% CL, $T^{0\nu}_{1/2}$ is defined as,

$$T^{0\nu}_{1/2} > 4.16 \times 10^{26}\text{yr} \left(\frac{\epsilon a m t}{M(^{82}Se)}\right)\left(\frac{1}{1.64\sqrt{N_B}}\right) \tag{4.20}$$

with ϵ the efficiency of detecting 0vbb (from equation 4.9), a the isotopic abundance (given as 1 for the refined source foil), mt the exposure, $M(^{82}Se)$ the ^{82}Se mass number and N_B the number of expected background events. The $\sqrt{1.64}$ denominator term represent a 90% confidence level (CL). Although not as precise as the other methods, the Gaussian approximation is a simple and fast approach for comparing the performance of three magnetic field configurations, although as the number of background events increases, the precision of the Gaussian approximation reduces significantly.

An alternative to the Gaussian approximation is the Poissonian approximation which provides greater precision for an analysis with increased statistical data. Poissonian approximations use equation 4.19 with the extraction of N_{obs} dependent upon a selected method. The method used to calculate the number of observed events is the Minimum Detectable Activity (MDA) method [125], which are outlined below.

4.5.1 Minimum Detectable Activity

In this thesis, the definition used for the minimum detectable activity is given in 'Radiation Detection and Measurement' by G. F. Knoll [125]. Knoll uses a binary pretence of whether the detector output represents a background only or a combination of backgrounds plus signal. By establishing the probability of a false positive as an identified signal even though only background is present and a false negative as the probability a signal is misidentified as a background, a critical count number n_c can determine the minimum threshold count, above which a signal is present.

For a Poisson distributed background B and a probability of a false positive less than 1 - CL, n_c must be increased until the following is satisfied,

$$P_B\left(n \geq n_c\right) = \sum_{n=n_c}^{\infty} Pois(n;B) = 1 - \sum_{n=0}^{n_c-1} e^{-B}\frac{B^n}{n!} \leq 1 - \text{CL} \tag{4.21}$$

Once the probability of a false positive is reduced to below 1 - CL, the false negative probability is used to calculate the minimum expected signal count S. S can be determined by increased it's value until the following equation is satisfied,

$$P_{S+B}\left(n < n_c\right) = \sum_{n=0}^{n_c-1} \text{Pois}\left(n; S+B\right) = \sum_{n=0}^{n_c-1} e^{-(S+B)} \frac{(S+B)^n}{n!} \leq 1 - \text{CL} \tag{4.22}$$

The MDA method is illustrated in Figure 4.10, with the black curve representing the Poisson distributed background B and the red curve representing the combined signal and background expectation. Both shaded areas illustrate the 1 - CL from equations 4.21 and 4.22. For the purpose of this work, the confidence level is set at 90% and so the shaded areas represent 10% of the total area of each curve. The minimum signal S and critical count n_c are then used to determine N_{obs} ($N_{90\%\,\text{CL}}$), in order to set a half-life limit using equation 4.19.

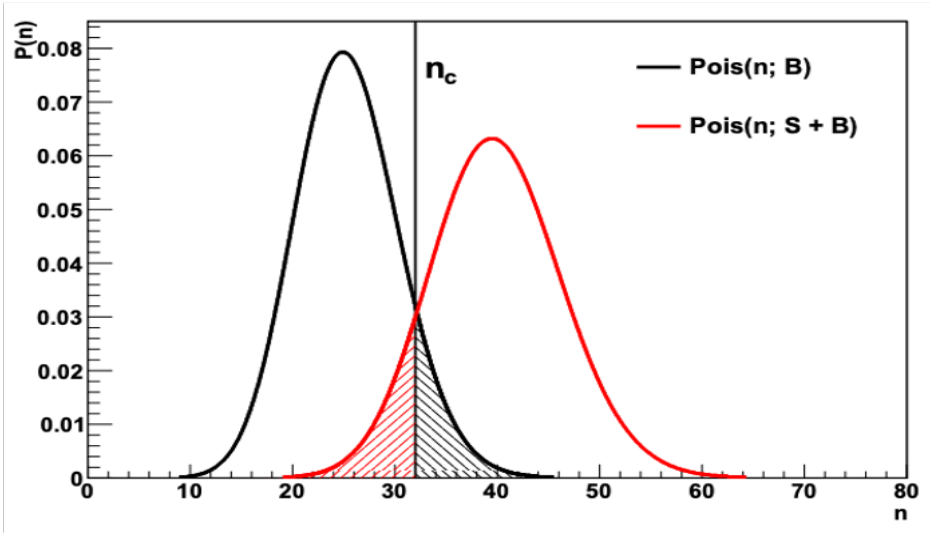

Figure 4.10: Probability distributions for the two Poisson variables, B and $S+B$. The black curve represents the background distribution and the red curve signal + background, with the shaded areas each corresponding to 1 - CL [7].

Chapter 5

Double Beta Decay Event Selection

The sensitivity to neutrinoless double decay is the primary metric of success for the magnetic field analysis described in this work. The results from the double beta decay simulations (signal) will be discussed, including the impact of the 2e topology cuts from chapter 4 on the concurrent and final detection efficiency for each of the three magnetic field scenarios. For the $0\nu\beta\beta$ analysis, $2\nu\beta\beta$ is treated as a background and contributes to the total background contamination. The high energy window/region of interest established in the previous chapter ensures the contamination of $2\nu\beta\beta$ is suppressed however a very small number of $2\nu\beta\beta$ events still remain. Additionally, the best case scenario SuperNEMO detector will be discussed, that is, a radiopure detector with only $2\nu\beta\beta$ as an irreducible background to $0\nu\beta\beta$. With improved processing methods it may be feasible to reduce or eliminate other backgrounds, improving detector conditions for probing neutrinoless double beta decay.

5.1 Neutrinoless Double Beta Decay ($0\nu\beta\beta$)

The primary goal of the SuperNEMO experiment is to search for the neutrinoless double beta decay of ^{82}Se, by optimising the sensitivity of the detector to the decay. Parallel to this, SuperNEMO aims to improve on the previous half-life measurement for the two neutrino decay of ^{82}Se and increase the precision of the two neutrino decay nuclear matrix elements. In order to determine the neutrinoless double beta decay sensitivity, the detection efficiency of $0\nu\beta\beta$ (equation 4.9) must first be extracted from simulated data. For each of the three magnetic fields, 10^8 simulated decays of $0\nu\beta\beta$ were uniformly distributed in the bulk of the source foil using the official Falaise 4.0.0 reconstruction with an exposure of 15.25 Kg yr^{-1} (6.1 Kg $\times$ 2.5 years). As previously mentioned, the cut flow is applied to simulated data in order to extract $N_{Survived}$, which is used to calculate the detection efficiency of the simulated isotope in the 2e channel and is briefly described below.

5.2 Identifying Double Beta Events

The search for ^{82}Se neutrinoless double beta decay is measured in the two electron channel, but not all events found in the two electron channel are necessarily from real double beta decays and may in fact materialise from specific backgrounds. The reconstructed topology of an electron was established, in section 4.2.1, as a negatively curved track with a vertex on the source foil (for events which originate within the source foil) and an associated calorimeter hit. For a double beta candidate event in the 2e channel, the reconstructed topologies of two electrons are combined with additional constraints, all of which are outlined below.

5.2.1 2e Channel Selection

- Two calorimeter hits

  Two calorimeter hits above 50 keV, with at least one hit above 150 keV, measuring the energies of the two double beta decay electrons. The minimum energy requirement is determined by the trigger energy of the detector.

- Two tracker clusters and two tracks

  Two tracks, derived from two tracker clusters are selected to represent the tracks of the two emitted electrons during double beta decay.

- Each track associated to a unique calorimeter

  Each track is associated to a calorimeter ensuring the two beta electron tracks correspond to the two calorimeter hits. One of the main benefits of SuperNEMO is that it allows the energy of each individual electron to be measured which can only be achieved when electrons hit separate calorimeters.

- Two vertices on the source foil

  The two electron vertices should be located on the source foil, ensuring a reconstructed path from the foil, through the tracker and finally into the calorimeters for the two electrons.

- Internal and External Probability

  The timing of the calorimeter hits must be within a certain boundary to ensure the electrons originated from within the source foil and did not enter the tracker from an external source. Internal and external probability essentially act as time of flight cuts. As mentioned in Section 4.3, for internal events the electrons must be coincident (within the time resolution), otherwise the event is classified as an external event.

- No Positrons

The double beta decay charged particle tracks can belong to either electrons or positrons. The charge of each track can be identified from the curvature of the track so electrons and positrons can be differentiated. Identifying both tracks as electrons is the final step for 2e selection.

5.2.2 2e Channel Optimization

The 2e channel cuts help to identify double beta candidate events however additional cuts are necessary in order to improve the the ratio of the signal detection efficiency whilst reducing the background survival probability, improving the half-life limits. Three additional optimization cuts are shown below,

- Maximum vertex separation

  The maximal separation between the vertices is ΔR <1cm and ΔZ <3cm, where ΔR represents the radial separation and ΔZ the vertical separation. The separation limits are defined by the tracker cell positional resolution, which is 1cm and 3cm for the radial and vertical resolution respectively. The maximum vertex separation targets events with electrons induced by gammas interacting with the source foil, such as the double Compton shown in Section 6.1, whereas double beta decay emits two electrons from a single vertex.

  The vertex separation cut applies a harsher constraint compared to previous studies. In [126], ΔR is required to be <6cm and ΔZ <7cm, culminating in over 95% of double beta candidate events from the source foil surviving the cut, compared to the approximately 70% survival rate with ΔR <1cm and ΔZ <3cm.

- No delayed alpha tracks

  No delayed/alpha tracks, between 13 and 700 μ. The 13 μs lower limit includes detector effects like the tracker response time and the upper limit is approximately 4 $\times$ the half-life of ^{214}Po. The delayed window is kept open so as to identify and measure BiPo decays.

- ROI energy

  No events are allowed outside of the energy window (ROI). The nominal ROI is 2.8 - 3.2 MeV for ^{82}Se, however the ROI is subject to optimization. The ROI selects a bin of a specified width for estimating the sensitivity using a counting method. The ROI cut is used to remove the majority of backgrounds which are found at lower energies, and allows the FOM to be determined by a simple counting method in the ROI.

Together, the two electron channel and optimization cuts combine to form the double beta decay cut flow, for the purpose of extracting the detection efficiency and subsequently the contribution of background decays, such as $2\nu\beta\beta$, to the ^{82}Se sensitivity. The cuts are selected in order to maximise the reconstruction efficiency of true double beta decays, whilst reducing the prevalence of

background induced two electron events. The breakdown of the $0\nu\beta\beta$ cut flow is provided in table 5.1, illustrating how the detection efficiency changes with each sequential cut. A short description of each of the cuts is provided.

	Signal Detection Efficiency		
Cut Descriptions	Uniform Field	No Field	Realistic Field
Only two calorimeter hits above 50keV, at least one >150keV	0.562	0.594	0.589
Two tracker clusters with 3 or more cells	0.380	0.446	0.436
Two reconstructed tracks	0.378	0.443	0.433
Remove events with two electron hits to the same calorimeter	0.373	0.438	0.429
Each track associated to a calorimeter	0.338	0.400	0.390
Two vertices on the source foil	0.337	0.399	0.389
Vertex ΔR <1cm and ΔZ <3cm (separation between vertices)	0.240	0.281	0.274
Internal Probability >1% and External Probability <4%	0.226	0.265	0.259
No delayed alpha tracks (no tracks with $13\mu s <$ t $< 700\mu s$)	0.226	0.265	0.259
Remove positrons (unavailable for no field)	0.211	-[†]	0.179
ROI energy (between 2.8 and 3.2 MeV)	0.0653	0.0790	0.537

Table 5.1: $0\nu\beta\beta$ cut flow for the three magnetic field configurations. Each row lists a short description of the cut as well as the concurrent detection efficiency. 10^8 $0\nu\beta\beta$ events were simulated using the light neutrino exchange (LNE) mass mechanism (Section 2.3.1).

[†]For no field, the no positron cut is not applied as without a magnetic field, the charges of the particle tracks are indeterminable. The magnetic field curves electrons and positrons in opposite directions as a result of their differing charges and so without a magnetic field, the charged particle tracks are straight, ignoring any low energy scattering.

The cut flow follows the ordering shown in section 5.2.1, however the three additional optimization cuts; the maximum vertex separation, no delayed tracks and the energy window (or ROI) are added to the cut flow as cuts seven, nine and eleven respectively. The order of the cut flow is important for studying the impact of each individual cut on the concurrent detection efficiency and importantly, understand how the different magnetic fields influence the overall final detection

efficiency. For example, the cut flow begins with the two calorimeter cut, which removes almost 50% of events, for all three magnetic fields. Requiring two calorimeter hits is most effective for removing 1e2(+)γ events that have more than two calorimeter hits and any 1e events from background decays or improper double beta decays where one of the electrons doesn't escape the foil or tracker volume. Moreover, removing events with two electron hits to the same calorimeter ensures the energy of individual electrons as well as the event topology can be identified which is one of the significant advantages of the SuperNEMO demonstrator as mentioned in Chapter 3.

5.3 Two Neutrino Double Beta Decay ($2\nu\beta\beta$)

Cut Descriptions	Background Survival Probability		
	Uniform Field	No Field	Realistic Field
Only two calorimeter hits above 50keV, at least one >150keV	0.237	0.287	0.279
Two tracker clusters with 3 or more cells	0.147	0.205	0.195
Two reconstructed tracks	0.146	0.204	0.194
Remove events with two electron hits to the same calorimeter	0.143	0.201	0.191
Each track associated to a calorimeter	0.125	0.179	0.170
Two vertices on the source foil	0.125	0.178	0.169
Vertex ΔR <1cm and ΔZ <3cm (separation between vertices)	0.072	0.101	0.096
Internal Probability >1% and External Probability <4%	0.068	0.095	0.090
No delayed alpha tracks (no tracks with $13\mu s <$ t $< 700\mu s$)	0.068	0.095	0.090
Remove Positrons (unavailable for no field)	0.063	-[†]	0.060
ROI energy (between 2.8 and 3.2 MeV)	3×10^{-8}	2×10^{-8}	1×10^{-8}
Number of Expected Events in the ROI	0.15 $\pm$ 0.09	0.10 $\pm$ 0.07	0.05 $\pm$ 0.05

Table 5.2: $2\nu\beta\beta$ cut flow and number of expected events for the three magnetic field configurations. Each row lists a short description of the cut as well as the concurrent detection efficiency. An exposure of 15.25 Kg.yr (6.1 Kg $\times$ 2.5 years) is used and value for $T_{1/2}^{2\nu\beta\beta}$ used is 9.39 $\times$ 10^{19} yrs under the single state dominance (SSD) hypothesis [130].

[†] No positron cut for no field scenario.

The cut flow for $2\nu\beta\beta$ double beta candidate events is shown in table 5.2, alongside the number of expected events with 2.5 years of exposure. The overall detection efficiency is significantly lower for $2\nu\beta\beta$ compared to $0\nu\beta\beta$, particularly in the ROI, where the detection efficiencies are of the order 10^{-8}. A low detection efficiency for $2\nu\beta\beta$ is important when measuring the sensitivity to neutrinoless double beta decay as $2\nu\beta\beta$ is the single irreducible background for the neutrinoless search.

The sum of the two electron distribution is shown in Figure 5.1. For neutrinoless double beta decay, the total energy correlates well with the expected Landau distribution seen for charged particles traversing a thin film. The distribution peaks around the decay energy of ^{82}Se (3 MeV, Figure **??**) and the Landau tail extends back to the 200 keV trigger energy. The shape of the distribution is unchanged between the three magnetic fields. The tail of the two neutrino distribution barely penetrates into the ^{82}Se ROI, resulting in the low detection efficiencies for the three fields as shown in table 5.2. The majority of $2\nu\beta\beta$ events are found at lower energies, with the peak of the distribution close to 1 MeV.

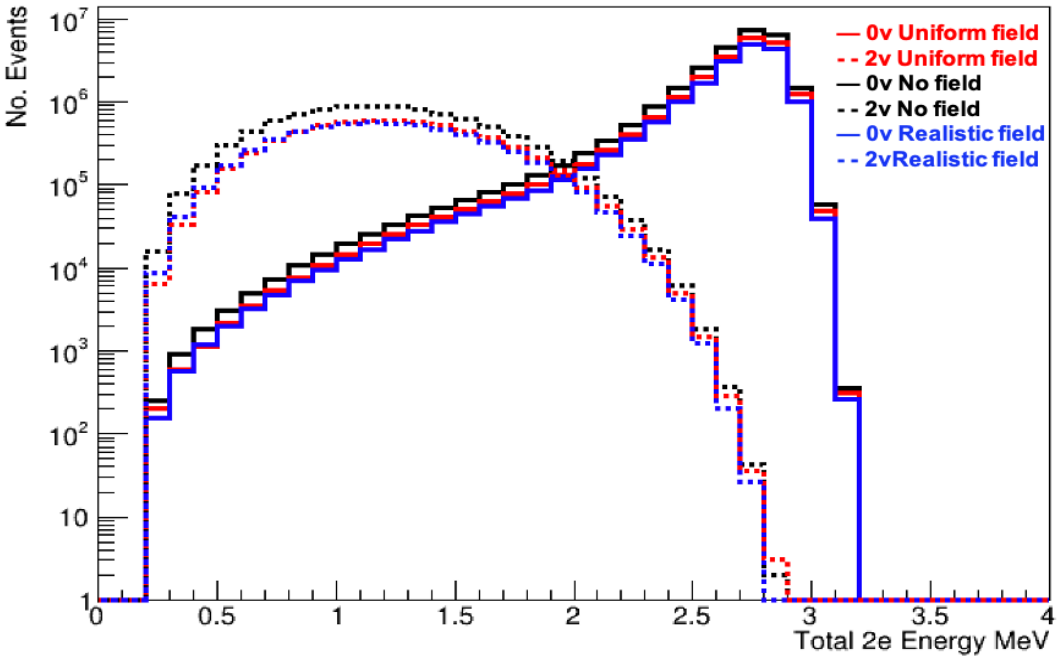

Figure 5.1: $0\nu\beta\beta$ and $2\nu\beta\beta$ total energy spectra for events with a 2e topology with all three magnetic fields. The $0\nu\beta\beta$ spectra are illustrated by the thick line and $2\nu\beta\beta$ by the dotted line. The spectra are normalised to the number of simulated events.

The modular structure of SuperNEMO provides the ability to reconstruct the entire topology of individual particles. One of the most important variables for studying the intermediate decay mechanism of ^{82}Se $0/2\nu\beta\beta$ decay, is the single electron energy. The single electron energy distribution is presented in Figure 5.2, for both $0\nu\beta\beta$ and $2\nu\beta\beta$ and can be used to infer the mechanism underlying the decay itself. The distribution shape of the total energy is independent of the magnetic field choice, for both the neutrinoless and two neutrino decays.

Similarly, the angular distribution is also sensitive to the underlying decay mechanism of $0\nu\beta\beta$ and the cosine of the angle between the two electron tracks is shown in Figure 5.3. The cosine(θ) curve for $0\nu\beta\beta$ is expected to follow a 1 - cos(θ) ***ref DBD chapter*** distribution with the addition of detector effects, however, as shown in Figure 5.3, the number of events reduces as you get closer to cos(θ) = 0. Again, both variables are important for analysing the underlying double

beta decay mechanism.

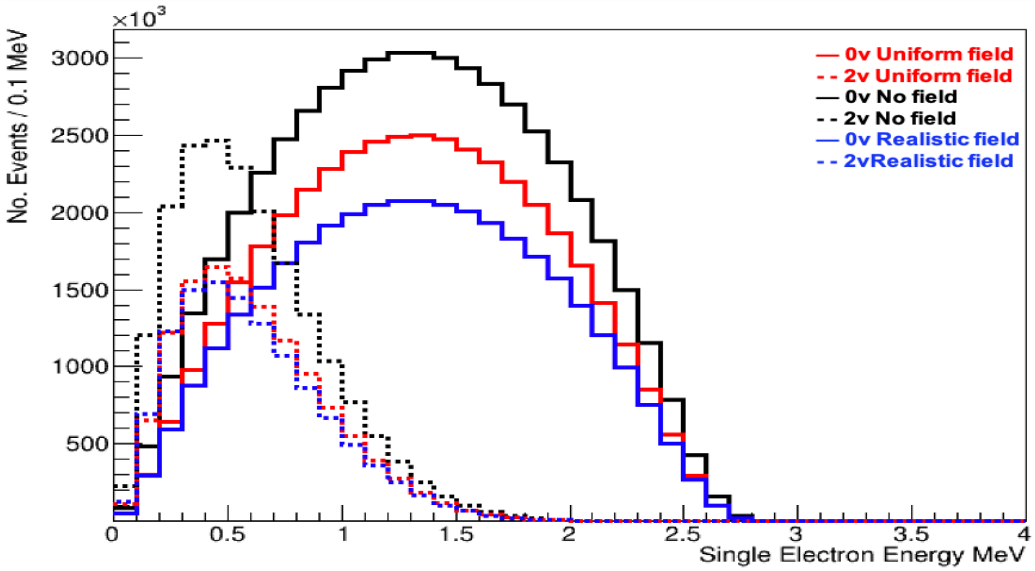

Figure 5.2: $0\nu\beta\beta$ and $2\nu\beta\beta$ single electron energy spectra for events with a 2e topology with all three magnetic fields. The $0\nu\beta\beta$ spectra are illustrated by the thick line and $2\nu\beta\beta$ by the dotted line. The spectra are normalised to the number of simulated events.

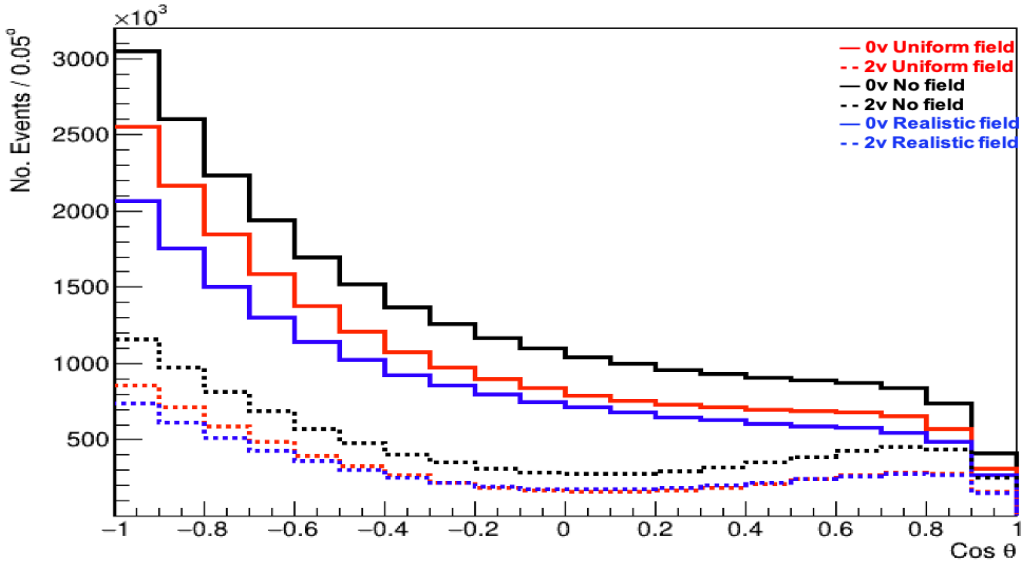

Figure 5.3: $0\nu\beta\beta$ and $2\nu\beta\beta$ $\cos\theta$ spectra for events with a 2e topology with all three magnetic fields. The $0\nu\beta\beta$ spectra are illustrated by the thick line and $2\nu\beta\beta$ by the dotted line. All events have a total energy within the ^{82}Se ROI (2.8 - 3.2 MeV). The spectra are normalised to the number of simulated events.

5.3.1 SuperNEMO Sensitivity with $2\nu\beta\beta$ Background Only

Prior to investigating the contributions from the other background sources, it is useful to consider the case of the best case scenario detector, which only includes the irreducible $2\nu\beta\beta$ as a background. Although SuperNEMO has a number of different backgrounds that contribute towards the ^{82}Se ROI, from internal, radon and external sources, it may be possible to further reduce and perhaps eliminate all of the reducible backgrounds. To reduce the internal contamination, the source foils can undergo increased processing which is made easier by the modular structure of the SuperNEMO demonstrator, allowing the source foils to be removed and replaced. Radon and external backgrounds can be reduced by improving the radon flushing inside the tracker and increasing shielding prowess respectively. Additionally the unique ability of SuperNEMO to reconstruct the topology of two electron event (as mentioned in Chapter 3), makes it possible, in principle, to reduce all backgrounds except $2\nu\beta\beta$. For the best case scenario detector, this would result in a reduction or elimination of all backgrounds leaving only $2\nu\beta\beta$. The best tool for minimising the $2\nu\beta\beta$ backgrounds contribution is the decay energy. The $2\nu\beta\beta$ total energy spectra is skewed to lower energies, whereas the $0\nu\beta\beta$ energy spectra peaks around the ^{82}Se ROI (Figure 5.1), as there are no neutrinos to reduce the energy carried by the electrons. By maximising the energy resolution, the rare $0\nu\beta\beta$ background peak can be most optimally separated from the $2\nu\beta\beta$ background continuum, particularly when probing the ROI at the ^{82}Se Q value. The width and position of the ROI is dependent upon the energy resolution of the experiment, so it is important to maximise this resolution, particularly for the ideal case scenario, where the most optimal strategy for separating the signal and 2ν background uses the measured energy of the decay progeny. The results for best case scenario are shown in Table 5.3, using the MDA method outlined in Section 4.5.1.

5.4 Summary of Double Beta Decays

	Magnetic Field Configuration		
0ν Detection Efficiency	0.0653	0.0790	0.0537
$2\nu\beta\beta$ Survival Probability	3×10^{-8}	2×10^{-8}	1×10^{-8}
$2\nu\beta\beta$ Number of Expected Events	0.15 ± 0.09	0.10 ± 0.07	0.05 ± 0.05
Half-Life Sensitivity (MDA $\times 10^{24}$ yrs)	3.28	4.09	3.09

Table 5.3: Summary table of the $0/2\nu\beta\beta$ detection efficiency, $2\nu\beta\beta$ number of expected events and the sensitivity estimates for the three magnetic fields.

Of the three magnetic field configurations, the no field scenario maintains the greatest detection efficiency after applying the two electron cut flow outlined in section 4.4.2. Additionally, as a result of the high energy region of interest, the two neutrino detection efficiency is suppressed and accordingly the background contribution is extremely small. When considering the ideal detector scenario, the highest sensitivity is achieved for no field as a result of the superior 0.0790 detection efficiency. The Poissonian approximations of the sensitivity are imprecise for low background statistics, nonetheless, when taking into account the additional background sources, the precision should improve. Although the idealistic detector assumes zero non DBD backgrounds, the current demonstrator module has non-zero background contributions from all different parts of the detector. To measure the sensitivity inclusive of the other backgrounds, the same procedure carried out to determine the $2\nu\beta\beta$ background count will be used for the remaining reducible backgrounds.

Chapter 6

Estimation of Backgrounds for SuperNEMO

The MDA method for estimating the detector sensitivity to the neutrinoless double beta decay half-life introduced in Chapter 4.4.2 represents the figure of merit (FOM) for this work and this figure of merit is used to compare the three magnetic field configurations. In order to maximise this sensitivity, the background contamination should be reduced or eliminated without significantly suppressing the signal detection efficiency. The sensitivity can also be improved with an increased exposure (Activity $\times$ Time), usually involving an increase in the source mass and run time of the experiment. For the SuperNEMO demonstrator, the initial run time is expected to be around 2.5 years, with a ^{82}Se source foil mass of 6.1 kg [45], therefore the MDA figures presented in this work are normalised to an exposure of 15.25 kg yrs.

This chapter is devoted to identifying the different sources of backgrounds as well as concluding how they materialise within the different parts of the detector. The 2e topology cuts discussed in chapter 5 are applied to the non-$2\nu\beta\beta$ backgrounds in order to determine the number of double beta candidate events that originate from background decays. Additionally, the simulated data will be used to predict how background decays mimic double beta candidate events. For the three magnetic fields, the contribution of the different backgrounds in the ^{82}Se region of interest will be calculated and the most significant backgrounds will be identified. To estimate the different background contributions, they will first be divided by their location. As stated in chapter 3, the three background locations are internal, radon-related and external, which will first be examined separately and combined to give the total background contamination for each magnetic field configuration.

In chapter 5, the sensitivity of the best case scenario detector, with zero non double beta decaying backgrounds, was investigated and this best case scenario will be expanded in this chapter to investigate the more realistic scenario, which includes the remaining background contributions. Determining the background contributions will allow for the final detector sensitivity estimates to be measured in chapter 7 for the three magnetic fields.

6.1 DBD Mimicking Mechanisms

6.1.1 Internal Background

Internal backgrounds were defined in section 3.3 as those background which originate within the confines of the source foil. As mentioned, the most substantial backgrounds found within the source foil are ^{208}Tl and ^{214}Bi, from the decay chains of ^{232}Th and ^{238}U shown in figures 3.9 and 3.10 respectively. The final source of internal backgrounds is the two neutrino double beta decay of the same isotope, discussed in chapter 5. Both the naturally occurring backgrounds, ^{208}Tl and ^{214}Bi, undergo beta decay within the source foil emitting an electron and usually at least one photon (^{214}Bi beta decays via a sole electron 19.1% of the time). The various photon energies are described in the decay schemes illustrated in Figures 6.1 and 6.2 below.

The interaction of the beta decay progeny shown in figures 6.1 and 6.2 with the source foil is what brings about events in the 2e channel and the mechanisms producing the 2e events are illustrated in figure 6.3. The first double beta mimicking mechanism is Møller scattering, which is a low angle electron-electron scattering where two electrons exchange a virtual photon transferring momentum between the two electrons. The beta electron emitted during the decay scatters an electron found within the dense source foil, resulting in the emission of two coincident electrons from the source foil, usually with a low opening angle as a result of the low momentum transfer.

Compton scattering is the scattering of gamma radiation by a charged particle, transferring momentum from the photon to the electron and ejecting the electron if the momentum transfer is sufficiently high. During beta decay, both ^{208}Tl and ^{214}Bi radiate photons of various energies (figures 6.1 and 6.2) which can initiate Compton scattering within the foil. The final mechanism for generating pseudo double beta events from internal backgrounds is internal conversion. Following the initial beta decay, the decaying isotope may reach an excited intermittent state during which it releases a photon for the purpose of de-excitation. Certain isotopes are able to de-excite via internal conversion, with an electron from one the inner shells of the atom ejected from the unstable atom. The internal conversion electron can provide the second electron for the 2e topology and although there is a de-excitation, it occurs over the time frame of a few nanoseconds producing two coincident electrons. The electron energy is equivalent to the gamma energy minus the binding energy of the atomic electron.

Although the increased density of the source foil amplifies the rate of electronic interactions, the foil also inhibits the charged particles from exiting, trapping them within the source foil or causing them to lose energy prior to emission. For this reason the source was processed into long thin sheets (0.3 mm foils [44]) with the intention of minimising the energy loss for electrons prior to emission.

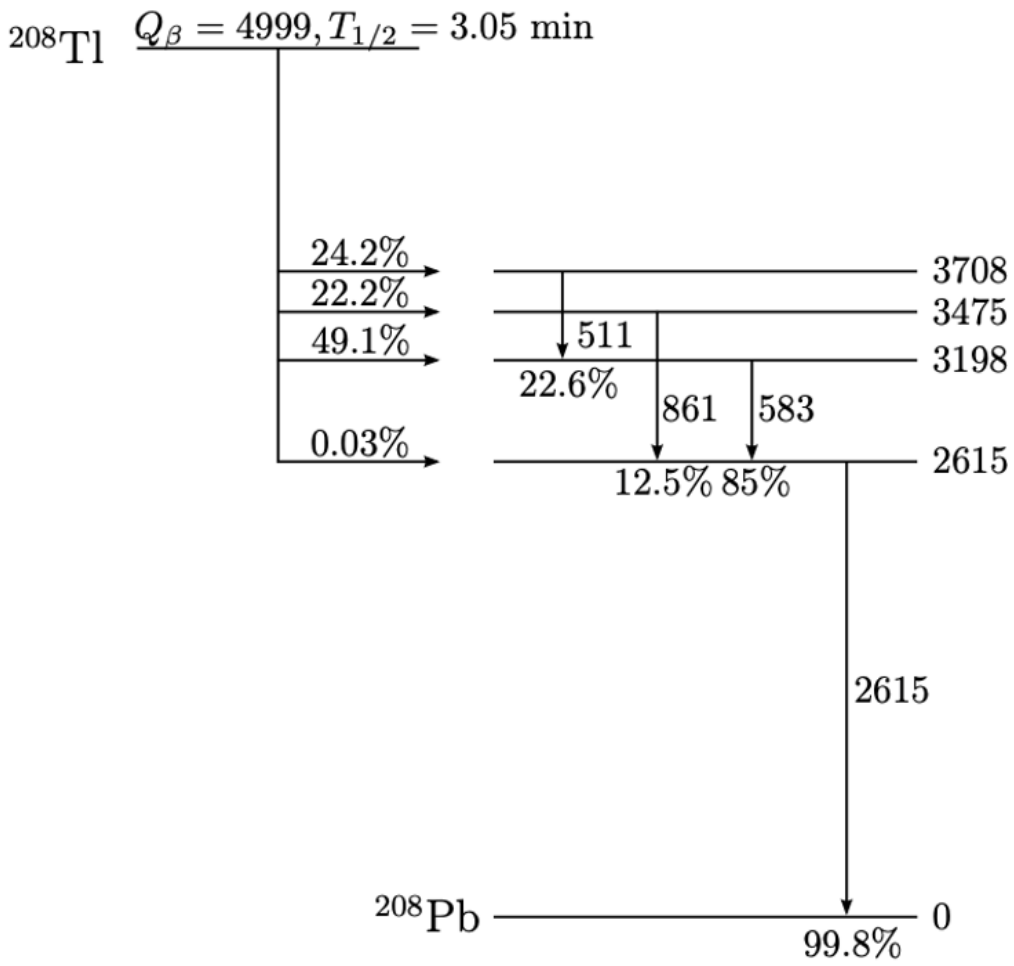

Figure 6.1: Simplified decay scheme for ^{208}Tl undergoing beta decay into ^{208}Pb, illustrating the most common transition lines, with the energies in keV [7].

6.1.2 Radon Backgrounds

Radon is a highly diffusive gas and readily enters the tracker volume via emanation from detector components or during construction. ^{222}Rn has a lifetime of roughly 3.8 days, allowing plentiful time for the gas to diffuse into the detector and undergo various decays into ^{214}Bi which is deposited on the surface of the source foil and tracker wires (figure 3.10) as explained in section 3.3. The decay of ^{222}Rn (discussed in section 4.2.3), culminates in the emission of an beta electron from ^{214}Bi decaying into ^{214}Po and a subsequent delayed alpha from the decay of ^{214}Po to ^{210}Pb.

The mechanisms for generating double beta candidate events from radon backgrounds are similar to those observed for internal backgrounds (shown in figure 6.3), with scattering being the dominant process. As the different Radon backgrounds originate in different parts of the detector, their

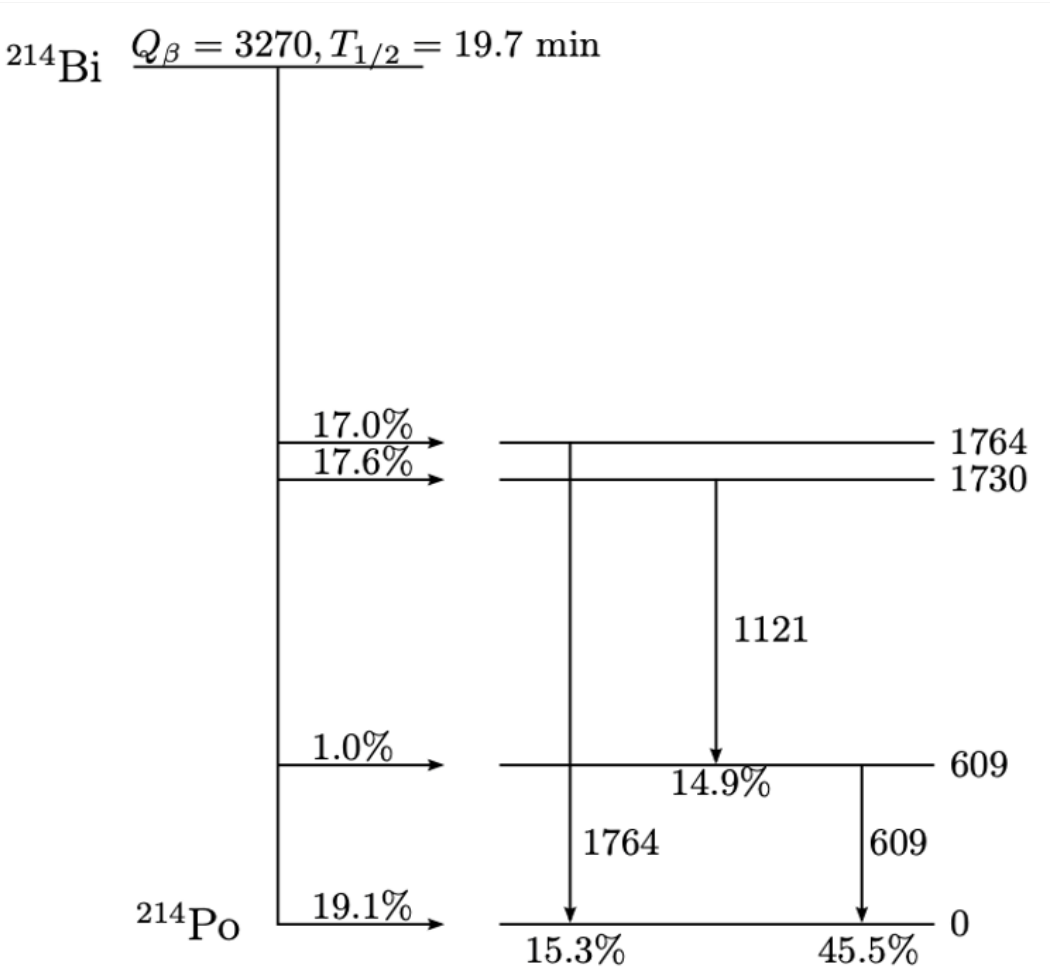

Figure 6.2: Simplified decay scheme for ^{214}Bi undergoing beta decay into ^{214}Po, illustrating the most common transition lines, with the energies in keV [7].

relative survival probabilities (detection efficiency ϵ for the backgrounds) will significantly differ. For example, radon backgrounds on the surface of the source foil will have an increased likelihood to be extrapolated back to source foil compared to simulations on the outer wires of the tracker volume, improving the survival probability on the surface of the source foil. Additionally, the high density of the source foil increases the cross section for both photonic and electronic interactions, increasing the rate at which internal backgrounds generate additional electrons. For ^{214}Bi the emitted alpha particle may not escape the source foil (for internal simulations) or may be missed entirely, resulting in a pure two electron event if one of the mechanisms in 6.3 results in the emission of two electrons from the decay vertex.

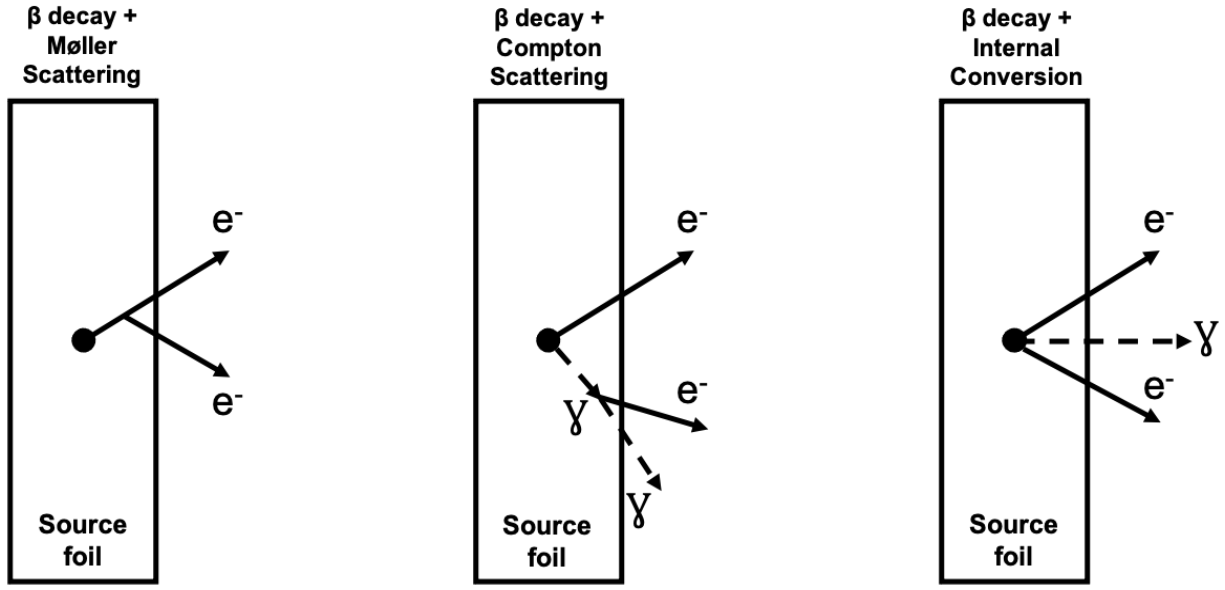

Figure 6.3: Illustrations of the dominant mechanisms, through which beta decaying internal backgrounds mimic double beta candidate events.

6.1.3 External Backgrounds

External backgrounds are defined as any non-radon backgrounds originating outside of the source foil. The majority of external backgrounds come about as a result of decays within the detector components, radioactive decays in the rocks surrounding the laboratory and neutron capture. External backgrounds materialise in a variety of decay channels including 1eNγ, however it is possible for external backgrounds to bring about double beta like decays reconstructed from the source foil.

An array of mechanisms can result in the production of double beta candidate events from external backgrounds which primarily generate pseudo double beta decays by way of photonic interactions with the dense source foil and other detector components. Pair production and Compton scattering from external photons provide the two principal mechanisms by which external backgrounds contribute towards the two electron channel, however the interaction of photons with matter is heavily dependent upon the photon energy as shown in figure 6.4. At higher energies, above 1 MeV, pair production and Compton scattering dominate. Pair production requires a photon of energy greater than 1.022 MeV, which is the minimum energy required to create two electrons

For external backgrounds, various mechanisms can produce two electron topologies and more often involve photonic interactions (figure 6.5). Multi energy photons from external decays first interact with the source foil, producing an electron positron pair (Figure 6.5 left) or a single Compton electron. The pair produced positron can be misconstrued as an electron, creating a two electron event. The Compton electron can Møller scatter to eject a second electron from the source foil (Figure 6.5 centre), or the incident photon can Compton scatter twice to produce two coincident

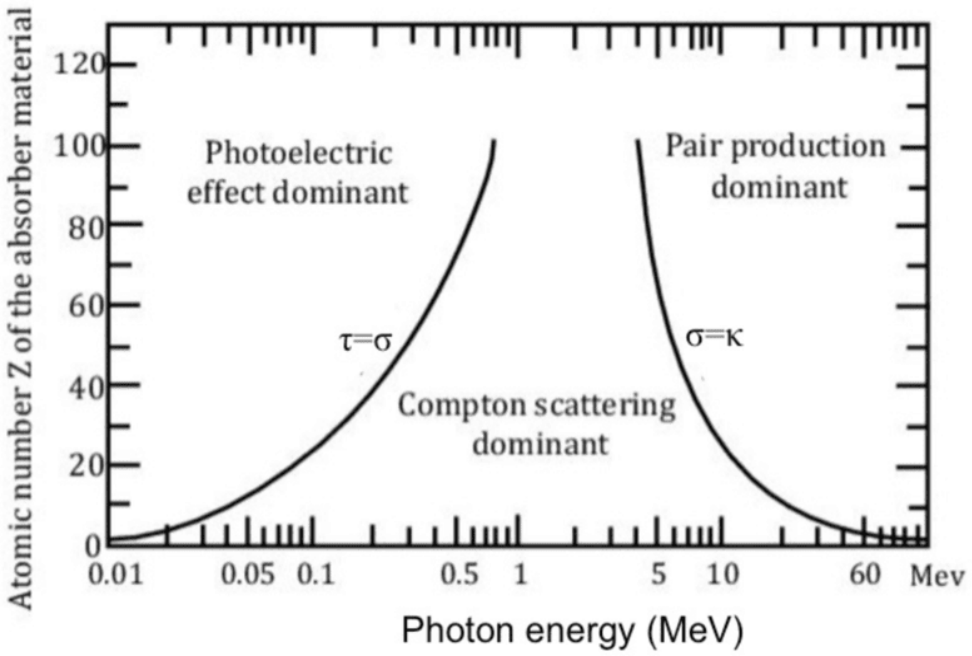

Figure 6.4: Cross section for photon interactions at various energies. The three principal interaction modes are shown as a function of the photon energy and atomic number of the interacting atom [47].

electrons (Figure 6.5 right). As mentioned, pair production requires a photon with a minimum energy of 1.022 MeV, which both ^{208}Tl and ^{214}Bi beta decays produce during their respective beta decays, as shown by the decay schemes in figures 6.1 and 6.2. ^{208}Tl in particular, produces a high energy 2.615 MeV photon, close to the ^{82}Se ROI, at a rate of 99.8%. The electron positron pair emitted from the source foil, can be misconstrued as a two electron event if the positron is labelled as an electron, which, as mentioned, frequently occurs for the no field scenario. At lower energies, the likelihood of Compton scattering and the photoelectric effect increases, although from the decay schemes shown in figures 6.1 and 6.2, Compton scattering and pair production are the likely processes associated with externally induced double beta candidate events.

Of all the potential external background sources, including the detector components, surrounding rocks and shielding it is important to note, only backgrounds on the detector wall PMTs were investigated. Primarily this is a consequence of the high ^{82}Se decay energy of 3 MeV, removing the majority of external backgrounds which can be found at lower energies. Although the decay energies of ^{208}Tl and ^{214}Bi are 5 and 3.3 MeV respectively, only gammas can penetrate the detector from external contamination and so only the high energy gamma progeny from these decays can interact within the detector to generate double beta candidate events.

In addition to the contributions from external ^{208}Tl and ^{214}Bi, ^{40}K is another external background as mentioned in chapter 6. ^{40}K can undergo both beta decay and electron capture resulting in the

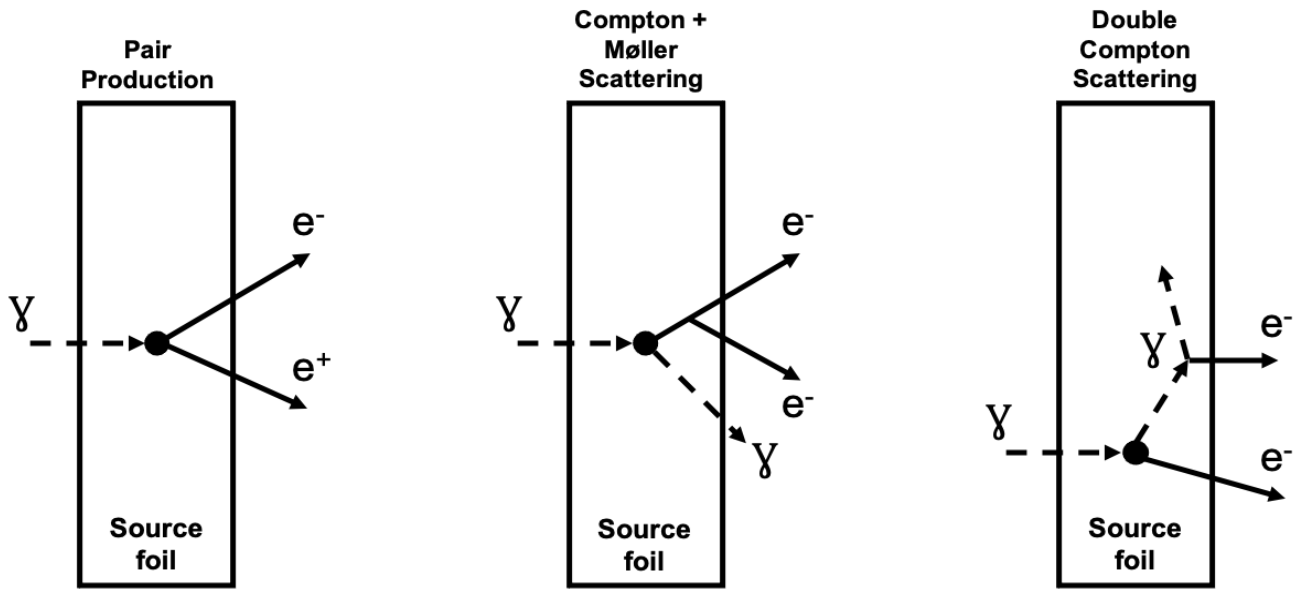

Figure 6.5: Illustrations of the dominant mechanisms, through which external backgrounds interacting with the source foil mimic double beta candidate events.

emission of a single electron or an electron followed by a photon after electron capture. ^{40}K is the most common isotope in the PMT glass, with an activity many times greater than that of ^{208}Tl and ^{214}Bi. Nonetheless, the decay energy of ^{40}K is significantly lower than both ^{208}Tl and ^{214}Bi, at approximately 1.4 MeV, reducing the rate at which ^{40}K decays mimic double beta candidate events in the high energy ROI. The final source of external backgrounds for the SuperNEMO demonstrator is thermalised neutrons, which when captured can result in the emission of gammas with energies ranging from 3-15 MeV. Neutron backgrounds have not been investigated in this work, however further reading on the subject can be found in [48].

6.2 Background Activities

The methods used to measure the background activities were highlighted in section 3.3, including the use of the High Purity Germanium (HPGe) and BiPo detectors. The table of activities for all simulated internal, radon and external backgrounds is given in table 6.1, with the associated number of decays over nominal exposure (6.1 kg $\times$ 2.5 years = 16.25 kg yrs). The internal background activities within the source foil were measured throughout the volume of the detector, using the HPGe and BiPo detectors, with the average contamination noted. For ^{208}Tl and ^{214}Bi, the activity is given as a maximum limit from a BiPo measurement, with a 90% confidence limit. The target activity of the internal backgrounds is 20μBq/Kg for ^{208}Tl and 100μBq/Kg for ^{214}Bi.

Radon in the tracker provides the contamination level for ^{214}Bi on both the surface of the source foil as well as the tracker wires. The contamination is scaled by the area of the different background sources such as the surface of the source foil or tracker wires. Approximately 7.8% of the radon contamination in the tracker deposits onto the surface of the tracker wires and the remaining 92.2% on the source foil surface. The division of activity is based on the width of the tracker-source air gap and the width of the tracker [49]. As mentioned earlier in section 3.3, the radon activity is given as a function of the flushing rate, which is expected to be 1m^3/h. The activity of ^{208}Tl and ^{214}Bi inside of the tracker wires is a consequence of the prior contamination of the detector materials and was directly measured. External background activities on the 8" PMTs were determined by directly measuring the activity of the PMT glass and insulators using crushed PMTs. For the 5" PMTs, the activities were taken from previous NEMO-3 studies as they were recycled from the experiment [50].

Isotope	Location	Activity mBq	No of Decays Over Nominal Exposure
^{208}Tl	Source Foil Bulk	0.55 *	43,000
^{214}Bi	Source Foil Bulk	4.94 *	389,500
^{208}Tl	Tracker Wire Bulk	0.24 ± 0.05	18,900
^{214}Bi	Source Foil Surface (Rn)	0.33 ± 0.04	26,000
^{214}Bi	Tracker Wire Bulk	0.49 ± 0.10	38,600
^{214}Bi	Tracker Wire Surface (Rn)	3.92 ± 0.44	309,000
		Activity Bq	
^{40}K	8" Main Wall PMT Glass Bulb	230 ± 23	18,133,200,000
^{40}K	5" Main Wall PMT Glass Bulb	23 ± 2.3	1,813,320,000
^{40}K	X Wall PMT Glass Bulb	37 ± 3.7	2,917,080,000
^{40}K	G Veto Wall PMT Glass Bulb	19 ± 1.9	1,497,960,000
^{208}Tl	8" Main Wall PMT Glass Bulb	41 ± 4.1	3,232,440,000
^{208}Tl	5" Main Wall PMT Glass Bulb	1 ± 0.1	78,840,000
^{208}Tl	X Wall PMT Glass Bulb	2 ± 0.2	157,680,000
^{208}Tl	G Veto Wall PMT Glass Bulb	1 ± 0.1	78,840,000
^{214}Bi	8" Main Wall PMT Glass Bulb	136 ± 13.6	10,722,240,000
^{214}Bi	5" Main Wall PMT Glass Bulb	18 ± 1.8	1,419,120,000
^{214}Bi	X Wall PMT Glass Bulb	30 ± 3.0	2,365,200,000
^{214}Bi	G Veto Wall PMT Glass Bulb	15 ± 1.5	1,182,600,000

Table 6.1: Total activities for all internal, radon and external backgrounds simulated. The activity (mBq) for each isotope is given alongside the expected exposure of 6.25 kg over 2.5 years of running time. For internal ^{208}Tl and ^{214}Bi the activities are provided as an upper limit. For the external backgrounds the listed activities are given in Bq [49],[50].

6.3 Background Simulations

6.3.1 Table of Simulations

All simulations were generated using Falaise 4.0.0 detailed in chapter 4 and were uniformly distributed throughout the selected location. Simulated events were then reconstructed using the official Falaise 4.0.0 reconstruction configuration. For each background simulated at a vertex location, the number of simulations were generated for each of the three magnetic field configurations. The total number of simulated events, at the corresponding locations in the detector, are shown in table 6.2.

Vertex Location	^{40}K	^{208}Tl	^{214}Bi	$2\nu\beta\beta$	Number of Simulated Events in Location
Source Foil Bulk		✓	✓	✓	10^8
Source Foil Surface (Rn)		✓	✓		10^8
Tracker Wire Bulk		✓	✓		10^8
Tracker Wire Surface (Rn)		✓	✓		10^8
8" Main Wall PMTs*	✓	✓	✓		$1.1 \times 10^{10\dagger}$
5" Main Wall PMTs	✓	✓	✓		10^9
X Wall PMTs	✓	✓	✓		10^9
G Veto Wall PMTs	✓	✓	✓		10^9

Table 6.2: Simulation vertex locations and the number isotope decay events simulated at those locations.

† For the external ^{208}Tl simulations, 15 billion events were simulated for no field and 11 Billion events for the remaining two magnetic fields.

6.4 Background Results

As mentioned in section 3.3, the detection efficiency shown in equation 4.9, is referred to as the survival probability, for background simulations. The survival probability is equivalent to equation 4.9, in that it takes the ratio of events that survived the cuts compared to the total number of simulations. The cuts used for determining the signal detection efficiency or background survival probability were motivated and discussed Section 5.2. The order of the cut flow and the individual cuts are unchanged between the signal and background and just as $2\nu\beta\beta$ from Table 5.2, the number of expected events will be given alongside the final probability for all three magnetic field configurations. The most significant background cut flow tables, internal ^{208}Tl, internal ^{214}Bi and external ^{208}Tl, will be briefly discussed with reference to the motivation described in section 5.3.

6.4.1 Internal Backgrounds

As defined in Section 6.1, internal backgrounds are those which originate from within the bulk of the source foil. For SuperNEMO, this includes the ^{208}Tl and ^{214}Bi source foil contaminations as well as the $2\nu\beta\beta$ contribution discussed in Chapter 5. For ^{208}Tl and ^{214}Bi, the number of simulations generated is shown in Table 6.2 and the concurrent survival probabilities/number of expected events are illustrated in Tables 6.3 and 6.4 respectively. The first cut flow table is Table 6.3, which illustrates the cut flow, final survival probability and the corresponding number of expected events for internal ^{208}Tl. From Table 6.3, the final survival probability and consequently the magnetic field with the greatest number of expected events is the no field scenario, followed by the uniform and realistic fields respectively. The most significant reason for this is the impact of the charge cut on reducing the number of remaining events for the uniform and realistic fields.

Prior to the associated tracks cut, the two hits/clusters/tracks cuts removes a large number of events as a consequence of the decay emitting only one charged particle. Additionally, the uniform field has the greatest detection efficiency prior to the associated track, as the increased track radius of curvature increases the number of reconstructed tracks. The associated track cut is useful for removing events with gammas as they are reconstructed as unassociated tracks. For ^{208}Tl which decays with the emission of an electron with at a minimum, one photon, track fitting errors increase the number of tracks from one to two and the photon provides a second calorimeter hit. After applying the remaining cuts however, the difference in detection efficiency between the uniform field and the other two fields is reduced as these events are identified and removed by the associated tracks and subsequent cuts.

Cut Descriptions	Concurrent Survival Probability		
	Uniform Field	No Field	Realistic Field
Only two calorimeter hits above 50keV, at least one >150keV	0.2387	0.2342	0.2349
Two tracker clusters with 3 or more cells	0.0311	0.0239	0.0253
Two reconstructed tracks	0.0309	0.0238	0.0251
Remove events with multiple hits to the same calorimeter	0.0134	0.0119	0.0122
Each track associated to a calorimeter	0.0017	0.0024	0.0022
Two vertices on the source foil	0.0016	0.0023	0.0022
Vertex ΔR <1cm and ΔZ <3cm (separation between vertices)	0.0008	0.0012	0.0011
Internal Probability >1% and External Probability <4%	0.0007	0.0010	0.0009
Delayed Alpha Hits (no hits allowed after 13 μs)	0.0007	0.0010	0.0009
Remove Positrons (unavailable for no field)	0.0006	-	0.0006
Energy Cut (between 2.8 and 3.2 MeV)	1907×10^{-8}	2527×10^{-8}	1637×10^{-8}
Number of Expected Events	0.82 ± 0.02 (stat)	1.09 ± 0.02 (stat)	0.69 ± 0.02 (stat)

Table 6.3: Internal ^{208}Tl cut flow and number of expected events for the three magnetic field configurations. Each row lists a short description of the cut as well as the concurrent survival probability. The number of expected events is normalised to the exposure of 15.25 kg yrs (6.1 $\times$ 2.5 years).

Cut Descriptions	Concurrent Survival Probability		
	Uniform Field	No Field	Realistic Field
Only two calorimeter hits above 50keV, at least one >150keV	0.2375	0.2392	0.2389
Two tracker clusters with 3 or more cells	0.0315	0.0261	0.0271
Two reconstructed tracks	0.0303	0.0251	0.0260
Remove events with multiple hits to the same calorimeter	0.0157	0.0148	0.0150
Each track associated to a calorimeter	0.0032	0.0042	0.0040
Two vertices on the source foil	0.0028	0.0036	0.0035
Vertex ΔR <1cm and ΔZ <3cm (separation between vertices)	0.0013	0.0017	0.0017
Internal Probability >1% and External Probability <4%	0.0012	0.0016	0.0015
Delayed Alpha Hits (no hits allowed after 13 μs)	0.0012	0.0016	0.0015
Remove Positrons (unavailable for no field)	0.0011	-	0.0010
Energy Cut (between 2.8 and 3.2 MeV)	362×10^{-8}	477×10^{-8}	315×10^{-8}
Number of Expected Events	1.41 ± 0.07 (stat)	1.86 ± 0.09 (stat)	1.23 ± 0.07 (stat)

Table 6.4: Internal ^{214}Bi cut flow and number of expected events for the three magnetic field configurations. Each row lists a short description of the cut as well as the concurrent survival probability. The number of expected events is normalised to the exposure of 15.25 kg yrs (6.1 × 2.5 years).

The survival probability of ^{214}Bi is lesser than ^{208}Tl, however, as a result of the greater ^{214}Bi activity in the source foil (table 6.1), the number of expected backgrounds from ^{214}Bi is higher. On average, the detection efficiency of internal ^{208}Tl is around 5× greater compared to ^{214}Bi, but after normalising to the activity, the number of expected events is roughly 1.7× greater for ^{214}Bi. From figure 6.6, the reduced detection efficiency of ^{214}Bi can be explained from tail of the energy spectrum, which falls to zero within the region of interest, akin to $2\nu\beta\beta$. For internal ^{208}Tl, the energy spectrum extends well beyond the ^{82}Se ROI, increasing the total number of two electron events found within the region.

The results for $2\nu\beta\beta$ were discussed in chapter 5 which completes the internal background

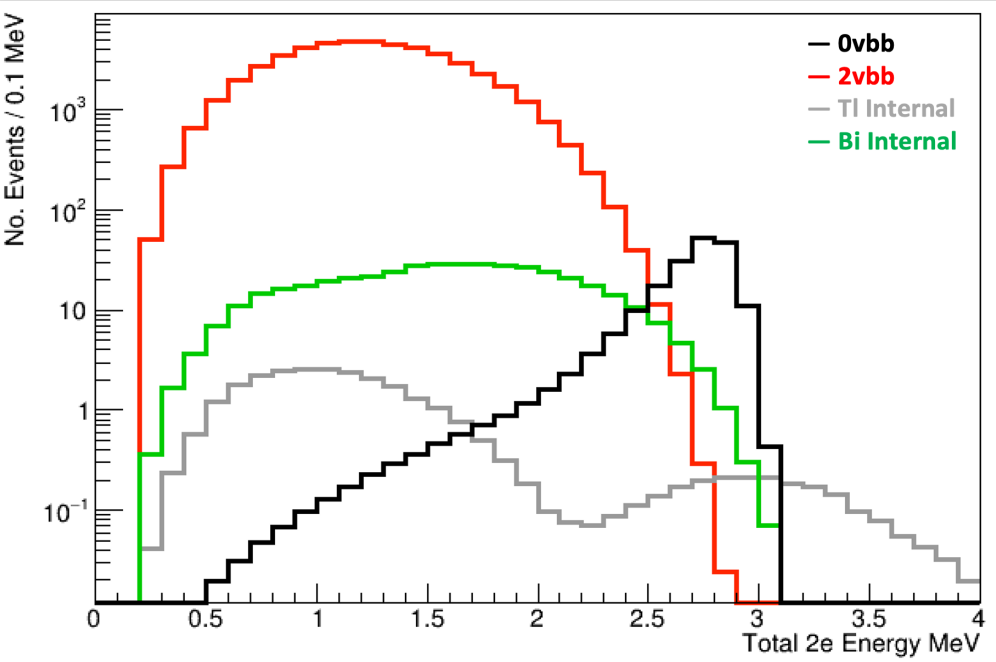

Figure 6.6: Energy spectra for $0\nu\beta\beta$ and the three internal backgrounds for events with a 2e topology for the uniform field scenario. The internal backgrounds include $2\nu\beta\beta$, ^{208}Tl and ^{214}Bi. The background spectra are normalised to exposure and the signal to the MDA half-life sensitivity.

contributions. The number of expected events from $2\nu\beta\beta$ is shown in table 6.5, alongside the results from internal ^{208}Tl and ^{214}Bi.

Of the three backgrounds, ^{214}Bi has the greatest number of expected events followed by ^{208}Tl and $2\nu\beta\beta$. Overall, the internal background contamination is highest for no field, followed by the uniform field and realistic field respectively.

Internal Background	Number of Expected 2e Candidate Events Uniform Field	No Field	Realistic Field
$2\nu\beta\beta$	0.15 ± 0.09	0.10 ± 0.07	0.05 ± 0.05
^{208}Tl	0.82 ± 0.02	1.09 ± 0.02	0.69 ± 0.02
^{214}Bi	1.41 ± 0.07	1.86 ± 0.09	1.23 ± 0.07
Total	2.38 ± 0.12	3.05 ± 0.11	1.97 ± 0.09

Table 6.5: Number of expected 2e candidate events in the ^{82}Se ROI for all internal backgrounds for the no field scenario. The error given for each value is the statistical error only.

6.4.2 Radon Backgrounds

Radon backgrounds contribute significantly fewer expected events to the ^{82}Se ROI compared to those from the internal sources. For ^{208}Tl and ^{214}Bi in the bulk of the tracker wires, both the detection efficiency and activity are lower than the corresponding internal background, resulting in the ^{208}Tl/^{214}Bi wire bulk contribution being roughly 1% of the total internal ^{208}Tl/^{214}Bi expected events. The activity of ^{208}Tl and ^{214}Bi in the tracker wire bulk is attributed to radon during reconstruction as a consequence of the location and energy profile of the backgrounds being similar to ^{214}Bi on the surface of the tracker wires, which is deposited by ^{222}Rn (Section 3.3). Moreover, thoron, which is radon from the ^{232}Th decay chain, has a half-life of only 55.6 seconds and cannot easily emanate into the detector and deposit ^{208}Tl onto the surface of the source foil and tracker wires. Therefore ^{208}Tl is only found within the bulk of the tracker wires.

Isotope	Location	Survival Probability ($\times 10^{-8}$) & Number of Expected 2e Candidate Events		
		Uniform Field	No Field	Realistic Field
^{208}Tl	Tracker Wire Bulk	30 0.006 ± 0.001 (stat) ± 0.002 (syst)	53 0.010 ± 0.001 (stat) ± 0.004 (syst)	34 0.006 ± 0.001 (stat) ± 0.002 (syst)
^{214}Bi	Tracker Wire Bulk	9 0.003 ± 0.001 (stat) ± 0.001 (syst)	9 0.003 ± 0.001 (stat) ± 0.001 (syst)	6 0.002 ± 0.001 (stat) ± 0.001 (syst)
^{214}Bi	Source Foil Surface	314 0.08 ± 0.004 (stat) ± 0.009 (syst)	373 0.10 ± 0.005 (stat) ± 0.011 (syst)	247 0.06 ± 0.004 (stat) ± 0.007 (syst)
^{214}Bi	Tracker Wire Surface	6 0.019 ± 0.008 (stat) ± 0.002 (syst)	9 0.028 ± 0.009 (stat) ± 0.003 (syst)	6 0.019 ± 0.008 (stat) ± 0.002 (syst)

Table 6.6: Detection efficiency and number of expected events for all radon and tracker bulk ^{208}Tl simulations, for the three magnetic field configurations. The number of expected events is normalised to the exposure of 15.25 kg yrs (6.1 × 2.5 years).

For ^{214}Bi, there are two sources of radon backgrounds, including the surface of the source foil and tracker wires. The combined contribution from the three radon sources is dwarfed by internal ^{214}Bi, accounting for only 7% of the internal contribution. Primarily this is a consequence of the lower ^{214}Bi activity on the surface of the source foil and the low detection efficiency of the tracker wire simulations. The detection efficiency of ^{214}Bi on the source foil surface is similar to that observed with ^{214}Bi in the bulk of the source foil however, as the activity is an order of magnitude lower the number of expected events is similarly reduced. The detection efficiencies for ^{214}Bi on the surface and within the bulk of the tracker wires are significantly lower than that seen for ^{214}Bi on the source

foil surface because the event vertices are less likely to be reconstructed back to the foil.

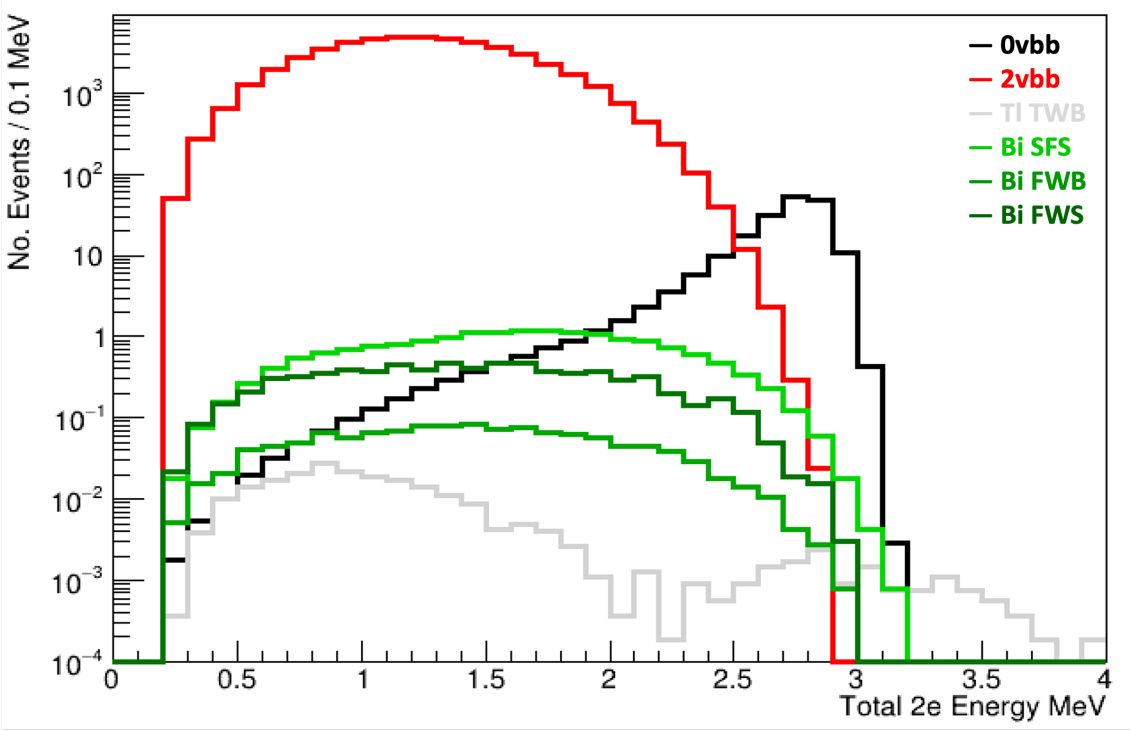

Figure 6.7: Energy spectra for $0\nu\beta\beta$, $2\nu\beta\beta$, the two radon backgrounds and ^{208}Tl/^{214}Bi in the tracker wire bulk (TWB), for events with a 2e topology. The radon backgrounds include ^{214}Bi on the source foil surface (SFS) and tracker wire surface (TWS). The background spectra are normalised to the exposure and the signal to the number of simulated events.

Like internal ^{214}Bi, the radon ^{214}Bi energy spectra curtail within the ^{82}Se ROI, reducing the detection efficiency compared to ^{208}Tl. Additionally, the energy profile for ^{214}Bi on the surface of the source foil is extremely similar to the internal ^{214}Bi spectra.

6.4.3 External Backgrounds

From the PMTs, the sole background contribution to the ^{82}ROI came from ^{208}Tl on the 8" Main wall PMTs. No Monte Carlo simulated events were found in the ROI for any of the other isotopes simulated in all of the external locations, including the 5" Main wall, X wall and Veto wall PMT glass bulbs. Backgrounds from the two rows of 5" Main wall PMTs, located at the top and bottom of the Main walls, are encumbered by their location, reducing the number of external backgrounds reaching the source foil. A similar but more severe impact is observed for the G Veto simulations with no double beta candidate events of any energy being generated. Although the X wall events are less suppressed by their location within the detector, the double beta candidate events have energies below the region of interest and lower survival probabilities.

As a result of the non-zero contribution from external ^{208}Tl on the 8" Main wall PMTs, an increased number of events were simulated (from the original 10^9) in order to reduce the statistical uncertainty on the simulated data. For no field, including the additional secondary particle simulations (Section 4.1.4), a total of 15 billion events were simulated, whereas for the uniform and realistic fields, 11 billion decays were simulated, with no secondary particle simulations.

Cut Descriptions	Concurrent Survival Probability		
	Uniform Field	No Field	Realistic Field
Only two calorimeter hits above 50keV, at least one >150keV	2.19×10^{-1}	2.19×10^{-1}	2.19×10^{-1}
Two tracker clusters with 3 or more cells	4.75×10^{-4}	4.71×10^{-4}	4.71×10^{-4}
Two reconstructed tracks	4.60×10^{-4}	4.68×10^{-4}	4.68×10^{-4}
Remove events with multiple hits to the same calorimeter	3.72×10^{-4}	3.92×10^{-4}	3.90×10^{-4}
Each track associated to a calorimeter	2.12×10^{-4}	2.37×10^{-4}	2.33×10^{-4}
Two vertices on the source foil	2.10×10^{-4}	2.33×10^{-4}	2.32×10^{-4}
Vertex ΔR <1cm and ΔZ <3cm (separation between vertices)	1.60×10^{-4}	1.81×10^{-4}	1.79×10^{-4}
Internal Probability >1% and External Probability <4%	3.87×10^{-7}	5.01×10^{-7}	4.89×10^{-7}
Delayed Alpha Hits (no hits allowed after 13 μs)	3.87×10^{-7}	5.01×10^{-7}	4.89×10^{-7}
Remove Positrons (unavailable for no field)	6.75×10^{-8}	-	1.30×10^{-7}
Energy Cut (between 2.8 and 3.2 MeV)	$\frac{2}{1.1\times10^{-10}}$	$\frac{110\dagger}{1.5\times10^{-10}}$	$\frac{10}{1.1\times10^{-10}}$
Number of Expected Events	0.58 ± 0.41 (stat) ± 0.06 (syst)	23.5 ± 2.24 (stat) ± 2.35 (syst)	2.91 ± 0.92 (stat) ± 0.29 (syst)

Table 6.7: Detection efficiency and number of expected events for external ^{208}Tl 8" Main Wall simulations, for the three magnetic field configurations. The number of expected events is normalised to the exposure of 15.25 kg yrs (6.1 × 2.5 years).

† The total number of simulated events for the no field scenario was 1.5×10^{10} and 1.1×10^{10} for the uniform and realistic field (Table 6.2).

Following simulation and normalization to both the exposure as well as the number of simulated events, the survival probability and total number of expected events for ^{208}Tl on the 8" Main wall PMT glass bulb is shown in Table 6.7. The number of expected events of 23.5 for no field represents almost 90% of the total backgrounds for the no field scenario. Although the detection efficiency is much lower for external ^{208}Tl, the much greater activity from external sources (Table 6.1) results in an increased number of expected backgrounds compared to other background sources. Similarly, for the realistic field, external ^{208}Tl is the largest background however it only represents approximately

60% of the total activity. For the uniform field external ^{208}Tl is the third largest background contribution behind internal ^{208}Tl and internal ^{214}Bi. The large contribution from external ^{208}Tl, particularly for no field and the realistic field requires further analysis in order to understand the origin of these events and create additional, targeted cuts for reducing this particular background. In the following chapter, the underlying mechanism producing double beta candidate events from the background decay will be discussed and used to rationalize the extra cuts and finally the impact of these cuts will be exhibited.

The energy spectra of the three isotopes simulated on the 8" Main wall PMTs is shown in Figure 6.8, with only the ^{208}Tl tail surpassing 2.8 MeV. The lower energy decays of ^{40}K and ^{214}Bi results in the potential double beta candidate events to be removed by the 2.8 - 3.2 MeV energy cut. Additionally, the low energy spectra shown in Figure 6.8 indicate no double beta candidate events would be found from simulating on the X and G Veto walls and so no events were simulated. The Main Wall represents the most probable external vertex location for inducing two electron events and so it is not expected for either external ^{40}K or ^{214}Bi to contribute to the ^{82}Se ROI.

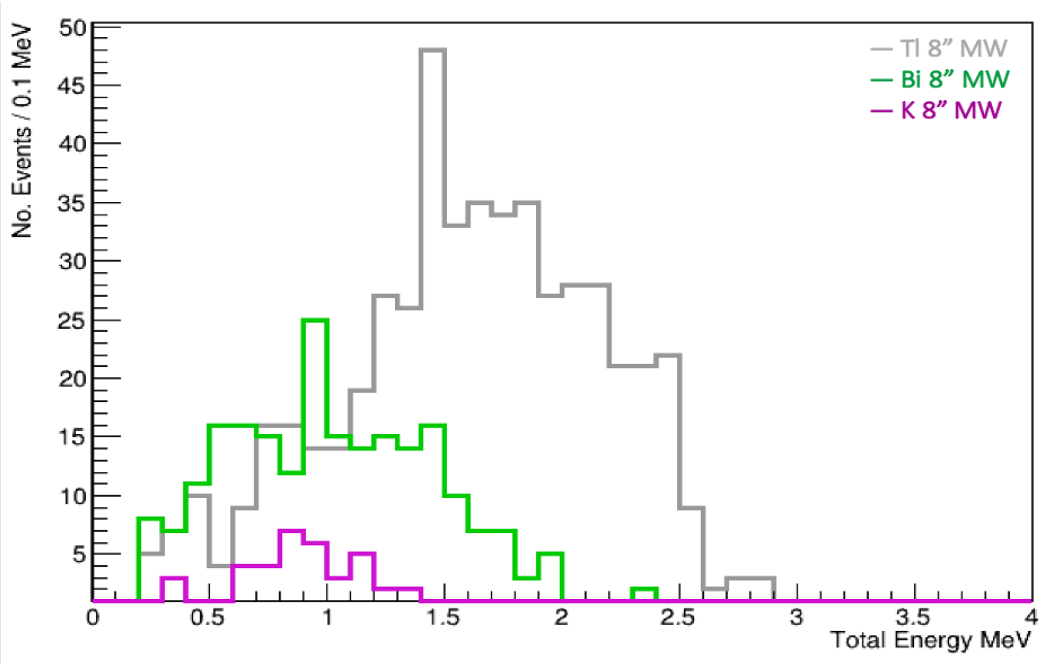

Figure 6.8: Energy spectra for all 8" Main Wall (MW) backgrounds with a 2e topology, including ^{208}Tl, ^{214}Bi and ^{40}K. For ^{214}Bi and ^{40}K, no events with a 2e topology were found in the ^{82}Se ROI. The energy spectra is normalised to the number of simulated events.

6.4.4 Total Background Contributions

	Number of Expected 2e Candidate Events		
Background	Uniform Field	No Field	Realistic Field
$2\nu\beta\beta$	0.15 ± 0.09	0.10 ± 0.07	0.05 ± 0.05
Internal ^{208}Tl	0.82 ± 0.02	1.09 ± 0.02	0.69 ± 0.02
Internal ^{214}Bi	1.41 ± 0.07	1.86 ± 0.09	1.23 ± 0.07
Radon ^{214}Bi	0.101 ± 0.01	0.125 ± 0.01	0.084 ± 0.01
Tracker Wire Bulk ^{208}Tl	0.006 ± 0.001	0.010 ± 0.001	0.006 ± 0.001
Tracker Wire Bulk ^{214}Bi	0.003 ± 0.001	0.003 ± 0.001	0.002 ± 0.001
*External ^{208}Tl 8" Main Wall PMTs	0.58 ± 0.41	23.5 ± 2.24	2.91 ± 0.92
Total Number of Expected Events	3.07 ± 0.43	26.69 ± 2.24	4.97 ± 0.92

Table 6.8: Number of expected 2e candidate events for all backgrounds in the ^{82}Se ROI with an exposure of 15.25 kg yrs (6.19 kg × 2.5 years), for the main background contributions. The total number of expected backgrounds for all three magnetic fields. Background errors shown are the statistical errors, with the systematic errors taken as 10% across all backgrounds.

Table 6.8 provides the total number of expected events for each isotope that contributes a non-zero amount to the ^{82}Se region of interest. Of the three magnetic field configurations, no field has the greatest number of expected backgrounds, roughly 5x greater then the realistic field and close to 9x the uniform field. The discrepancy between the three fields is largely a result of the contribution from external ^{208}Tl on the 8" Main Wall PMTs, shown in Figure 6.9, which contributes significantly more for the no field scenario. The increase in all backgrounds for no field is mostly a result of electron tracks being reconstructed with the 'wrong' sign. As the charge cut is not applied for the no field scenario these events are not removed, increasing the total background count. Furthermore, the increased contribution from external ^{208}Tl is a result of the higher activity of the external backgrounds as the detection efficiencies of the external backgrounds are generally much lower compared to the internal or radon simulations. By identifying the mechanism behind the external ^{208}Tl double beta candidate events, multi-variate analysis can be utilised to remove the large background contribution from external ^{208}Tl and will be discussed in Chapter 7.

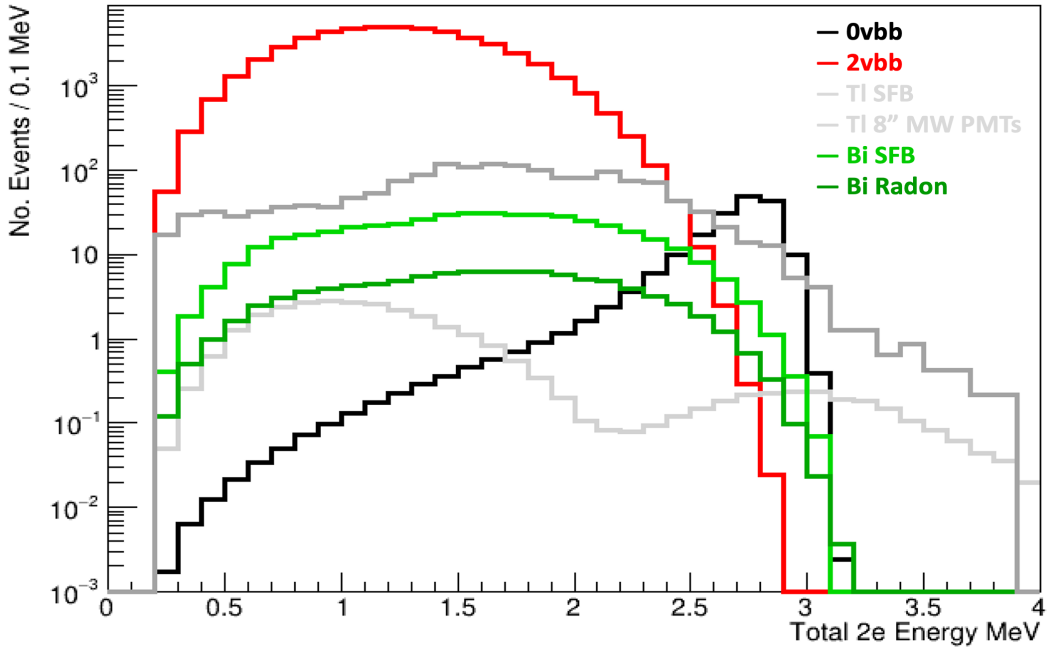

Figure 6.9: Energy spectra for all external ^{208}Tl backgrounds with a 2e topology, including, ^{208}Tl on the 8" Main Wall (MW) PMTs, 5" Main Wall (MW) PMTs, 5" X Wall (XW) PMTs and the 5" G Veto Wall (VW) PMTs. Only 8" Main Wall simulations resulted in events with a 2e topology in the ^{82}Se ROI. There are no events with a 2e topology for ^{208}Tl simulated on the G Veto PMTs. The energy spectra is normalised to the number of simulated events.

Chapter 7

Optimisation Of Background Suppression And Sensitivity Comparison Of SuperNEMO Magnetic Field Configurations

In chapter 6, it was shown that the most significant background contribution came from external ^{208}Tl on the 8" Main wall PMTs for the no field scenario. Additionally, of the three magnetic field configurations being investigated, the no field scenario had the highest background survival probability for reconstructing two electron events from all backgrounds, mostly as a result of the absence of a charge cut for events with charged particle tracks reconstructed with the 'wrong' sign. Consequently, the no field scenario had the greatest number of expected backgrounds, but also had the greatest signal detection efficiency.

In order to measure the performance of three magnetic field configurations, the sensitivity to ^{82}Se neutrinoless double beta decay is calculated for each magnetic field. The sensitivity provides the figure of merit (FOM) for this work and is used as the metric to determine which magnetic field gives the best FOM. Moreover, the FOM uses a simple counting experiment in a fixed energy region (Equation 4.19), to perform a comparative analysis of the three magnetic field configurations. This FOM is dependant upon multiple factors, including the $0\nu\beta\beta$ detection efficiency and number of expected backgrounds discussed in chapter 6 and in order to maximise the sensitivity, the $0\nu\beta\beta$ detection efficiency should be as large as possible whilst simultaneously suppressing the background count. The large background contribution from external ^{208}Tl on the 8" Main wall PMTs with no field suggests a background mechanism with the 'wrong' curvature is responsible for the events with 2e topologies. The underlying mechanism was investigated by simulating additional secondary particle simulations as discussed in section 4.1.4, and the additional data was used to infer the processes which result in the ROI events from ^{208}Tl on the 8" Main wall PMTs with no field. The identified mechanism provided motivation for additional optimisation cuts which were investigated for the three fields and used to primarily reduce the 8" Main Wall ^{208}Tl contamination, particularly for the no field scenario. The impact of the additional optimisation cuts on both the background contamination and signal efficiency will be presented. Finally, the current 2.8 - 3.2 MeV ROI will be optimised to minimise the background and maximise the signal efficiency and finally the sensitivities of the three magnetic field scenarios will be reported, using the Minimum Detectable Activity (MDA) method outlined in Section 4.5.1, with a view to determine which of the three magnetic field scenarios provides the greatest $0\nu\beta\beta$ sensitivity.

7.0.1 External Background Mechanism for DBD Candidates

In order to investigate the origin of the double beta candidate events from 8" Main wall ^{208}Tl decays, additional simulations were generated with access to GEANT level information for secondary particles. As mentioned in section 4.1.4, the additional GEANT level information provides data for the properties of the secondary particles that are produced when the primary decay particles interact with the detector. Using this information, the underlying 2e mechanism is presented below.

The initial beta decay of ^{208}Tl on the PMT glass bulbs results in the emission of an electron, as well as a number of gammas dictated by the decay scheme in figure 6.1. However, after generating additional simulations with true secondary particle information, the two reconstructed electron tracks were shown to be brought about by a single secondary electron, as illustrated in figure 7.1. A secondary electron is defined as an electron generated by a photon interacting with the surface of a scintillator block as displayed in figure 7.1.

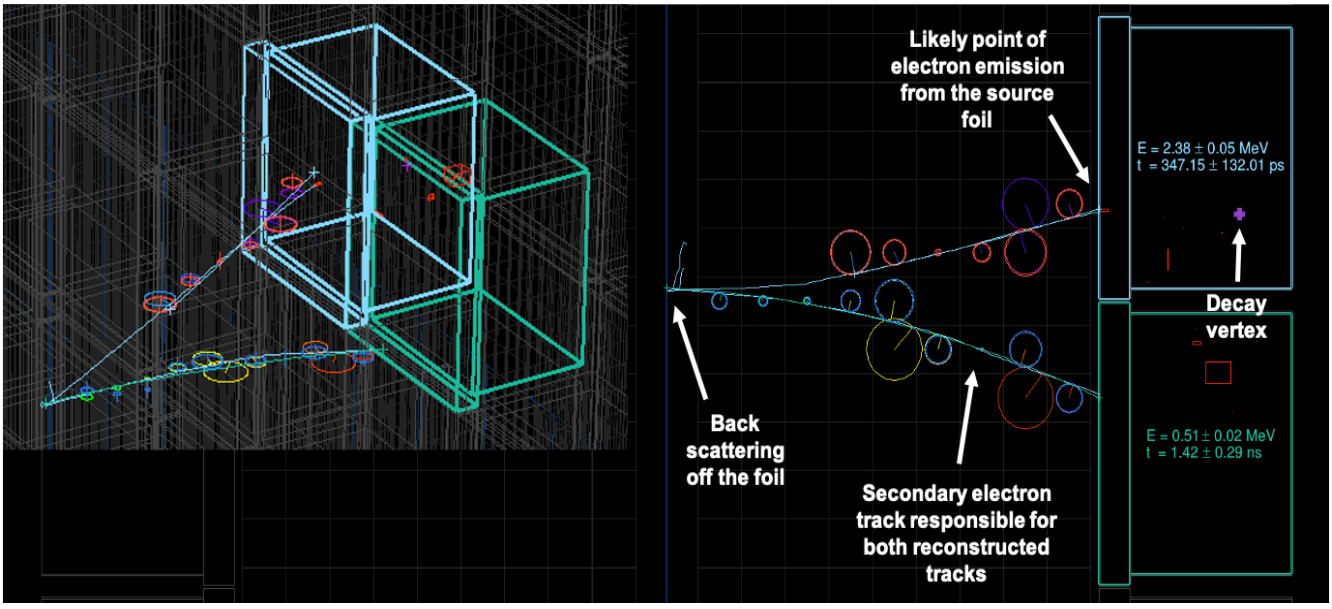

Figure 7.1: Event display illustrating the how an external ^{208}Tl decay on the 8" Main wall PMTs produces a double beta candidate event, which occurs via the emission of a secondary electron from the surface of the scintillator.

The secondary electron generates two reconstructed tracks by propagating from the surface of the scintillator, to the source foil and backscattering off the foil before finally coming to rest in a second calorimeter close to the initial decay, as shown in figure 7.1. This results in two reconstructed charged particles that appear to have a shared vertex on the foil.

The electron is most likely to be emitted from the surface of the scintillator via Compton or low energy electronic scattering. The emitted secondary electron is of low energy, but additional energy

is provided by the primary photons, including the 2.6 MeV photon produced in almost all ^{208}Tl decays as shown in figure 6.1. This additional energy is registered by either the initial or adjacent PMT, raising the total energy of the event into the ^{82}Se ROI. Two calorimeter hits are registered, one in the original decay calorimeter and a second in a neighbouring OM from one of the primary ^{208}Tl decay photons. Falaise only registers the timing for the first hit to a calorimeter therefore the two hits are measured as coincident hits with the timing determined by the time taken for the primary decay progeny to deposit energy within the two PMTs. The time taken for the secondary electron to backscatter off the foil and then strike the adjacent PMT is not taken into account when measuring the time separation of the two calorimeter hits, allowing the event to pass the timing cuts (Section 4.3). This combination of factors allows for external ^{208}Tl events to pass all of the current cuts and contribute significantly towards the total background count, particularly for no field.

Therefore, in order to successfully generate a double beta candidate event from external ^{208}Tl, the incident secondary electron must interact head on with the source foil so that the electron returns to the locale of the initial decay. For simulations on the X and G Veto wall PMTs, it is impossible for secondary electrons to strike the foil at an angle that can backscatter towards the initial vertex location because the X and G Veto walls do not face the exposed side of the source foil.

7.1 Optimisation Of Background Suppression

As a result of the excessive number of expected events for external ^{208}Tl on the 8" Main wall PMTs, further cuts are necessary for reducing the prevalence of the background. From chapter 6, external ^{208}Tl was shown to represent over 90% of the total background for the no field scenario and increased the total background for no field to over 5 and 9 times the background count observed for the realistic and uniform field respectively. Additionally, the events have low opening angles and calorimeter hit time separations as explained in section 7.0.1. To explicitly target the external ^{208}Tl background, three additional cuts were investigated: Setting a minimum opening angle for the 2e topology, Removing events with adjacent calorimeter hits and Removing events in specific energies regions based on the decay scheme of ^{208}Tl.

7.1.1 Minimum Opening Angle

As mentioned in chapter 6, pseudo double beta decays from background simulations, often results in 2e events with low opening angles. As shown in figure 5.3, $0\nu\beta\beta$ follows a 1 - cosθ angular distribution, modified by the detector response, with the majority of events found at large angles. However, cutting on smaller angles does still remove a significant number of signal events so it pertinent to measure if there is an overall improvement in sensitivity when cutting out double beta candidate events with small angles. From the angular distributions shown in figures 7.2 and 7.3 the proportion of events at lower angles (cos$\theta \approx 1$) is greater for the backgrounds, particularly, external ^{208}Tl. Cutting out events at low angles should disproportionately target these backgrounds whilst maintaining a high $0\nu\beta\beta$ detection efficiency. The angular distributions for internal backgrounds is less skewed to lower angles (figure 7.3), relative to the radon and external contaminations, therefore they are not expected to have as many events removed at low angles.

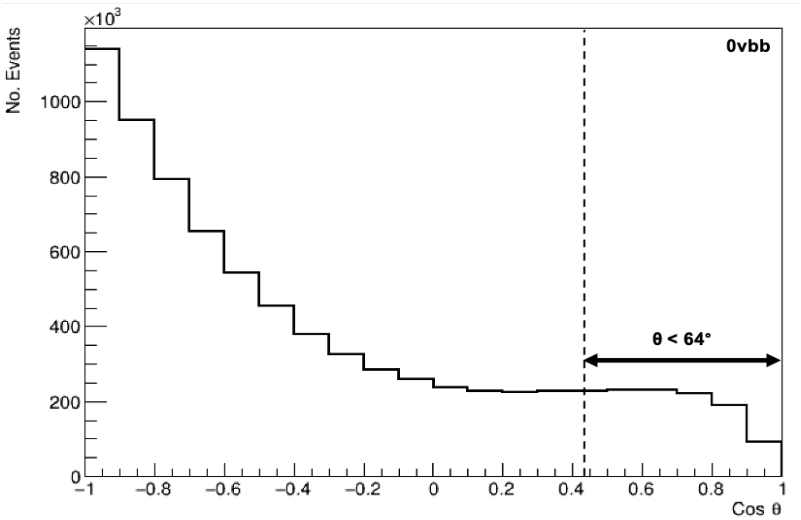

Figure 7.2: $0\nu\beta\beta$ angular distribution for events with a 2e topology and energy in the ^{82}Se ROI. The angular distribution is normalised to the number of simulated events and is only shown for the no field scenario. The calculated maximum angle for two charged particles striking adjacent calorimeters is shown by the dashed line.

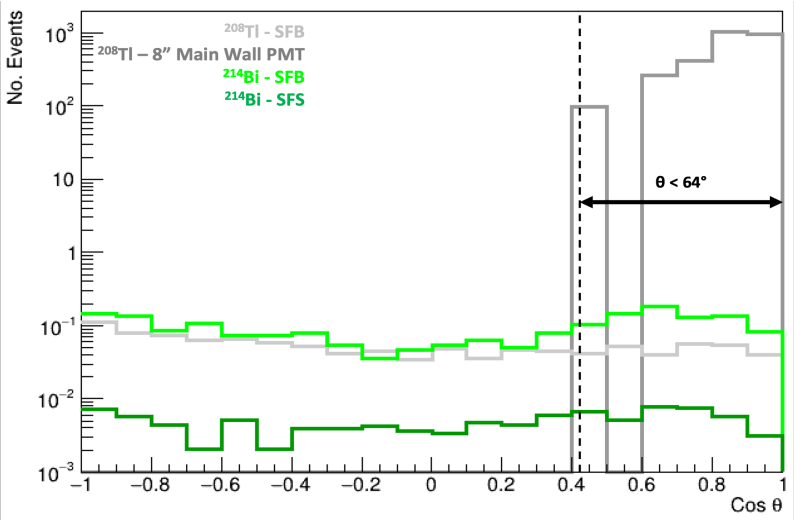

Figure 7.3: ^{208}Tl in the source foil bulk (SFB), ^{208}Tl on the 8" Main wall PMTs, ^{214}Bi in the source foil bulk (SFB) and ^{214}Bi on the surface of the source foil (SFS) angular distributions for events with a 2e topology and energy in the ^{82}Se ROI. The angular distribution is normalised to the exposure and is only shown for the no field scenario. The calculated maximum angle for two charged particles striking adjacent calorimeters is shown by the dashed line.

7.1.2 Minimum Angle Optimisation

Prior to applying the minimum angle cut, the optimum angle was first determined by investigating a number of different minimum angles, ranging from 0° (no minimum angle), to 100°, increasing in increments of 10°. The signal detection efficiency and background contributions were measured for each of the minimum opening angles and used to plot figure 7.4 below.

For all three magnetic fields, the $s/\sqrt{b}$ ratio increases with the minimum opening angle, until approximately 60° to 70°, following which the ratio plateaus. Angles above 100° were not considered as they would begin to remove excessive amounts of signal events (figure 7.2). The increase in $s/\sqrt{b}$ with increasing minimum opening angle was most abrupt for no field as the low angle external ^{208}Tl events are removed, unlike the uniform and realistic fields which have much lower contributions from external ^{208}Tl. At higher angles (>50°), the cut removes a greater number of internal backgrounds but also begins to remove a significant number of signal events resulting in the ratio plateauing.

For no field and the realistic field, as the minimum angle increases, the internal backgrounds begin to dominate as the external contribution is removed. At around 70°, the number of external backgrounds for all three magnetic fields is reduced to zero, corresponding to the peak $s/\sqrt{b}$. From this we can assert that the optimum minimum opening angle cut should be between 65° and 75° which is the consensus for all three magnetic fields. At higher angles, the reduction in signal limits any improvement in $s/\sqrt{b}$ and at angles below 65°, the external backgrounds, particularly for no

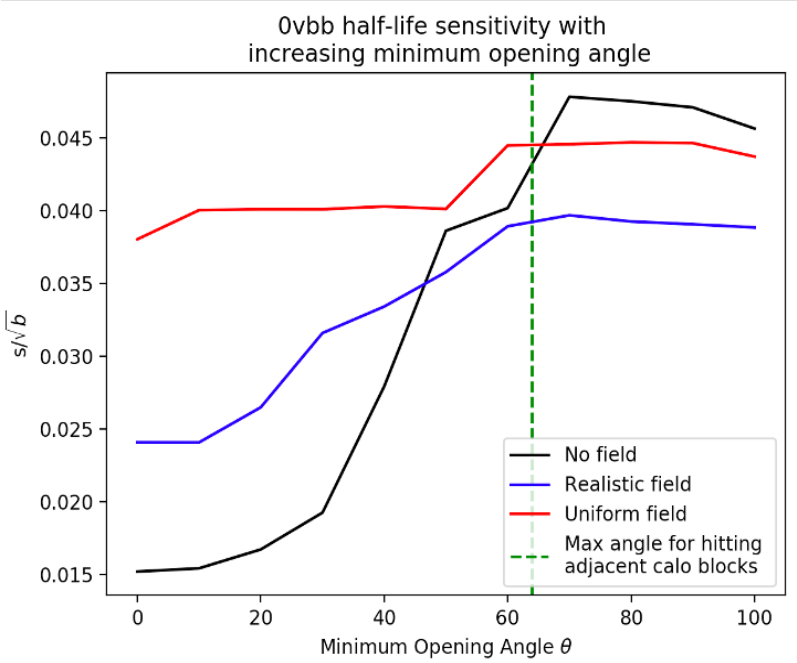

Figure 7.4: Signal over the square root of the background dependence on the minimum opening angle between two electrons for the three magnetic field configurations. The data includes events with a 2e topology and energy in the 2.8 - 3.2 MeV range. The calculated maximum angle for two charged particles striking adjacent calorimeters is shown by the dashed line (section 7.1.3).

field and the realistic field, significantly degrade the detector performance.

7.1.3 No Adjacent Calorimeter Hits

Double beta candidate events generated by external ^{208}Tl are primarily low angle events, often resulting in events with hits in adjacent calorimeters. Adjacent calorimeter events are described as events with a second calorimeter hit, occurring in any of the horizontally, vertically or diagonally neighbouring calorimeters, to the first hit. A visual description of adjacent calorimeter hits is show in figure 7.5 below. The dashed line in figures 7.2-7.3, around 64°, represents the maximum calculated angle for events with adjacent calorimeter hits, which is calculated using the angle between two maximally separated and diagonally adjacent calorimeter hits.

The adjacent calorimeter cut had to be uniquely implemented into Sensitivity Module using multiple Falaise functions that extracted data from the various data banks. To determine whether an event consists of two adjacent calorimeter hits, the unique geometry identifier (GID) (found in the Falaise data banks 4.1) for the first calorimeter is extracted by the GetGID function. The unique GID is then inputted into the GetNeighbourGIDs function, which provided the GIDs for

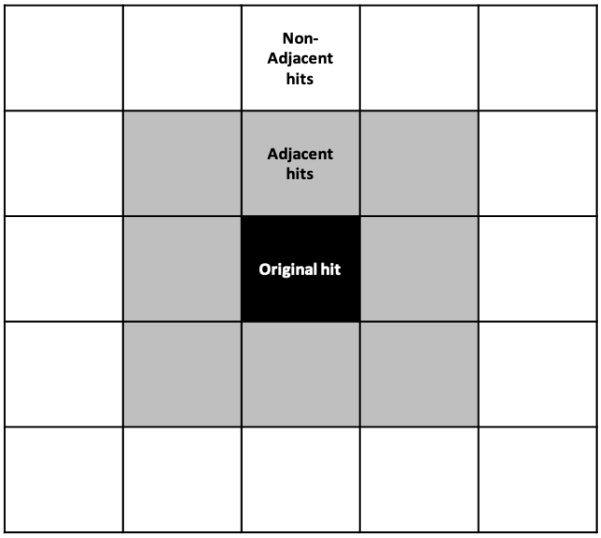

Figure 7.5: Illustration of the adjacent calorimeter hit definition. Any hit within a block horizontally, vertically or diagonally adjacent to the original hit is labelled an adjacent calorimeter hit.

all neighbouring calorimeters. If the second calorimeter hit GID matches one of the neighbouring GIDs, the event is designated as having an adjacent calorimeter hit.

Removing events with hits in adjacent calorimeters provides an alternate approach to the minimum opening angle cut, in the hopes of removing the external backgrounds without significantly reducing the signal detection efficiency. Evidently, there will be a large overlap between the low angle and adjacent calorimeter events, although, the orientation of the reconstructed electrons emitted from the foil can result in low angle events hitting non-adjacent calorimeters. By explicitly targeting the adjacent calorimeter hits commonplace with external ^{208}Tl 2e events, the number of backgrounds may be reduced without reducing the signal efficiency as much as the angle cut. The results for the no adjacent calorimeter hit cut are shown in Table 7.1.

7.1.4 ^{208}Tl Energy Split

^{208}Tl beta decay occurs through the excited state of ^{208}Pb with the emission of a 2.615 MeV photon (figure 6.1) as well as potentially multiple lower energy photons. From 6.1, the main gamma lines can be found at 511, 583, 861 and 2615 keV. The two selected exclusionary regions of 0.2-0.9 and 2.3-2.59 MeV, take into account the prominent ^{208}Tl gamma lines including the Compton continuum.

From [129], multiple exclusionary energy regions were selected for targeting ^{208}Tl backgrounds. Upper and lower regions were identified, for the higher and lower electron energies respectively. For the purpose of this optimisation process, the exclusion region for the lower energy electron

was set as 0.2-0.9 MeV and for the higher energy electron, the exclusion region included electrons with energy between 2.3-2.59 MeV. Events with both the higher and lower energy electrons outside of these regions, pass the cut and contribute towards the total background count. From previous investigations for NEMO-2 and NEMO-3, this selective cut was used during the analysis of ^{100}Mo neutrinoless double beta decay and because the decay energy for ^{82}Se is similar to ^{100}Mo (Table 2.1), the exclusionary energy regions are applicable for the SuperNEMO analysis of ^{82}Se. Like the minimum angle and no adjacent calorimeter cuts, the results for the ^{208}Tl energy separation cut are shown in Table 7.1.

7.2 Optimisation Results

Similar to the minimum angle cut, the adjacent calorimeter hit cut was retrospectively applied to both signal and background to determine the influence of the cut on the sensitivity to neutrinoless double beta decay, for the three magnetic field configurations. Unlike the minimum angle cut, cut optimisation was not required.

	$0\nu\beta\beta$ Detection Efficiency		
	Uniform Field	No Field	Realistic Field
Prior to optimisation	0.0653	0.0790	0.0537
Angle >70°	0.0551	0.0666	0.0451
No adjacent hits	0.0619	0.0754	0.0510
^{208}Tl energy separation	0.0394	0.0470	0.0323

	Total Background Expected Events $s/\sqrt{b}$		
	Uniform Field	No Field	Realistic Field
Prior to optimisation	3.07 ± 0.43 (0.037)	26.69 ± 2.24 (0.015)	4.97 ± 0.92 (0.024)
Minimum Angle 70°	1.59 ± 0.09 (0.044)	1.99 ± 0.10 (0.047)	1.28 ± 0.05 (0.040)
No adjacent hits	1.97 ± 0.11 (0.044)	3.53 ± 0.51 (0.040)	1.77 ± 0.08 (0.038)
Tl energy separation	1.62 ± 0.31 (0.031)	12.86 ± 1.56 (0.013)	2.30 ± 0.59 (0.021)

Table 7.1: $0\nu\beta\beta$ detection efficiency as well as the total background expected events shown alongside the signal over the square root of the background in parenthesis. The values are shown before and after the different optimisation cuts. The three optimisation cuts include the minimum angle of 70°, no adjacent calorimeter hits and the ^{208}Tl energy separation describes in Section 7.1.

Table 7.1 provides the detection efficiency of $0\nu\beta\beta$, the total background expected events and the signal over the square root of the background (in parenthesis), before and after the different optimisation cuts. The highest detection efficiency, for all three magnetic field configurations, is with no additional cut and the lowest detection efficiency is observed with the ^{208}Tl separation. Additionally, the ^{208}Tl separation cut is the least effective in reducing the total background con-

tamination in particular, the ^{208}Tl on the 8" Main wall PMTs. Both the minimum angle and adjacent calorimeter cuts successfully remove the external ^{208}Tl events, significantly reducing the total background count.

Although the detection efficiency of $0\nu\beta\beta$ was reduced by the angle cut further than the adjacent calorimeter cut, the angle cut more successfully reduced the number of internal backgrounds. As show in figure 7.3, there are a significant number of internal backgrounds at smaller angles and so the minimum angle cut is able to remove a greater number of backgrounds, whether internal, radon or external. From Table 7.1, the minimum angle cut brought about the lowest number of expected backgrounds, most notably, for the no field scenario as the prominent cut removed the external ^{208}Tl 8" Main wall PMTs contamination. The no adjacent hit cut removes the majority of external ^{208}Tl but only a small number of internal backgrounds resulting in a higher background count. Applying the ^{208}Tl energy separation optimisation reduces the detection efficiency of $0\nu\beta\beta$ to roughly 60% of the non optimized value. Critically, the energy separation cut fails to remove the majority of the external ^{208}Tl backgrounds.

7.2.1 Window Region Optimisation

Optimisation with a minimum angle requirement was shown to most effectively reduce the total $0\nu\beta\beta$ background count and resulted in the highest $s/\sqrt{b}$ ratio for the three optimisation cuts discussed in Section 7.1. Consequentially, the window optimisation presented in this section was performed after applying the minimum angle cut. Moreover, the window region optimisation uses MDA (Section 4.5.1) as the figure of merit for optimisation, unlike the previous optimisation cut which used the total background events and the signal to $\sqrt{\text{background}}$ ratio as shown in Table 7.1.

Throughout this work, the region of interest for ^{82}Se neutrinoless was stated as 2.8-3.2 MeV as a consequence of the 3 MeV ^{82}Se decay energy. However it is possible to fine tune this window region to maximise the expected sensitivity. To optimize the ROI window, the lower end of the ROI was shifted from 2.8 MeV to 2.6 MeV in increments of 0.05 MeV and at the same time the upper limit was shifted from 3.2 MeV to 3 MeV. With each changing ROI, the sensitivity was calculated after applying all cuts as well as the additional minimum angle optimisation cut, which produced the highest sensitivity as shown in section 7.2. Additionally the window optimisation was only performed for the no field scenario, after optimisation with the minimum angle cut.

The number of expected background events with each of the selected ROIs is shown in 7.2 with the signal efficiency, total expected backgrounds and overall sensitivity shown in table 7.3. From table 7.3, the energy region shown to have the highest sensitivity is the 2.75-3.15 MeV region. This is mostly a result of the much greater detection efficiency for $0\nu\beta\beta$ at this lower energy region whilst still suppressing the background contamination (table 7.2), in particular, from the problematic external ^{208}Tl. The peak of the $0\nu\beta\beta$ spectrum is between 2.7-3 MeV, however after 3 MeV number

	No. Of Expected Events				
ROI MeV	Internal ^{208}Tl	Internal ^{214}Bi	External ^{208}Tl	$2\nu\beta\beta$	Other BGs
2.80 - 3.20	0.77 ± 0.02	1.04 ± 0.06	0	0.10 ± 0.01	0.08 ± 0.01
2.75 - 3.15	0.79 ± 0.02	1.76 ± 0.08	0.21 ± 0.21	0.40 ± 0.14	0.12 ± 0.01
2.70 - 3.10	0.79 ± 0.02	2.89 ± 0.11	0.43 ± 0.30	1.90 ± 0.34	0.19 ± 0.01
2.65 - 3.05	0.78 ± 0.02	4.50 ± 0.13	0.43 ± 0.30	5.70 ± 0.60	0.28 ± 0.02
2.60 - 3.00	0.78 ± 0.02	6.60 ± 0.16	0.21 ± 0.21	16.24 ± 1.01	0.39 ± 0.02

Table 7.2: Number of expected events for the most significant backgrounds for different ROIs. The backgrounds include, internal ^{208}Tl, internal ^{214}Bi, external ^{208}Tl and $2\nu\beta\beta$. as a with changing ROI

of successfully reconstructed events rapidly drops off and so shifting the ROI closer to 2.7 MeV increases the signal efficiency with only a small increase in the background count.

Region of interest MeV	Signal Efficiency	Expected Backgrounds	Sensitivity MDA $\times 10^{24}$ yr.
2.80 - 3.20	0.067	1.99 ± 0.10	1.12
2.75 - 3.15	0.099	3.28 ± 0.27	1.30
2.70 - 3.10	0.126	6.20 ± 0.44	1.26
2.65 - 3.05	0.146	11.69 ± 0.61	1.15
2.60 - 3.00	0.161	24.22 ± 0.89	0.93

Table 7.3: Signal detection efficiency, number of expected events and sensitivity to $0\nu\beta\beta$ for different regions of interest in the range from 2.6 to 3.2 MeV. Values provided are for the no field scenario after the additional minimum angle optimisation, with a total exposure of 15.275 kg yrs.

From the window or region of interest optimisation, the energy window giving the greatest sensitivity to ^{82}Se neutrinoless double beta decay is the region between 2.75 and 3.15 MeV. Below 2.75 MeV, the increased $2\nu\beta\beta$ and ^{214}Bi background contamination begins to rapidly increase. As mentioned in chapter 3, one of the benefits of using ^{82}Se as a double beta decay isotope, is that the relatively high decay energy removes a lot of the lower energy backgrounds that may plight lower

energy double beta decay searches.

Simultaneously, the width of the window was also subject to change and the sensitivity measured. Using tables 7.3 and 7.2, the minimum energy was set to 2.7 MeV and the ROI ranged from 150 to 500 keV. 2.7 MeV was set as the lower limit to avoid the surging $2\nu\beta\beta$ and ^{214}Bi and the minimum width was selected as 150 keV as a consequence of the detectors energy resolution. The full width half maximum (FWHM) is 4% at 3 MeV, which gives a resolution of 120 keV, which defines the minimum ROI width. The results of the different ROI widths are shown in table 7.4.

Region of interest MeV	Signal Efficiency	Expected Backgrounds	Sensitivity MDA $\times 10^{24}$ yr.
2.75 - 3.20	0.099	3.38 ± 0.27	1.30
2.75 - 3.15	0.099	3.28 ± 0.27	1.24
2.75 - 3.10	0.099	3.18 ± 0.27	1.32
2.75 - 3.05	0.099	3.093 ± 0.27	1.35
2.75 - 3.00	0.099	2.97 ± 0.27	1.34
2.75 - 2.95	0.096	2.784 ± 0.27	1.44
2.75 - 2.90	0.087	2.539 ± 0.27	1.33

Table 7.4: Signal detection efficiency, number of expected events and sensitivity to $0\nu\beta\beta$ for different regions of interest in the range from 2.6 to 3.2 MeV. Values provided are for the no field scenario after the additional minimum angle optimisation, with a total exposure of 15.275 kg yrs.

Above 3.05 MeV the increase in signal detection is minimal, whereas there is a small increase in the background count from internal ^{208}Tl. Regardless, the sensitivity remains relatively stable above 2.70 to 3.00 MeV. Below the 3.00 MeV upper limit, the signal efficiency drops faster than the expected backgrounds resulting in a decrease in sensitivity. Using the data shown in tables 7.3-7.4, the optimal lower limit is around 2.70 MeV, below which the background count of $2\nu\beta\beta$ and ^{214}Bi exponentially increase. The upper limit is less prone to variations in sensitivity as the majority of the signal events are found below 3.05 MeV and increasing the upper limit of the ROI merely increases the internal ^{208}Tl contamination.

7.2.2 Final Sensitivities For The Three Magnetic Fields

The final sensitivity values for the three magnetic field scenarios are shown in table 7.5 for a number of different ROIs with a minimum ROI energy of 2.75 MeV. The sensitivities were calculated using the MDA method outlined in section 4.5.1. The signal and background simulations were subject to the two electron cut flow from section 5.2 as well as the additional minimum angle optimisation cut, with the minimum angle set as 70°.

	Sensitivity MDA $\times 10^{24}$ yr.		
Region of interest MeV	Uniform Field	No Field	Realistic Field
2.75 - 3.20	1.23	1.30	1.01
2.75 - 3.15	1.15	1.24	1.00
2.75 - 3.10	1.20	1.32	1.01
2.75 - 3.05	1.31	1.35	1.01
2.75 - 3.00	1.30	1.34	1.00
2.75 - 2.95	1.22	1.44	1.03
2.75 - 2.90	1.11	1.34	0.95

Table 7.5: Sensitivity (MDA) to $0\nu\beta\beta$ for the different region of interests, ranging from 2.75 to 3.2 and 2.75 to 2.9 MeV. The sensitivity estimates are provided for the three magnetic field scenarios following the additional angle optimisation, with a total exposure of 15.275 kg yrs.

From table 7.5, the no field scenario has the highest sensitivity across the range of ROI widths, peaking at an ROI of 2.75 to 2.95 MeV. Reducing the top end of the counting window from 3.2 MeV reduces the total ^{208}Tl internal contamination whilst maintaining the signal detection efficiency, which curtails closer to 3 MeV. As mentioned in section 7.2.1, below 2.7 MeV, the contamination from ^{214}Bi and $2\nu\beta\beta$ exponentially increases as the energy spectra is encroached.

7.2.3 Discussion

Of the three magnetic field configurations investigated, the highest $0\nu\beta\beta$ half-life sensitivity was observed for the no field scenario, with an estimated half-life sensitivity of 1.44×10^{24} years (Table 7.5) for ROI ranging from 2.75 to 2.95 MeV. This sensitivity was achieved using the 2e topology cut flow outlined in Chapter 2 and by applying the additional 70° minimum angle constraint. All sensitivities were calculated using a simple counting version of the MDA method introduced in Section 4.5.1, taking into account the signal and background contributions in the ROI.

The optimum ROI was found to be between 2.75 to 2.95 MeV. Below 2.7 MeV, the background count increases rapidly as the contributions from ^{82}Se $2\nu\beta\beta$ and internal ^{214}Bi become dominant (Figure 6.6). Above 3 MeV there is a minimal gain in the signal detection efficiency, however this is offset by the increase in the total background count from higher energy background sources such as internal ^{208}Tl.

Background contributions from internal, radon and external sources were investigated for the purposes of the magnetic field studies. Internal ^{208}Tl and ^{214}Bi were the two primary contributors to the total background count. Prior to the optimization discussed in Section 7.1, external ^{208}Tl on the 8" Main Wall PMTs was the highest contributing background for the realistic and no field scenarios, however with the addition of the minimum angle cut, the overall background count was reduced and internal ^{208}Tl and ^{214}Bi were established as the main backgrounds. The minimum angle cut removed the majority of low angle external ^{208}Tl events whilst also removing a small proportion of internal and radon backgrounds.

Chapter 8

Conclusion

Neutrinoless double beta decay ($0\nu\beta\beta$) is a hypothesised lepton number violating, Beyond Standard Model (BSM) interaction, whereby an even-even nucleus undergoes two simultaneous beta decays, resulting in the emission of two concurrent β electrons. The most commonly referenced $0\nu\beta\beta$ decay mechanism is the Light Neutrino Exchange (LNE) mechanism (Section 2.3.1), although more complicated SM extensions for neutrinoless double beta decay, have been formulated. Observing neutrinoless double beta decay would have major implications for the fields of particle physics and cosmology, indicating a preference for the leptogenesis mechanism ***ref*** as the origin of the matter-antimatter asymmetry found in the universe. Neutrinoless double beta decay also provides constraints on the absolute neutrino mass (alongside kinematic searches and cosmological measurements), whilst providing the only practical method for establishing the nature of neutrino mass.

SuperNEMO is the latest tracker-calorimeter experiment, following in the footsteps of the previous NEMO experiments and will initially study the $0\nu\beta\beta$ of ^{82}Se. SuperNEMO expects to reach a total sensitivity of $T^{0\nu}_{1/2} > \times 10^{26}$ years, utilising 100 kg of source material. The major benefit of the SuperNEMO tracker-calorimeter technology is the ability to precisely reconstruct the topology of an event, therefore, if a $0\nu\beta\beta$ signal is observed in the $\approx$ 50 meV region, a full SuperNEMO detector will be constructed as it provides the best technology for investigating the underlying decay mechanism for $0\nu\beta\beta$. Although other experiments are projected to reach greater sensitivities over the latest iteration of double beta decay experiments, the precise topological reconstruction of the SuperNEMO demonstrator means SuperNEMO is the ideal candidate for studying any potential $0\nu\beta\beta$ signal.

The SuperNEMO demonstrator module aims to implement a smaller prototype of a full SuperNEMO detector, using 6.1 kg of ^{82}Se with an exposure of 18 kg yrs and expects to achieve a half-life expectancy of $T^{0\nu}_{1/2} > 6.5 \times 10^{24}$ years. Currently, the SuperNEMO demonstrator module has been constructed at the Laboratoire Souterrain de Modane (LSM) and has begun data taking using a small section of the demonstrator module with the whole detector expected to be active come 2022.

SuperNEMO will deploy a magnetic field for the purpose of rejecting backgrounds that originate from sources external to the detector tracking volume. The most prominent background that can be easily differentiated using a magnetic field come from external photons, which interact with the

source foil, producing an electron-positron pair, with opposite curvatures under an applied magnetic field. However, an active magnetic field may be detrimental to the overall detector sensitivity as a result of the reduced $\beta\beta$ signal detection efficiency.

The comparative analysis used in this thesis consisted of event counting in an optimised window Region Of Interest (ROI). Within the ROI, the total background count was determined alongside the signal detection efficiency and the sensitivity for each magnetic field was estimated using the Minimum Detectable Activity (MDA) shown in Section 4.5.1. The ROI counting analysis differs from a more precise, full sensitivity analysis, which takes into account the entire spectral shape and uses additional multivariate parameters to estimate the sensitivity. However, for the purpose of performing a comparative analysis, event counting in the ROI ~~provides a sufficient sensitivity estimation.~~

Firstly, the best case scenario ~~detector~~ was investigated, which estimated the sensitivity of the detector with two neutrino double beta decay ($2\nu\beta\beta$) as the only irreducible background (Section 5.3.1). Of the three magnetic field configurations, the no field scenario achieved the highest best case scenario, ^{82}Se $0\nu\beta\beta$ half-life sensitivity, with an estimated sensitivity of $T^{0\nu}_{1/2} \approx 4.1 \times 10^{24}$ years for a 2.8 to 3.2 ROI ~~and a decay mediated by the LNE mechanism (Section 2.3.1),~~ mostly attributable to the greater signal detection efficiency relative to the uniform and realistic fields.

When considering the total background count in the ROI, the no field scenario once more achieved the highest $0\nu\beta\beta$ half-life sensitivity, using the MDA method, with an estimated sensitivity of $T^{0\nu}_{1/2} \approx 1.4 \times 10^{24}$, ~~for an ROI of 2.75 to 2.95 MeV and a decay mediated by the LNE mechanism.~~ The performance with no field was only marginally greater than the uniform and realistic fields, all three of which achieved a sensitivity of the order 10^{24}, ~~close to the forecasted $T^{0\nu}_{1/2} > 6.5 \times 10^{24}$ sensitivity of the demonstrator module.~~

The magnetic coil has now been installed as part of the demonstrator module so preliminary data taking with no magnetic field can commence in order to fully comprehend the performance of the detector prior to turning on the magnetic coil. Results from this thesis indicate a very similar performance across the different magnetic field configurations, with only a marginal improvement for the no field scenario. Consequently, the most pertinent strategy may be to run the demonstrator module with no field, for an amount of time sufficient to fully characterise the backgrounds and then compare this to the background model produced in this thesis. Comparisons to the background model can help inform the decision about when to turn on the magnetic field or whether to turn it on at all during the demonstrator operational lifetime or for the full SuperNEMO detector.

References

[1] A. Giuliani, J. J. G Cadenas, S. Pascoli, E. Previtali, R. Saakyan, K. Schaffner and S. Schonert, *Double Beta Decay APPEC Committee Report*, **arXiv:1910.04688v2 [hep-ex] 2020**.

[2] C. Cowan, F. Reines, F. Harrison, H. Kruse, and A. McGuire, *Detection of the free neutrino: A Confirmation*, **Science 124 (1956) 103–104**.

[3] R. Davis, *A Review of the Homestake Solar Neutrino Experiment*, **Prog. Part. Nucl. Phys., Vol. 32 (1994) 13-32**.

[4] SNO Collaboration , A. Bellerive et al., *The Sudbury Neutrino Observatory*, **Nuclear Physics B (2016) arXiv:1602.02469v2 [nucl-ex]**.

[5] B. Pontecorvo, *Mesonium and anti-mesonium*, **Sov.Phys.JETP 6 (1957) 429.**.

[6] B. Pontecorvo, *Inverse beta processes and nonconservation of lepton charge*, **Sov.Phys.JETP 7 (1958) 172–173**.

[7] J.Mott, *Search for double beta decay of 82Se with the NEMO-3 detector and development of apparatus for low-level radon measurements for the SuperNEMO experiment*, **PhD Thesis, University College London (2013)**.

[8] Z. Maki, M. Nakagawa, S. Sakata, *Remarks on the Unified Model of Elementary Particles*, **Progress of Theoretical Physics. 28, (1962) 870**.

[9] P.A. Zylaet et al.(Particle Data Group), *Prog. Theor. Exp. Phys.2020*, **083C01 (2020) and 2021 update**

[10] X.Qian, P.Vogel, *Progress in Particle and Nuclear Physics*, **Vol. 83 (2015) 1–30**

[11] P. F. de Salas, et al., *2020 Global reassessment of the neutrino oscillation picture* **arXiv:2006.11237**.

[12] ATLAS Collaboration, *Combined measurements of Higgs boson production and decay using up to 80 fb-1 of proton-proton collision data at $\sqrt{s}$ = 13 TeV collected with the ATLAS experiment*, **Phys. Rev. D 101 (2020) 012002**.

[13] Majorana. E, *Teoria simmetrica dell'elettrone e del positrone*, **Nuovo Cim 14, (1937) 171**.

[14] J. Angrik et al., *KATRIN design report 2004, KATRIN Collaboration*, **Technical report, KATRIN, 2005**.

[15] M.Aker et al., *First direct neutrino-mass measurement with sub-eV sensitivity*, **arXiv:2105.08533v1 [hep-ex] (2021)**

[16] M. Tanabashi et al., *(Particle Data Group)*, **Phys. Rev.D 98, 030001 (2018)**.

[17] J. J. Evans, *The MINOS experiment: results and prospects*, **arXiv:1307.0721v1 [hep-ex] (2013)**.

[18] S.R. Choudhury, S. Hannestad, *Updated results on neutrino mass and mass hierarchy from cosmology with Planck 2018 likelihoods*, **JCAP07(2020)037**.

[19] A. Gando, et al., *Search for Majorana Neutrinos near the Inverted Mass Hierarchy Region with KamLAND-Zen*, **arXiv:1605.02889v2 [hep-ex] (2016)**.

[20] M. Agostini et al. (GERDA Collaboration), *Final Results of GERDA on the Search for Neutrinoless Double-β Decay*, **PHYSICAL REVIEW LETTERS 125 (2020), 252502**.

[21] C. Weizsacker, *Zur Theorie der Kernmassen*, **Z.Phys. 96 (1935) 431–458**.

[22] M. Goeppert-Mayer, *Double Beta-Disintegration*, **Phys. Rev. 48, (1935)**.

[23] L. Simard, *The NEMO-3 results after completion of data taking*, **J. Phys. Conf. Ser., (2012) 375:042011**

[24] M. Mirea et al., *Phase Space Factors for Double Beta Decay: an up-date*, **arXiv:1411.5506 [nucl-th] (2015)**

[25] G. Racah, *On the symmetry of particle and antiparticle*, **Nuovo Cim. 14 (1937) 322–328**.

[26] W. H. Furry, *On Transition Probabilities in Double Beta-Disintegration*, **Phys. Rev. 56 (1939), 1184-1193**.

[27] S. Dell'Oro S. Marcocci, M. Viel, F. Vissan, *Neutrino Masses and Oscillations 2015*, **Advances in High Energy Physics, vol. (2016), Article ID 2162659, 37 pages, 2016**.

[28] J. Schechter, J. Valle, *Neutrino Masses in SU(2) $\times$ U(1) Theories*, **Phys.Rev. D22 (1980) 2227**.

[29] M. Doi, T. Kotani, H. Nishiura, E. Takasugi *DOUBLE BETA DECAY*, **Prog.Theor.Phys. 69 (1983) 602**.

[30] A. K. Chopra, *Construction and commissioning of the tracker for the SuperNEMO Demonstrator Module and unfolding the $2\nu\beta\beta$ spectrum of ^{100}Mo from the NEMO-3 experiment.* **PhD Thesis, University College London (2019)**.

[31] N. Fatemi-Ghomi, *Measurement of the double beta decay half-life of 150Nd and search for neutrinoless decay modes with NEMO-3 detector*, **(2009) arXiv:0905.0822 [hep-ex]**.

[32] SuperNEMO Collaboration, R. Arnold et al., *Probing New Physics Models of Neutrinoless Double Beta Decay with SuperNEMO*, **Eur.Phys.J. C70 (2010) 927–943, arXiv:1005.1241 [hep-ex]**.

[33] S. Dell'Oro, S. Marcocci, M. Viel, F. Vissani, *Neutrinoless double beta decay: 2015 review*, **Advances in High Energy Physics, Volume 2016 (2016), arXiv:1601.07512**.

[34] R. A. Sen'kov, M. Horoi, *Accurate shell-model nuclear matrix elements for neutrinoless double-beta decay*, **Phys. Rev. C 90, 051301(R) (2014) arXiv:1411.1667**.

[35] J. Terasaki, *Many-body correlations of quasiparticle random-phase approximation in nuclear matrix element of neutrinoless double-beta decay*, **Phys. Rev. C 91, 034318 (2015) arXiv:1408.1545**

[36] J. Barea, J. Kotila, F. Iachello, *Nuclear matrix elements for double-β decay*, **Phys. Rev. C 87, 014315 (2013) arXiv:1301.4203**.

[37] P. K. Rath et al., *Neutrinoless $\beta\beta$ decay transition matrix elements within mechanisms involving light Majorana neutrinos, classical Majorons and sterile neutrinos*, **Phys. Rev. C 88, 064322 (2013) arXiv:1308.0460**.

[38] Tomás R. Rodríguez, G. Martinez-Pinedo, *Energy density functional study of nuclear matrix elements for neutrinoless $\beta\beta$ decay*, **Phys.Rev.Lett. 105:252503 (2010) arXiv:1008.5260**.

[39] J.F. Berger, M. Girod, D. Gogny, *MICROSCOPIC ANALYSIS OF COLLECTIVE DYNAMICS IN LOW ENERGY FISSION*, **Nuclear Physics A428(1984)23c-3**.

[40] J. M. Yao et al., *Systematic study of nuclear matrix elements in neutrinoless double-β decay with a beyond-mean-field covariant density functional theory*, **Phys. Rev. C 91, 024316 (2015) arXiv:1410.6326**.

[41] F. T. Avignone, S. R. Elliott, and J. Engel, *Double Beta Decay, Majorana Neutrinos, and Neutrino Mass*, **Rev.Mod.Phys. 80 (2008) 481–516, arXiv:0708.1033 [nucl-ex]**.

[42] R. Arnold et al., *Result of the search for neutrinoless double-β decay in ^{100}Mo with the NEMO-3 experiment*, **Physical Review D 92 (2015) 072011 arXiv:1506.05825**.

[43] M. Hoballah, *The SuperNEMO Demonstrator calorimeter commissioning*, **PoS ICHEP (2020) 199**.

[44] C. Vilela, *Search for double-beta decay of 48Ca in NEMO-3 and commissioning of the tracker for the SuperNEMO experiment*, **PhD Thesis, University College London, (2014)**.

[45] A. Jeremie, *The SuperNEMO demonstrator double beta experiment*, **Nuclear Instruments and Methods in Physics Research Section A: Accelerators, Spectrometers, Detectors and Associated Equipment Volume 958 (2020) 162115**.

[46] A. Jeremie, A. Remoto, *The SuperNEMO $\beta\beta$ source production*, **PoS (ICHEP2016) 1018**.

[47] W. R. Hendee, E. R. Ritenour, *Medical imaging physics*, **3rd ed. St.Louis: Mosby-Year Book, (1992)**.

[48] V. Palusova, E. Chauveau, *Neutron background*, **Internal presentation DocDB:5392-v1, (2021)**.

[49] F. Perrot, *Radiopurity measurement of the cathodic wires*, **Internal presentation DocDB:3395-v2, (2014)**.

[50] F. Perrot, *Radiopurity measurements for 8"PMTs and preliminary budget for the SN demonstrator*, **Internal presentation DocDB:4263-v1, (2017)**.

[51] M. Cascella, *Construction and commissioning of the SuperNEMO detector tracker*, **Nuclear Instruments and Methods in Physics Research A 824 (2016) 507–509508**

[52] R. Arnold, C. Augier, et al., *Technical design and performance of the nemo 3 detector*, **Nuclear Instruments and Methods in Physics Research Section A: Accelerators, Spectrometers, Detectors and Associated Equipment (2005), vol. 536, pp. 79 – 122**.

[53] The SuperNEMO Collaboration, *SuperNEMO Conceptual Design Report*, **Internal paper, http://www.hep.ucl.ac.uk/ saakyan/NEMO_Docs/SuperNEMO_Demonstrator_CDR.pdf**.

[54] S. Calvez, *Development of reconstruction tools and sensitivity of the SuperNEMO demonstrator*, **Thèse de doctorat de l'Université Paris-Saclay (2017)**.

[55] A.S. Barabash et al., *Calorimeter development for the SuperNEMO double beta decay experiment*, **Nuclear Inst. and Methods in Physics Research, A 868 (2017) 98–108**.

[56] R. M. Salazar, *Calibration and Monitoring Systems for Neutrinoless Double Beta Decay Searches in the SuperNEMO Experiment*, **PhD Thesis, The University of Texas at Austin (2021)**.

[57] M. Berglund, M. E. Wieser, *Isotopic compositions of the elements 2009 (IUPAC Technical Report)*, **Pure Appl. Chem., 2011, Vol. 83, No. 2, pp. 397-410**.

[58] E. der Mateosian, M. Goldhaber, *Limits for Lepton-Conserving and Lepton-Nonconserving Double Beta Decay in Ca^{48}*, **Phys. Rev. 146 (1966), 810**

[59] E. Fiorini et al., *A Search for Lepton Nonconservation in Double Beta Decay With a Germanium Detector*, **Phys.Lett.B 25 (1967) 602-603**.

[60] A. Barabash, *Precise Half-Life Values for Two-Neutrino Double-β Decay: 2020 review*, **arXiv:2009.14451v1 (2020) [nucl-ex].**

[61] Y. Gando, *Neutrinoless double beta decay search with liquid scintillator experiments*, **[physics.ins-det] (2019) arXiv:1904.06655v1**.

[62] *Low background techniques in bolometers for double-beta decay search*, **[physics.ins-det] (2017) arXiv:1711.01075**.

[63] *Semiconductor-based experiments for neutrinoless double beta decay search*, **Nuclear Physics B (Proc. Suppl.) 229–232 (2012) 141–145142**.

[64] A. Laing on behalf of the NEXT collaboration, *The NEXT double beta decay experiment*, **Journal of Physics: Conference Series 718 (2016) 062033**.

[65] S. Zatschler, *The COBRA experiment status and prospects on the search of neutrinoless double beta-decay*, **AIP conference proceedings (2015), vol. 1686**.

[66] A. Chavarria, C. Galbiati, X. Li, and J. Rowlands, *A high-resolution CMOS imaging detector for the search of neutrinoless double decay in ^{82}Se*, **Journal of instrumentation (2017), vol. 12, no. 3, pp. P03022–P03022**.

[67] C. E. Aalseth et al., *Search for Neutrinoless Double-β Decay in ^{76}Ge with Majorana Demonstrator*, **Phys. Rev. Lett. (2018), 120:132502**

[68] H.V. Klapdor-Kleingrothaus et al., *Latest results from the HEIDELBERG-MOSCOW double beta decay experiment*, **Eur. Phys. J. (2001), A12:147**

[69] C. E. Aalseth et al., *IGEX ^{76}Ge neutrinoless double-beta decay experiment: Prospects for next generation experiments*, **Phys. Rev. (2002), D65:092007**.

[70] K. H. Ackermann et al., *The GERDA experiment for the search of $0\nu\beta\beta$ decay in ^{76}Ge*, **Eur. Phys. J.)(2013) C73:2330**.

[71] N. Abgrall et al., *The MAJORANA DEMONSTRATOR Neutrinoless Double-Beta Decay Experiment*, **Adv. High Energy Phys. (2014), 2014:365432**.

[72] P. S. Barbeau, J. I. Collar, O. Tench, *Large-Mass Ultra-Low Noise Germanium Detectors: Performance and Applications in Neutrino and Astroparticle Physics*, **(2007) JCAP 0709:009**.

[73] M. Agostini et al., *Results on neutrinoless double-β decay of ^{76}Ge from Phase I of the GERDA experiment*, **Phys. Rev. Lett. (2013), vol. 111, p. 122503**.

[74] M. Agostini et al., *Improved Limit on Neutrinoless Double-β Decay of ^{76}Ge from GERDA Phase II*, **Phys. Rev. Lett. (2018), 120:132503**.

[75] S. I. Alvis et al., *Search for neutrinoless double- decay in ^{76}Ge with 26 kgyr of exposure from the Majorana demonstrator*, **Physical review. C (2019), vol. 100, no. 2**.

[76] J. Myslik for the LEGEND collaboration, *LEGEND: The Large Enriched Germanium Experiment for Neutrinoless Double-Beta Decay*, **(2018) arXiv:1810.00849v1 [physics.ins-det]**.

[77] S. Umehara et al., *Neutrino-less double-beta decay of ^{48}Ca studied by $CaF_2(Eu)$ scintillators*, **Phys.Rev. C78 (2008) 058501, arXiv:0810.4746 [nucl-ex]**.

[78] S. Ajimura et al., *Low background measurement in CANDLES-III for studying the neutrino-less double beta decay of ^{48}Ca*, **(2021) arXiv:2008.09288v3 [hep-ex]**.

[79] Gando A, et al. Phys. Rev. Lett. 110:062502 (2013)

[80] J. Shirai, *Results and future plans for the KamLAND-Zen experiment*, **Journal of physics. Conference series (2017), vol. 888, no. 1, pp. 12031**.

[81] A. Gando et al, *"Search for Majorana neutrinos near the inverted mass hierarchy region with KamLAND-Zen*, **Phys. Rev. Lett. (2016), vol. 117, p. 082503**.

[82] Y. Gando, *First results of KamLAND-Zen 800*, **J. Phys. Conf. Ser.(2020), vol. 1468, no. 1, p. 012142**.

[83] A. Andringa, *SNO+ present status and prospects*, **Journal of physics. Conference series (2019), vol. 1137, no. 1, pp. 12053**.

[84] D. Poda and A. Giuliani, *Low background techniques in bolometers for double-beta decay search*, **International Journal of Modern Physics A (2017), vol. 32, no. 30**.

[85] E. Andreotti, C. Arnaboldi, F. Avignone, M. Balata, I. Bandac, et al., *^{130}Te Neutrinoless Double-Beta Decay with CUORICINO*, **Astropart.Phys. 34 (2011) 822–831, arXiv:1012.3266 [nucl-ex]**.

[86] C. Auldino et al., *First Results from CUORE: A Search for Lepton Number Violation via $0\nu\beta\beta$ Decay of ^{130}Te*, **Phys. Rev. Lett. (2018) 120, 132501**.

[87] C. Alduino et al., *CUORE-0 detector: design, construction and operation*, **Journal of Instrumentation (2016), vol. 11, pp. P07009–P07009**

[88] D. Adams et al. *CUORE: The first bolometric experiment at the ton scale for rare decay searches*, **Nuclear instruments & methods in physics research. Section A, Accelerators, spectrometers, detectors and associated equipment (2019), vol. 936, pp. 158–161**.

[89] D.R. Artusa et al., *Enriched TeO_2 bolometers with active particle discrimination: Towards the CUPID experiment*, **Physics Letters B 767 (2017) 321–329**.

[90] E. S. Battistelli, F. Bellini, C. Bucci, M. Calvo, L. Cardani, N. Casali and M. G. Castellano *Calder: neutrinoless double-beta decay identification in TeO[Formula: see text] bolometers with kinetic inductance detectors*, **The European physical journal. C, Particles and fields (2015), vol. 75, no. 8, pp. 1**.

[91] O. Azzolini et al., *First result on the neutrinoless double-β decay of ^{82}Se with CUPID-0*, **Phys. Rev. Lett. (2018), vol. 120, p. 232502**.

[92] A. S. Barabash et al., *Enriched Zn100MoO4 scintillating bolometers to search for 0v2b decay of 100Mo with the LUMINEU experiment*, **European Physical Journal C: Particles and Fields (2014), vol. 74, no. 11, p. 3133 (7 p.)**

[93] J. L. Ouellet, *New results from the CUORE experiment*, **(2021), arXiv:2011.09295v2 [physics.ins-det]**

[94] J. Y. Lee, et al., *Measurement of the Background Activities of a ^{100}Mo-enriched powder sample for AMoRE crystal material using a single high purity germanium detector*, **IEEE Trans. Nucl. Sci. (2018), 65:2041**.

[95] M. Lee, AMoRE: a search for neutrinoless double-beta decay of ^{100}Mo using low-temperature molybdenum-containing crystal detectors, **Journal of instrumentation, (2020) vol. 15, no. 8, pp. C08010–C08010**.

[96] V. Alvarez et al., *NEXT-100 technical design report (TDR). executive summary*, **Journal of Instrumentation (2012), vol. 7, pp. T06001–T06001**.

[97] J. Aalbers et al., *DARWIN: towards the ultimate dark matter detector*, **(2016) arXiv:1606.07001v1 [astro-ph.IM]**.

[98] M. Auger et al., *The EXO-200 detector, part I: Detector design and construction*, **(2012) arXiv:1202.2192v2 [physics.ins-det]**.

[99] N. Ackerman et al., *Observation of two-neutrino double-beta decay in ^{136}Xe with the EXO-200 detector*, **Phys. Rev. Lett. (2011), vol. 107, p. 212501**.

[100] J. B. Albert et al., *Search for Neutrinoless Double-Beta Decay with the Upgraded EXO-200 Detector*, **Phys. Rev. Lett. (2018), 120, 072701**.

[101] J. B. Albert et al., *Sensitivity and discovery potential of the proposed nEXO experiment to neutrinoless double-β decay*, **Phys. Rev. (2018), C 97, 065503**.

[102] F. Piquemal for the NEMO collaboration, *Results from the NEMO experiment*, **Nuclear Physics B (Proc. Suppl.) 77 (1999) 352-356**.

[103] M. Bongrand, and on behalf of the SuperNEMO Collaboration, *Search for $0\nu2\beta$ of ^{100}Mo by NEMO-3 and status of SuperNEMO*, **AIP Conference Proceedings (2015) 1666, 170002**.

[104] R. Arnold et al., *Measurement of the double-beta decay half-life and search for the neutrinoless double-beta decay of ^{48}Ca with the nemo-3 detector*, **arXiv.org, (2016), vol. 93, no. 11**.

[105] R. Arnold et al., *Final results on Se double beta decay to the ground state of Kr from the nemo-3 experiment*, **Physical Review D, (2017)**.

[106] R. Arnold et al., *Measurement of the two neutrino double beta decay half-life of Zr-96 with the NEMO-3 detector*, **Nuclear Physics, Section A, (2010), vol. 847, no. 3, pp. 168–179**.

[107] R. Arnold et al., *Result of the search for neutrinoless double-β decay in ^{100}Mo with the NEMO-3 experiment*, **Physical Review D, (2018), vol. 92, no. 7**.

[108] R. Arnold et al., *Measurement of the 2 nu beta beta decay half-life and search for the 0 nu beta beta decay of Cd-116 with the NEMO-3 detector*, **Physical Review D, (2018)**.

[109] R. Arnold et al., *Measurement of the $2\nu\beta\beta$ decay half-life of ^{150}Nd and a search for $0\nu\beta\beta$ decay processes with the full exposure from the NEMO-3 detector*, **arXiv.org, (2016), vol. 94, no. 7**.

[110] A. Giuliani et al., *Double Beta Decay APPEC Committee Report*, **(2020) arXiv:1910.04688v2 [hep-ex]**.

[111] M. Macko, *SuperNEMO Experiment: Study of Systematic Uncertainties of Track Reconstruction and Energy Calibration. Evaluation of Sensitivity to $0\nu\beta\beta$ with Emission of Majoron for ^{82}Se*, **PhD Thesis, Universite de Bordeaux (2018)**.

[112] P. P. Povinec, *Background constrains of the SuperNEMO experiment for neutrinoless double beta-decay searches*, **Nuclear Instruments and Methods in Physics Research Section A: Accelerators, Spectrometers, Detectors and Associated Equipment (2017), vol. 845, pp. 398–403**.

[113] X. Fang, *Radon Background Studies for the SuperNEMO Experiment*, **PhD Thesis, University College London (2021)**.

[114] A.S. Barabash et al., *The BiPo-3 detector for the measurement of ultra low natural radioactivities of thin materials*, **JINST 12 (2017) P06002**.

[115] J. Argyriades et al., *Results of the BiPo-1 prototype for radiopurity measurements for the SuperNEMO double beta decay source foils*, **Nucl. Inst. Meth. A 622 (2010) 120**.

[116] C. Macolino, *Energy calibration of the SuperNEMO demonstrator calorimeter*, **Internal note DocDB:4038 (2016)**.

[117] T. Le Noblet, *Status design of the Light Injection System*, **Internal presentation, DocDB:3874, (2015)**.

[118] H. de Préaumont, *SuperNEMO coil*, **Internal presentation DocDB:3072-v1, (2014)**.

[119] M. Bongrand, *Summary of magnetic shields knowledge*, **Internal presentation DocDB:5189-v1, (2020)**.

[120] product-design-brand-line-angle-png-favpng-WVihW8dtrMiZwLvcyfLfXHF86.jpg (820328).url:https://img.favpng.com/12/20/15/product-design-brand-line-angle-png-favpng-WVihW8dtrMiZwLvcyfLfXHF86.jpg (visited on 22/09/2021).

[121] S. W. Snow, *Estimate of the influence of the magnetic shields on the field in the tracker*, **Internal presentation DocDB:3582-v1, (2015)**.

[122] C. Patrick, *Magnetic field map*, **Internal presentation DocDB:5190-v1, (2020)**.

[123] O. Ponkratenko, V. Tretyak, Y. Zdesenko, *The Event generator DECAY4 for simulation of double beta processes and decay of radioactive nuclei*, **Phys.Atom.Nucl. 63 (2000) 1282–1287, arXiv:nucl-ex/0104018 [nucl-ex]**.

[124] S. Agostinelli, et al., *Geant4—a simulation toolkit*,**Nuclear Instruments and Methods in Physics Research A 506 (2003) 250–303**.

[125] G. Knoll, *Radiation Detection and Measurement*, **ISBN-9780470131480 (2000)**.

[126] D. Boursette, *Neutrino physics with SoLid and SuperNEMO experiments.*, **High Energy Physics - Experiment [hep-ex]. Université Paris-Saclay, (2018)**.

[127] A. Jeremie, *82Se foil position in SuperNEMO demonstrator*, **Internal presentation DocDB:4457-v5, (2017)**.

[128] D. L. Hall, *Development of a simulation model for the SuperNEMO tracker module*, PhD thesis, University of Manchester, 2012.text

[129] R. Arnold, et al., *Possible background reductions in double beta decay experiments*, **Nuclear Instruments and Methods in Physics Research A 503 (2003) 649-657**.

[130] R. Arnold, et al. *Final results on ^{82}Se double beta decay to the ground state of ^{82}Kr from the NEMO-3 experiment*, **Eur. Phys. J. C 78 (2018) 821**.